

**33 FEMTOSECOND YB-DOPED OPTICAL
FREQUENCY COMB FOR FREQUENCY
METROLOGY APPLICATIONS**

A THESIS

SUBMITTED TO THE DEPARTMENT OF PHYSICS

AND THE GRADUATE SCHOOL OF ENGINEERING AND SCIENCE

OF BILKENT UNIVERSITY

IN PARTIAL FULFILLMENT OF THE REQUIREMENTS

FOR THE DEGREE OF

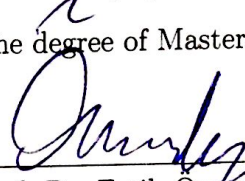
MASTER OF SCIENCE

By

Çağrı Şenel

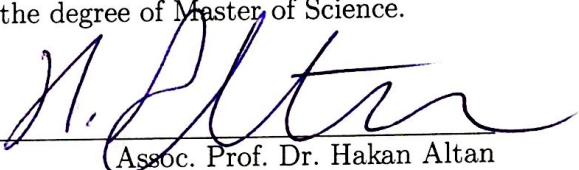
June, 2013

I certify that I have read this thesis and that in my opinion it is fully adequate,
in scope and in quality, as a thesis for the degree of Master of Science.



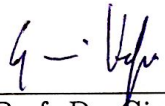
Assist. Prof. Dr. Fatih Omer İlday(Supervisor)

I certify that I have read this thesis and that in my opinion it is fully adequate,
in scope and in quality, as a thesis for the degree of Master of Science.



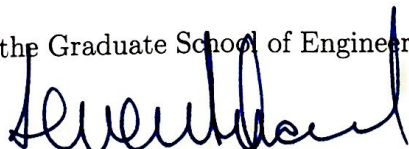
Assoc. Prof. Dr. Hakan Altan

I certify that I have read this thesis and that in my opinion it is fully adequate,
in scope and in quality, as a thesis for the degree of Master of Science.



Assist. Prof. Dr. Giovanni Volpe

Approved for the Graduate School of Engineering and Science



Prof. Dr. Levent Onural
Director of Graduate School of Engineering and Science

ABSTRACT

33 FEMTOSECOND YB-DOPED OPTICAL FREQUENCY COMB FOR FREQUENCY METROLOGY APPLICATIONS

Çağrı Şenel

M.S. in Physics

Supervisor: Assist. Prof. Dr. Fatih Ömer İlday

June, 2013

Optical frequency combs have enabled many applications (high precision spectroscopy, table-top optical frequency metrology, optical atomic clocks, etc.), received considerable attention and a Nobel Prize. In this thesis, the development of a stabilized Yb-doped femtosecond optical frequency comb is presented. As a starting point in the development of the frequency comb, a new type of fiber laser has been designed using numerical simulations and realized experimentally. The developed laser is able to produce pulses that can be compressed to 33 fs without higher-order dispersion compensation. After realization of the laser, a new type of fiber amplifier has been developed to be used for supercontinuum generation. The amplifier produces 6.8 nJ pulses that can be compressed to 36 fs without higher-order dispersion compensation. The dynamics of supercontinuum generation have been studied by developing a separate simulation program which solves the generalized nonlinear Schrödinger equation. Using the simulation results, appropriate photonic crystal fiber was chosen and octave-spanning supercontinuum was generated. Carrier-envelope-offset frequency of the laser has been obtained by building an f - $2f$ interferometer. Repetition rate and carrier-envelope offset frequency of the laser have been locked to Cs atomic clock using electronic feedback circuits, resulting in a fully stabilized optical frequency comb. The noise performance and stability of the system have been characterized. Absolute frequency measurement of an Nd:YAG laser, which was stabilized using iodine gas, has been performed using the developed optical frequency comb.

Keywords: Fiber lasers, fiber amplifiers, optical frequency combs, frequency metrology, numerical simulations.

ÖZET

FREKANS METROLOJİSİ UYGULAMALARI İÇİN 33 FEMTOSANIYE YB-KATKILI OPTİK FREKANS TARAĞI

Çağrı Şenel

Fizik, Yüksek Lisans

Tez Yöneticisi: Yrd. Doç. Dr. Fatih Ömer İlday

Haziran, 2013

Optik frekans tarakları birçok uygulamayı mümkün hale getirmiş (yüksek hassasiyetli spektroskopi, masa üstü optik frekans metrolojisi, optik atomik saatler, vs.), hatırı sayılır derecede ilgi çekmiş ve bir Nobel Ödülü kazanmıştır. Bu tezde, stabilize edilmiş bir Yb-katkılı femtosaniye optik frekans tarağının geliştirilmesi sunulmuştur. Frekans tarağının geliştirilmesi için başlangıç olarak yeni bir tür fiber lazer, nümerik simülasyonlar kullanılarak dizayn edilmiş ve deneysel olarak yapımı gerçekleştirilmiştir. Geliştirilmiş olan lazer, yüksek-dereceli dağılım dengelenmeden 33 fs uzunluğa sıkıştırılabilen atımlar üretebilmektedir. Lazerin yapımının gerçekleştirilmesinden sonra, supercontinuum üretimi için kullanılmak üzere yeni bir tür fiber yükseltici geliştirilmiştir. Fiber yükseltici, yüksek-dereceli dağılım dengelenmeden 36 fs uzunluğa sıkıştırılabilen, 6.8 nJ enerjiye sahip atımlar üretebilmektedir. Supercontinuum üretim dinamikleri, genelleştirilmiş Schrödinger denklemini çözen, geliştirilen başka bir simülasyon programını kullanarak incelenmiştir. Simülasyon sonuçları kullanılarak uygun fotonik kristal fiberi seçilmiş ve oktav-kaplayan supercontinuum üretilmiştir. Lazerin taşıyıcı-zarf ofset frekansı bir $f-2f$ interferometresi yapılarak elde edilmiştir. Lazerin tekrar frekansı ve taşıyıcı-zarf ofset frekansı, elektronik geri-besleme devreleri kullanılarak bir Cs atomik saatine kilitlenmiş, sonucunda tamamen stabilize edilmiş optik frekans tarağı elde edilmiştir. Sistemin gürültü performansı ve kararlılığı karakterize edilmiştir. İyot gazı kullanılarak stabilize edilmiş bir Nd:YAG lazerinin mutlak frekans ölçümü, geliştirilen sistem kullanılarak yapılmıştır.

Anahtar sözcükler: Fiber lazerler, fiber yükselticiler, optik frekans tarakları, frekans metrolojisi, sayısal simülasyonlar.

Acknowledgement

I would like to thank F. Ömer İlday for the high-quality scientific environment that he created and for his priceless mentorship.

I would like to thank all members of UFOLAB for their friendship and support.

I would also like to thank Ramiz Hamid, Cihangir Erdoğan, Mehmet Çelik and Oğuzhan Kara for their continuing support through my studies.

Contents

- 1 Introduction 1**
- 1.1 Introduction to Optical Fiber Technology 1
 - 1.1.1 Brief History of Optical Fibers 1
 - 1.1.2 Structure and Guiding Mechanisms of Modern Optical Fibers 2
- 1.2 Pulse Propagation in Optical Fibers 6
 - 1.2.1 Dispersion 6
 - 1.2.2 Nonlinear Effects 7
 - 1.2.3 Nonlinear Schrödinger Equation 10
- 1.3 Mode-Locked Fiber Lasers 11
 - 1.3.1 A Brief History of Mode-Locked Fiber Lasers 11
 - 1.3.2 Applications of Mode-Locked Fiber Lasers 13
 - 1.3.3 Main Types and Fundamental Dynamics of Mode-Locked Fiber Lasers 13
- 1.4 Femtosecond Frequency Combs 16

2	Numerical Simulations	20
2.1	Finite-Difference Methods	20
2.2	Pseudo-Spectral Methods	21
2.2.1	Split-Step Fourier Method	21
2.2.2	Fourth-Order Runge-Kutta in the Interaction Picture Method	23
2.2.3	Performance Comparison of the Pseudo-Spectral Computational Schemes	25
2.3	Ultrashort Pulse Propagator	28
2.4	Simulation of Supercontinuum Generation Using RK4IP Algorithm	30
2.5	Improvement of the GNLSE	35
3	Supercontinuum Generation in Photonic Crystal Fibers with Femtosecond Pulses	37
3.1	Supercontinuum Generation Dynamics	38
3.1.1	Soliton Fission	38
3.1.2	Raman Scattering	40
3.1.3	Dispersive Wave Generation	41
3.2	Dependence of Generated Supercontinuum on Input Pulse Parameters	42
3.2.1	Dependence on Pulse Wavelength	43
3.2.2	Dependence on Pulse Duration	44
3.2.3	Noise Properties of the Generated Supercontinuum	45

- 4 Net-Zero Dispersion Short Pulsed Laser 48**
 - 4.1 Basic Principles of Similariton Lasers 49
 - 4.2 Basic Principles of Dispersion-Managed Lasers with Net-Zero Cavity Dispersion 51
 - 4.3 Design and Characterization of a Novel Laser 53

- 5 Frequency Comb Stabilization and Absolute Frequency Measurements with The Stabilized Frequency Comb 60**
 - 5.1 Repetition-Rate Stabilization of the Laser 60
 - 5.2 Carrier-Envelope-Offset Frequency Stabilization 62
 - 5.3 Absolute Frequency Measurements with the Stabilized Frequency Comb 67

- 6 Conclusions 74**

- Appendix 88**
 - A Simulation of Pulse Propagation in Fiber Using RK4IP Algorithm 88**

 - B Simulation of Pulse Propagation in Fiber Using RK4IP Algorithm with Adaptive Step-Size 95**

List of Figures

1.1	Basic structure of an optical fiber.	2
1.2	Types of optical fibers [1].	3
1.3	Images of a micro-structured fiber obtained by a scanning electron microscope. (Courtesy of Zuxing Zhang)	5
1.4	Pulse evolution for different types of lasers. Vertical axis is the spectral bandwidth of pulses and horizontal axis is the ratio of pulse durations to the transform-limited pulse durations. Negative values indicate negative frequency-chirp.	14
1.5	The electric field of pulses (left column) and the corresponding spectra (right column).	17
2.1	Schematic illustration of the symmetrized split-step Fourier method used for numerical simulations [2].	23
2.2	Graph of average relative errors for different schemes versus number of computational steps for simulation of a second-order soliton [3].	26
2.3	Graph of average relative errors for different schemes versus number of computational steps for simulation of broadband supercontinuum generation in PCF [3].	27

2.4	Graph of average relative errors for different schemes versus normalized computation time for simulation of broadband supercontinuum generation in PCF [3].	27
2.5	Main screen of Ultrashort Pulse Propagator 3.0.0.	29
2.6	Transmission versus incident power graphs for SSA and NPE for the given parameters.	30
2.7	Experimental and computed Raman response function and Raman gain [4].	31
2.8	Experimental (upper fig.) and simulated (lower fig.) supercontinuum spectra obtained from 30 cm-long SC-3.7-975 photonic crystal fiber.	33
2.9	Comparison of necessary computational time for supercontinuum generation process in PCF for different implementations of symmetrized split-step Fourier method and RK4IP method [5].	35
3.1	Dispersion profile of SC-3.7-975.	39
3.2	Evolution of a third-order soliton in PCF.	39
3.3	Evolution of a third-order soliton in fiber in the absence of higher-order dispersion and Raman scattering.	40
3.4	Raman scattering induced break up of a third-order soliton in PCF in the absence of higher-order dispersion.	41
3.5	Higher-order dispersion induced break up of a third-order soliton in PCF in the absence of Raman scattering.	42
3.6	Temporal and spectral evolution of pulses with different central wavelengths in PCF with ZDW of 984 nm.	43

3.7	Temporal and spectral evolution of pulses with different initial durations in PCF.	45
3.8	Dependence of average SC coherence and -20 dB spectral bandwidth on pump wavelength and pulse duration for constant peak power [6]. Dashed line indicates ZDW.	47
4.1	Schematics of a dispersion-managed laser.	49
4.2	Simulated evolution of pulses in a similariton laser for the first type of evolution.	50
4.3	Simulated evolution of pulses in a similariton laser for the second type of evolution.	51
4.4	Simulated evolution of pulses in a dispersion-managed laser with net-zero cavity dispersion for 0.56 nJ pulse energy.	52
4.5	Simulated evolution of pulses in a dispersion-managed laser with net-zero cavity dispersion for 1 nJ pulse energy.	52
4.6	Schematics of the new laser.	54
4.7	Simulated evolution of pulses in the new laser.	54
4.8	Simulated beamsplitter output of the laser for 3.82 nJ pulse energy.	55
4.9	Simulated compressed beamsplitter output.	55
4.10	50/50 Beamsplitter output of the laser.	56
4.11	Polarizing beamsplitter output of the laser.	57
4.12	Retrieved pulse shape from PICASO algorithm. (Inset) Measured (red) and PICASO retrieved (blue) autocorrelation traces.	57
4.13	Relative intensity noise of the laser.	58

4.14	Phase noise of the laser.	59
5.1	Schematics of the repetition-rate locking and characterization setup.	61
5.2	Relative Allan deviation vs. averaging time graph for the given cases.	63
5.3	Schematics of the supercontinuum generation setup and f-2f interferometer.	63
5.4	Output spectrum of the amplifier.	64
5.5	Compressed pulse shape that is retrieved from PICASO algorithm. (Inset) Measured (red) and PICASO retrieved (blue) autocorrelation traces.	65
5.6	Measured supercontinuum spectrum for 62 mW of coupled average power.	65
5.7	Obtained carrier-envelope offset beat signal.	66
5.8	Schematics of the carrier-envelope offset frequency locking setup. .	67
5.9	Allan deviation vs. averaging time graphs for free-running and stabilized f_{ceo}	68
5.10	Schematics of the absolute frequency measurement setup.	68
5.11	Illustration of LUT and comb teeth.	69
5.12	Nd:YAG beat frequency measurement data.	71
5.13	Overlapping Allan deviation graph for beat signal between the stabilized Nd:YAG laser and one frequency comb tooth.	72

List of Tables

2.1	Values of the parameters used in the intermediate-broadening model	32
3.1	Dispersion coefficients of SC-3.7-975 fiber for wavelength of 1040 nm.	38

Chapter 1

Introduction

1.1 Introduction to Optical Fiber Technology

1.1.1 Brief History of Optical Fibers

Daniel Colladon and Jacques Babinet demonstrated guiding of light by total internal reflection in the early 1840s for the first time [7,8]. Image transmission through tubes was demonstrated independently by John Logie Baird and Clarence Hansell in 1920s [9, 10]. Heinrich Lamm used tubes for internal medical examinations in 1930s [11]. First modern optical fiber was made in late 1930s which consisted of a core region surrounded by a transparent cladding region. First bundle of fiber was produced by Harold Hopkins and Narinder Singh Kapany in 1954 [12]. First optical fiber with glass-cladding was produced by Lawrence E. Curtiss in 1956 [13]. Jun-ichi Nishizawa proposed usage of optical fibers for telecommunication in 1963 [14]. First working fiber-optical telecommunication system was shown by Manfred Brner in 1965 [15,16]. High-fiber losses of that time (~ 1000 dB/km) prevented the building of long-distance communication lines. In 1965, Charles K. Kao and George A. Hockham theorized that optical fibers with losses less than 20 dB/km can be produced using silica glass with high purity [17]. Half of the Nobel Prize in Physics 2009 was awarded to Charles K. Kao for this discovery. First

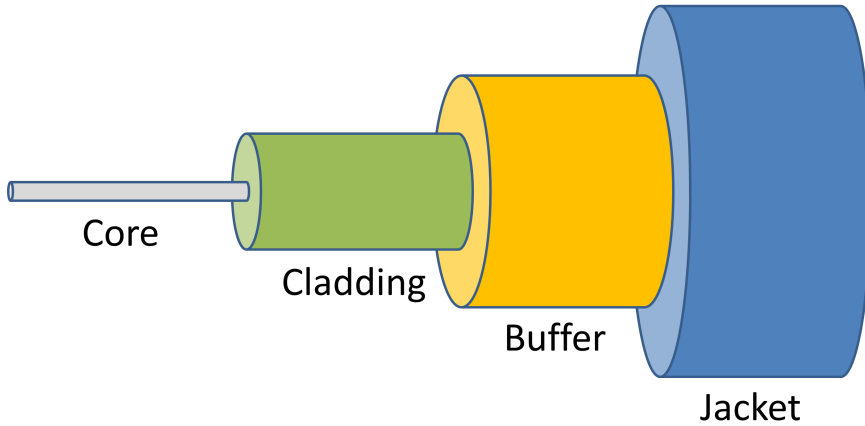


Figure 1.1: Basic structure of an optical fiber.

fiber with loss of 17 dB/km was produced in 1970 by Robert D. Maurer, Donald Keck, Peter C. Schultz and Frank Zimar. They also produced the fiber with loss of 4 dB/km a few years later [18]. First commercial fiber-optical communication system was built in 1975. First optical fiber with loss of 1 dB/km was produced in 1976. Modern optical fibers have losses below 0.2 dB/km. Erbium-doped fiber amplifiers, which reduced the cost of long-distance telecommunication systems by eliminating the need for optical-electrical-optical repeaters, was co-developed by teams led by David N. Payne and Emmanuel Desurvire in 1987 [19,20]. Photonic bandgap fibers were developed in 1991, which guides light by diffraction from a periodic structure [21]. Photonic crystal fibers became commercially available in 2000.

1.1.2 Structure and Guiding Mechanisms of Modern Optical Fibers

Basic structure of modern optical fibers is shown (Fig. 1.1). Light mostly propagates in the core, while some part of the light penetrates into the cladding. Modern optical fibers can be classified into three main categories according to their guiding mechanisms as step-index fibers, graded index fibers and micro-structured fibers.

Step-index fibers have a core with uniform index of refraction and a cladding

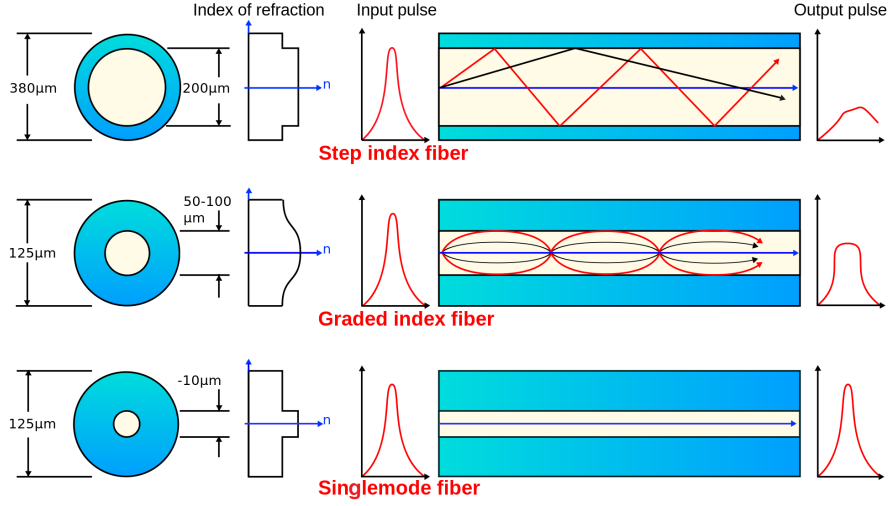


Figure 1.2: Types of optical fibers [1].

with slightly lower, uniform index of refraction. Most single-mode fibers and some multi-mode fibers have step-index profile. Light propagation in multi-mode step-index fibers can be studied using ray optics. For single-mode fibers, since the core size is comparable to the wavelength of the light, wave optics should be used. When the ray optics is used, light guiding can be explained by total internal reflection. The maximum incidence angle for the light to be guided is determined by the numerical aperture (NA) of the fiber, which is given by,

$$\sin \theta_{\max} = NA \equiv \sqrt{n_{\text{core}}^2 - n_{\text{cladding}}^2} \quad (1.1)$$

The number of guided modes is determined by the parameter called V number, which is given by,

$$V = \frac{2\pi}{\lambda} a NA = \frac{2\pi}{\lambda} a \sqrt{n_{\text{core}}^2 - n_{\text{cladding}}^2} \quad (1.2)$$

where, a is the core radius of the fiber. The fibers with V values smaller than ~ 2.405 are single-mode fibers. The number of guided modes can be approximated by the formula given below for large V values:

$$M \approx \frac{4}{\pi^2} V^2 \quad (1.3)$$

V number also determines the fraction of the light that propagates in the core. Mode-field radius for single-mode fibers can be estimated using Marcuse's formula

[22]:

$$\frac{w}{a} \approx 0.65 + \frac{1.619}{V^{3/2}} + \frac{2.879}{V^6} \quad (1.4)$$

where w is the mode-field radius.

Even though the mode profile in the fibers is not rectangular normally, effective mode area of single-mode fibers can be well-approximated by $A = \pi w^2$. However, this formula is not enough for multi-mode fibers and it is necessary to calculate effective mode area using the definition,

$$A_{\text{eff}} = \frac{(\int I dA)^2}{\int I^2 dA} \quad (1.5)$$

where I is the radius-dependent intensity.

Graded-index fibers have a radius-dependent index of refraction such that the index of refraction usually has a parabolic profile and decreases as radial distance from the center of the fiber increases. Mode dispersion is considerably lower in multi-mode graded-index fibers than in multi-mode step index fiber as it is illustrated in Fig. 1.2.

Recently, micro-structured fibers have emerged. Micro-structured fibers consist of a solid or hollow core and some voids in the cladding area. Guiding mechanism of the solid-core micro-structured fibers is similar to the conventional fibers. Voids create a cladding region that has effectively lower index of refraction. Periodicity of the holes is not crucial for this kind of fibers and light can be guided by even a random arrangement of holes. Hollow core micro-structured fibers have a different mechanism of guiding light. A strictly periodic arrangement of the holes with spacing that is close to the wavelength of the light gives rise to a resonant effect that is similar to Bragg diffraction and light is guided by continuous diffraction from the periodic structure. This kind of fibers are named photonic bandgap fibers. Photonic bandgap fibers were also called photonic crystal fibers, which is used as a general name for the micro-structured fibers nowadays. From this point on, micro-structured fibers will be called photonic crystal fibers (PCF).

PCFs opened up the way to many new possibilities. Since almost all of the

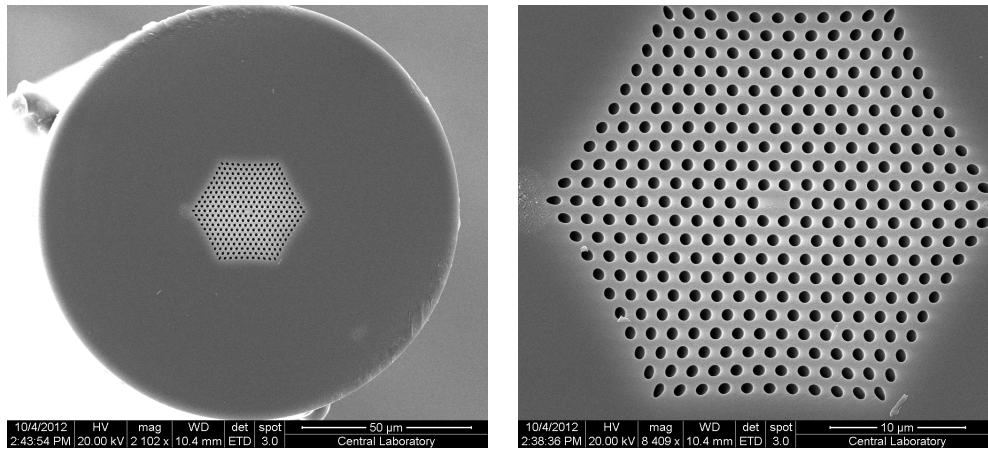


Figure 1.3: Images of a micro-structured fiber obtained by a scanning electron microscope. (Courtesy of Zuxing Zhang)

cladding area can consist of air, it is possible to produce fibers with very small core diameters and very high NA. By adjusting the size of the holes, hole spacing and the core diameter, the dispersion characteristics of PCFs can be engineered. These two properties gave rise to highly nonlinear fibers with arbitrary zero dispersion wavelengths and revolutionized the areas of supercontinuum generation and optical frequency metrology. Hollow core fibers have the potential to be the fibers with the lowest propagation losses since light effectively propagates in air. They allow transfer of light pulses without experiencing Kerr nonlinearity and can be used for pulse compression. Hollow core fibers can be filled with gases and be used as very long gas cuvettes. There is a class of PCF which is called endlessly single-mode fibers. These fibers do not have a higher-order mode cut-off wavelength and can have very large core diameters. PCFs can also be doped with rare earth elements for light amplification. PCFs can be produced to have very high values of birefringence and they can be polarization-maintaining.

1.2 Pulse Propagation in Optical Fibers

1.2.1 Dispersion

Dispersion is the phenomenon in which phase velocity of a wave depends on some factors such as frequency, propagation mode or polarization. Most important of these is the chromatic dispersion, which is caused by the frequency dependence of refractive index. Because of Kramers-Kronig relations, real part of the refractive index depends on the imaginary part of the refractive index, which means the frequency dependence of the phase velocity is related to the frequency dependence of the material absorption. The frequency dependence of refractive index of materials are well-approximated for the frequencies that are far from the medium resonances by the Sellmeier equation,

$$n^2(\omega) = 1 + \sum_{j=1}^m \frac{\beta_j \omega_j^2}{\omega_j^2 - \omega^2} \quad (1.6)$$

where ω_j is the resonance frequency and β_j is the strength of j th resonance. For bulk fused silica, these parameters are given as $\omega_j = 2\pi c/\lambda_j$, $\beta_1 = 0.6961663$, $\beta_2 = 0.4079426$, $\beta_3 = 0.8974794$, $\lambda_1 = 0.0684043 \mu m$, $\lambda_2 = 0.1162414 \mu m$, $\lambda_3 = 9.896161 \mu m$.

Chromatic dispersion plays an important role for pulse propagation in fibers since the spectrum of short pulses are broad. In the presence of the nonlinear effects, dispersion gives rise to very rich dynamics which makes mode-locked femtosecond fiber lasers possible. Effects of fiber dispersion is usually studied by applying a Taylor expansion about a frequency ω_0 :

$$\beta(\omega) = n(\omega) \frac{\omega}{c} = \beta_0 + \beta_1(\omega - \omega_0) + \frac{1}{2}\beta_2(\omega - \omega_0)^2 + \dots \quad (1.7)$$

where

$$\beta_m = \left(\frac{d^m \beta}{d\omega^m} \right)_{\omega=\omega_0} \quad (1.8)$$

β_1 and β_2 are given as

$$\beta_1 = \frac{1}{v_g} = \frac{n_g}{c} = \frac{1}{c} \left(n + \omega \frac{dn}{d\omega} \right) \quad (1.9)$$

$$\beta_2 = \frac{1}{c} \left(2 \frac{n}{\omega} + \omega \frac{d^2 n}{d\omega^2} \right) \quad (1.10)$$

where v_g is the group velocity and n_g is the group index. β_1 is the inverse group velocity and β_2 is the group-velocity dispersion (GVD) coefficient. In optical fiber communications community, it is common to use the dispersion parameter D , which is defined as $D = d\beta_1/d\lambda$. Dispersion parameter D is related to β_2 as

$$D = \frac{d\beta_1}{d\lambda} = -\frac{2\pi c}{\lambda^2} \beta_2 = -\frac{\lambda}{c} \frac{d^2 n}{d\lambda^2} \quad (1.11)$$

Higher orders of dispersion can also be defined. For pulses with small spectral bandwidths higher-order terms can be neglected. In most cases, including the third-order dispersion term suffices. Even higher-order dispersion terms are usually necessary only for extremely broadband pulses as it is the case for supercontinuum generation.

Chromatic dispersion is not the only cause of dispersion in optical fibers. Modal dispersion is an effect that is observed in multi-mode fibers, which causes the light pulses to spread in time since the propagation velocity is not the same for all propagation modes. There is also a special type of modal dispersion called polarization mode dispersion, which is observed even in single mode fibers. Polarization mode dispersion is caused by the birefringence of the fiber which stems from production imperfections and anisotropic stress. Chromatic dispersion is by far the most important type of dispersion for femtosecond fiber lasers and other types of dispersion will be ignored for the rest of the discussions.

1.2.2 Nonlinear Effects

The response of fibers depends on the intensity of light. The most important effects that influence the short pulse propagation are the Kerr effect and Raman scattering. Kerr effect is an instantaneous effect while Raman scattering is a delayed effect.

The Kerr effect is the modification of the phase delay per unit length in proportion to optical power. It can be described as the dependence of the index of refraction on the light intensity:

$$n(I) = n_0 + n_2(I) \quad (1.12)$$

The Kerr coefficient of fused silica is measured as $n_2 \approx 2.7 \times 10^{-20} \text{ m}^2/\text{W}$ for the wavelengths around $1 \text{ }\mu\text{m}$ [23]. The frequency-dependent nonlinearity coefficient of the fibers are usually given in terms of the parameter $\gamma(\omega)$:

$$\gamma(\omega) = \frac{n_2(\omega)\omega}{cA_{eff}(\omega)} \quad (1.13)$$

where A_{eff} is the effective mode-area of the fiber.

Some important consequences of Kerr nonlinearity can be categorized as self-phase modulation, cross-phase modulation and self-focusing effects. Self-phase modulation is the dependency of phase delay for light to its own intensity. When there are more than one beams propagating together with different wavelengths, each beam creates an intensity-dependent phase delay on other beams and this is called cross-phase modulation. Mode-profile in fibers is not rectangular and therefore, intensity of the light is not constant in the transverse direction. This causes the refractive index to depend on the radial distance from the center and leads to self-focusing. Self-phase modulation is the most important consequence of the Kerr effect for short pulses that are propagating in fiber and will be discussed in some detail.

Self-phase modulation determines the main characteristics of short pulse propagation in optical fibers together with dispersion and is very important for pulse formation and mode-locking. In the absence of chromatic dispersion, self-phase modulation does not change the pulse envelope. It creates new frequency components and some frequency chirp. In the presence of anomalous dispersion in the medium, self-phase modulation gives rise to solitonic effects. If the pulse enters the anomalous dispersion medium with positive initial chirp, pulse is compressed temporally and broadened spectrally. When the pulses are negatively chirped and propagated in a medium with normal dispersion, they get compressed in both temporal and spectral domains. Initially transform-limited or positively chirped

pulses go through self-similar parabolic pulse propagation and they evolve into a parabolic shape in both temporal and spectral domains.

Raman scattering is the scattering of photons from optical phonons in the medium. Raman scattering can be divided into two subcategories as Stokes and anti-Stokes scattering. Stokes scattering corresponds to the annihilation of the input photon that is followed by creation of a phonon and a photon with lower frequency. Anti-Stokes scattering corresponds to the annihilation of the input photon and a phonon that is followed by creation of a photon with higher frequency. Anti-Stokes scattering occurs very rarely at low temperatures since it requires the existence of a phonon beforehand. Stokes scattering can take place at any temperature since the phonon is created in the process. The ratio of anti-Stokes to Stokes scattering events is given by [24]:

$$\frac{I_{\text{anti-Stokes}}}{I_{\text{Stokes}}} = \exp(-\hbar\Omega/k_{\text{B}}T) \quad (1.14)$$

where Ω is the absolute angular frequency difference between the input and output photons.

Raman scattering can happen spontaneously or it can be stimulated. Stimulated Raman scattering (SRS) is the dominant type that is observed with short pulses in optical fibers. Stokes scattering rate increases when there are some Stokes photons already in the medium and the rate increases proportionally to the number of both original input (pump) and Stokes (signal) photons. For continuous wave pump and Stokes beams, growth of the intensity of Stokes beam is given by [2]:

$$\frac{dI_S}{dz} = g_R I_P I_S \quad (1.15)$$

where I_S is the intensity of Stokes beam, I_P is the intensity of pump beam and g_R is the Raman gain coefficient. Since ultrashort pulses have wide spectral bandwidths, photons within the pulse with different frequencies can act as pump and signal photons. This causes pulse wavelength to continuously shift towards longer wavelengths in the fiber. This effect is called self-frequency shift. Self-frequency shift becomes especially important for soliton propagation since the peak power of the pulses does not decrease drastically during propagation.

1.2.3 Nonlinear Schrödinger Equation

Evolution of the pulse envelope in optical fibers with second-order group velocity dispersion and self-phase modulation can be described by the nonlinear Schrödinger equation (NLSE):

$$\frac{\partial A}{\partial z} = -i\frac{\beta_2}{2}\frac{\partial^2 A}{\partial T^2} + i\gamma|A|^2 A \quad (1.16)$$

where A is the normalized pulse amplitude such that $|A|^2$ gives the optical power, β_2 is the second-order group velocity dispersion coefficient, γ is the nonlinearity coefficient and z is the propagation direction. NLSE can be derived from Maxwell's equations and the derivation can be found in [2]. NLSE is sufficient for modelling pulses with relatively small bandwidths and moderate peak powers.

NLSE can be generalized to include the effects of gain, loss, higher order dispersion, stimulated Raman scattering and self-steepening [2]. Higher-order dispersion can be added to the equation through a simple summation. Higher-order nonlinear effects can be added by adding more terms of the Taylor expansion of the nonlinearity coefficient γ :

$$\gamma(\omega) = \gamma(\omega_0) + \gamma_1(\omega - \omega_0) + \frac{1}{2}\gamma_2(\omega - \omega_0)^2 + \dots \quad (1.17)$$

In practice, it is enough to keep the first two terms of the expansion. Stimulated Raman scattering can be included in the equation via use of a response function [25]. Resulting equation is called the generalized nonlinear Schrödinger equation (GNLSE):

$$\begin{aligned} \frac{\partial A}{\partial z} + \frac{\alpha}{2}A + \left(\sum_{n \geq 2} \beta_n \frac{i^{n-1}}{n!} \frac{\partial^n}{\partial t^n} \right) A = i \left(\gamma(\omega_0) + \gamma_1 \frac{\partial}{\partial t} \right) \\ \times \left((1 - f_R)A|A|^2 + f_R A \int_0^\infty h_R(t')|A(z, t - t')|^2 dt' \right) \end{aligned} \quad (1.18)$$

where α is the loss (or gain) coefficient, γ_1 is a higher-order nonlinearity term, f_R is the fraction of the delayed Raman response and h_R is the Raman response function. GNLSE is sufficient to model very complicated processes like supercontinuum generation.

1.3 Mode-Locked Fiber Lasers

Mode-locked fiber lasers are pulsed lasers that use fibers that are doped with rare-earth elements (such as neodymium, erbium, ytterbium, thulium, praseodymium, thulium and holmium) as the gain media. Mode-locked fiber lasers have replaced their gain-crystal based predecessors in most applications due to their lower cost, better environmental stability and comparable pulse parameters. In this section, a brief history, applications and fundamental dynamics of mode-locked fiber lasers will be presented.

1.3.1 A Brief History of Mode-Locked Fiber Lasers

First mode-locked fiber laser was built in 1986 using neodymium-doped fiber [26]. The laser was operating at $1.08 \mu\text{m}$ and the pulse energy was 17 pJ. The Nd-doped fiber had normal dispersion at that wavelength, but the possibility of building a soliton laser using erbium-doped fibers was discussed in the same article. This was followed by the demonstration of the soliton fiber lasers using Yb:Er co-doped fiber in 1989 [27]. In this study, 70 ps pulses with $1.56 \mu\text{m}$ wavelength and 6 pJ energy were produced. An erbium soliton laser that produces 4 ps pulses at $1.53 \mu\text{m}$ with output pulse energy of 11 pJ was also demonstrated in the same year [28]. First femtosecond erbium fiber laser was demonstrated in 1991 [29]. This laser was passively mode-locked using a nonlinear amplifying loop mirror as a virtual saturable absorber and produced 314 fs pulses. First mode-locked thulium-doped fiber laser was demonstrated in 1992, which was operating at 810 nm [30]. Same year, 30 fs pulses were generated by an amplified all-fiber Er laser [31]. 180 fs pulses with 100 pJ pulse energy were produced using an Er-doped fiber with normal dispersion and in-cavity dispersion compensation with prism pair in 1993 [32]. In the same year, 42 fs pulses at $1.06 \mu\text{m}$ with 1 nJ pulse energy were generated using a neodymium fiber laser [33]. First mode-locked praseodymium-doped fiber laser which was operating at $1.3 \mu\text{m}$ was also demonstrated in 1993 [34]. Stretched-pulse erbium fiber lasers, which consist of normal and anomalous dispersion fibers were presented later [35–37].

They had energies around 1 nJ and were an improvement over the soliton lasers. Femtosecond pulses were obtained from a tunable Th-doped fiber laser in 1995 [38]. The demonstrated laser was tunable from 1.8 μm to 1.9 μm . First mode-locked Yb:glass fiber laser was built in 1998 [39]. Yb fiber lasers became increasingly popular due to their broad gain bandwidth and low quantum defect. In 2003, 36 fs pulses were generated with 1.5 nJ pulse energy by optimizing the cavity dispersion map [40]. First similariton laser was demonstrated in 2004 using Yb-doped fibers for gain and diffraction gratings for dispersion management [41]. The experimentally demonstrated laser had 2 nJ pulse energy but the possibility of reaching much higher energies was shown using numerical simulations. All-normal-dispersion (ANDi) Yb-doped fiber laser was demonstrated in 2006 [42]. It was not the first fiber laser that was built using all-normal-dispersion components, since even the first mode-locked fiber laser was built using all-normal-dispersion components, but rather it was the first passively mode-locked femtosecond all-normal-dispersion laser. ANDi laser included a spectral filter in the cavity to balance the effects of Kerr nonlinearity and chromatic dispersion and produced highly chirped pulses, opening the way to pulses with even higher energies. Using Yb-doped large mode area photonic crystal fibers, ANDi lasers that produce sub-100 fs pulses with microjoule-level pulse energy and tens of watts average power has been presented [43]. In 2007, first mode-locked bismuth-doped fiber laser was built, which was operating at 1.16 μm [44]. In 2010, the possibility of incorporating different pulse evolution mechanisms into one laser was shown for the first time by demonstration of the soliton-similariton laser [45]. First mode-locked holmium-doped fiber laser was demonstrated in 2012, which was operating at 2.09 μm [46]. Even though continuous-wave dysprosium-doped fiber lasers that operate around 2.9 μm have been built, a mode-locked Dy-doped fiber laser has not been demonstrated yet [47, 48].

In the current state of the technology, shortest pulses from fiber lasers are produced by Yb-doped fiber lasers and are ~ 20 fs-long [49]. Even shorter pulses are generated by amplified erbium-based systems. Few-cycle pulse generation have been demonstrated by several groups and pulses as short as one optical cycle are generated [50–53]. Highest pulse energies also produced by Yb-doped fiber

lasers and they are in the order of microjoule [54, 55]. Yb-doped fiber amplifiers produce millijoule pulse energies and gigawatt peak powers [56].

1.3.2 Applications of Mode-Locked Fiber Lasers

Mode-locked fiber laser have very important scientific and technological applications and some applications of the mode-locked fiber lasers can be listed as such: Femtosecond frequency combs (Nobel Prize in Physics 2005) [57], micro-machining [58], nonlinear optics (optical parametric oscillators, terahertz generation, etc.) [59, 60], optical communications [61], femtochemistry (Nobel Prize in Chemistry 1999) [62], low-phase-noise microwave generation [63], microscopy (confocal, multi-photon, photoacoustic, etc.) [64, 65], nuclear fusion [66], ultra-fast spectroscopy [67], optical coherence tomography [68], eye surgery (corneal, cataract) [69], optical data storage [70] and high-speed electrical testing [71].

Mode-locked fiber lasers advance quickly and it can safely be argued that they will become even more common and influential in both the industrial and scientific applications.

1.3.3 Main Types and Fundamental Dynamics of Mode-Locked Fiber Lasers

Mode-locked fiber lasers can be classified into two categories according to their mode-locking mechanisms as actively mode-locked and passively mode-locked fiber lasers. Actively mode-locked lasers include an active element in the cavity such as an electro-optic or acousto-optic modulator for initialization of pulsed operation. Actively mode-locked lasers can be set to operate at the fundamental cavity frequency or a higher harmonic of the fundamental frequency. Passively mode-locked lasers can be mode-locked using one of several mechanisms. Saturable absorber materials can be placed in the laser cavity to initialize mode-locking. Kerr self-focusing effect can also be utilized to initialize mode-locking

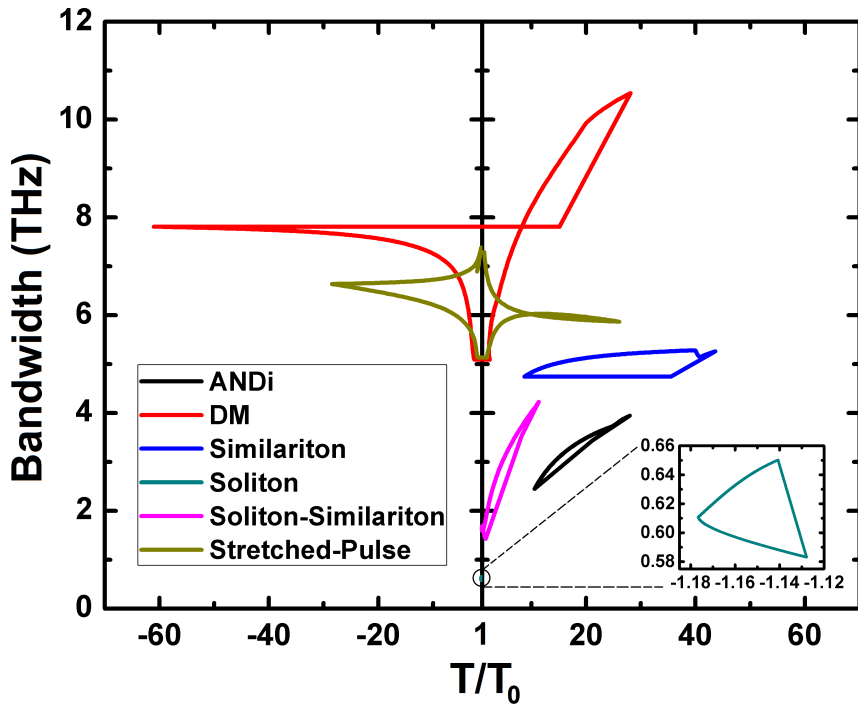


Figure 1.4: Pulse evolution for different types of lasers. Vertical axis is the spectral bandwidth of pulses and horizontal axis is the ratio of pulse durations to the transform-limited pulse durations. Negative values indicate negative frequency-chirp.

of lasers. Nonlinear polarization rotation, which also stems from the Kerr non-linearity, can be used as a virtual saturable absorber for initialization of pulsed operation.

Mode-locked fiber lasers can also be categorized according to their pulse evolution regimes. They can be classified into six categories which are soliton, stretched-pulse, dispersion-managed, similariton, all-normal-dispersion (ANDi) and soliton-similariton fiber lasers. Even though the distinctions are not very clear as similariton, soliton-similariton and stretched-pulse lasers are also utilize some dispersion-management and therefore can be considered dispersion-managed lasers, these categories are still useful and commonly used to classify lasers. Pulse evolutions for the mentioned type of lasers are shown in Fig. 1.4. This figure illustrates the characteristic evolutions for these lasers but they

are only example cases and the actual values of spectral bandwidth and time-bandwidth products depend heavily on the particular laser parameters. Characteristic properties of these lasers will be explained below.

Soliton lasers consist of all-anomalous-dispersion components. Their pulse durations and spectral bandwidths change minimally in one roundtrip. The pulse energy of soliton fiber lasers are usually limited to ~ 100 pJ level. The most important advantages of soliton lasers are their very simple cavity designs, which makes building an all-fiber laser very easy and their ability to produce nearly chirp-free pulses.

Stretched-pulse lasers incorporate fibers with normal and anomalous-dispersion together in the cavity. Pulses reach zero-chirp in the middle of both normal and anomalous-dispersion fibers. They are positively chirped after the zero-chirp point inside the normal-dispersion fiber until the zero-chirp point in the anomalous-dispersion fiber. They are negatively chirped from there on until the zero-chirp point in the normal-dispersion fiber. These pulses are also called “breathers” because of the explained evolution of the pulses. These lasers usually have pulse energies of ~ 1 nJ. They can be built in the all-fiber form easily and compressed pulses can be obtained simply by adjusting the fiber length after the output coupler.

The term “dispersion-managed lasers” usually refers to lasers with normal dispersion fibers and some elements like diffraction gratings for dispersion management. These lasers can be mode-locked with net-anomalous, net-zero or net-normal cavity dispersion and pulse evolution in the laser heavily depends on the net-dispersion of the cavity and pulse energy. Dispersion-managed lasers with high net-anomalous dispersion are somewhat similar to soliton lasers and pulses can be considered to be average solitons. Dispersion-managed lasers with high net-normal dispersion approximates ANDi lasers and cannot be mode-locked without some kind of spectral filtering. Dispersion-managed lasers with near-zero net cavity dispersion can produce very broadband pulses which can be compressed outside the cavity to obtain very short pulses.

Similariton lasers are a special case of dispersion-managed lasers and they

have net-normal cavity dispersion. Pulses evolve self-similarly in the similariton lasers and have approximately parabolic temporal and spectral shapes. When the output is taken after the gain fiber, similariton lasers generates linearly chirped broadband pulses, which can be compressed outside the cavity.

All-normal-dispersion lasers consist of elements with normal dispersion only. They usually include a spectral filter in addition to regular mode-locking elements to undo the spectral broadening caused by Kerr nonlinearity. Spectral filter shortens the pulses also in the temporal domain since the pulses are chirped. ANDi lasers generate highly chirped pulses with steep edges. Highest pulse energies are reached by ANDi lasers since the nonlinearity can be kept low due to long pulse durations.

Soliton-similariton lasers consist of passive fibers with anomalous-dispersion and gain fiber with normal-dispersion. They also include a spectral filter in the cavity. Pulses evolve into a soliton in the passive fiber. They get amplified and propagates self-similarly in the gain fiber, get shortened by the mode-locking element and spectral filter in spectral and temporal domains and enter the anomalous-dispersion fiber again. Due to attractive nature of both soliton and self-similar propagations, soliton-similariton lasers offer very good noise performance [45].

1.4 Femtosecond Frequency Combs

Femtosecond frequency combs are tools that revolutionized optical frequency metrology and as a recognition of this revolution, half of the Nobel Prize in Physics 2005 was awarded to John L. Hall and Theodor W. Hensch “for their contributions to the development of laser-based precision spectroscopy, including the optical frequency comb technique”. The history of optical frequency measurements can be found in an article by Hall and Nobel Lecture by Hensch [72, 73]. Femtosecond frequency combs depend on a very simple principle: Fourier transform of a train of pulses is a comb-like structure in the frequency domain. This

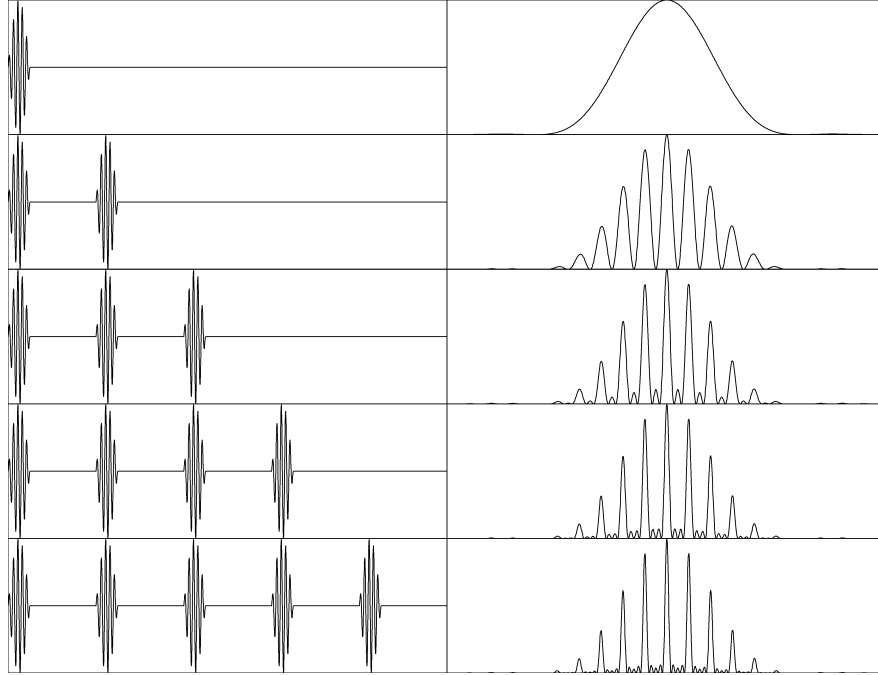


Figure 1.5: The electric field of pulses (left column) and the corresponding spectra (right column).

is illustrated in Fig. 1.5. In this figure, the electric field of pulses and the corresponding spectra are shown. Note that as the number of pulses increase, the comb lines get narrower. The comb spacing is independent of the carrier frequency and depends only on the repetition frequency of the pulses. If all the pulses are identical as in Fig. 1.5, frequency of the comb lines correspond to an exact integer multiple of the repetition frequency. But usually this is not the case, phase of the electric field shifts with respect to the pulse envelope due to the chromatic dispersion and this causes all the comb lines to be shifted by a fixed amount that is called the carrier-envelope-offset frequency [74]. The frequency of the comb lines in this case can be written as such:

$$f(n) = n \times f_R + f_{ceo} \quad (1.19)$$

where n is the integer multiple, f_R is the repetition frequency of the pulses and f_{ceo} is the carrier-envelope-offset frequency.

The challenge was to obtain and stabilize the carrier-envelope-offset frequency. This became easy with the generation of octave-spanning spectrum using the

photonic crystal fibers [75]. First stabilized femtosecond frequency comb was demonstrated in 2000 [76]. Firstly, 300 THz-wide spectrum was generated using a Ti:Sapphire laser and a piece of photonic crystal fiber. Then, the low-frequency end of the spectrum was frequency-doubled and beaten with the high-frequency end of the spectrum. The f_{ceo} was obtained using the beat signal and stabilized. This setup to obtain f_{ceo} is called an $f - 2f$ interferometer and it is currently the most commonly employed method for this purpose.

First stabilized frequency combs were generated using Ti:Sapphire lasers and they usually cover the region of 500-1200 nm. They are followed by many others notably Er-fiber laser based combs which cover 1000-2000 nm region and Yb-fiber laser based combs which cover 700-1400 nm region. Frequency combs that covers other regions of the spectrum are also available. Through difference frequency generation using an Er-fiber laser comb, a tunable frequency comb that can be used up to 17 μm wavelength has been demonstrated [77]. Other methods of producing mid-infrared frequency combs are discussed in [78]. Frequency combs in the ultraviolet and extreme ultraviolet regions were also produced via high harmonic generation [79–81].

Femtosecond frequency combs have found many other applications. Some of the applications of frequency combs can be listed as: attosecond pulse generation [82], optical clocks [83,84], astronomical spectrograph calibration [85], spectroscopy [86], time/frequency transfer [87], long range absolute distance measurement [88], length calibration of gauge blocks [89], surface-profile metrology [90] and next generation of formation-flying satellite missions [91].

Femtosecond frequency combs have advanced tremendously, found many applications and became a common laboratory equipment in only one decade. They will open new doors for ultra-precise measurements and enable us to understand the universe better than ever. Some theories predict that the fine structure constant changes with time and even though measurements performed with frequency combs have not shown a drift, the upper limit for the drift rate have been improved by a factor of ten [92]. The unprecedented precision reached by frequency combs will enable us to test the constancy of “physical constants” and may help

us discover new physical phenomena.

Chapter 2

Numerical Simulations

Numerical simulations have a very important place in physics to understand underlying processes in a particular situation and simulations enable us to predict new phenomena and make new designs. In this chapter, different models that are used for modelling optical pulse propagation in optical fibers will be reviewed and the simulation code that is developed to simulate ultrafast fiber lasers and fiber amplifiers will be explained in detail. This chapter is partially based on [2, 3, 5].

2.1 Finite-Difference Methods

Finite-difference methods are widely used for simulating electromagnetic wave propagation. Finite-difference methods solve Maxwell equations directly in time domain with small number of approximations and therefore they are more accurate than other methods. In fiber optics, they are particularly useful for modelling wavelength-division-multiplexed (WDM) systems and few-cycle optical pulse propagation, where slowly-varying envelope approximation is invalid. Main draw-back of finite difference methods for optical propagation modelling is the necessity of very small grid size (< 1 fs), which limits their usage. Pseudo-spectral methods are more commonly used for modelling optical pulse propagation in fibers, since optical pulses are usually much longer than one optical cycle and

slowly-varying envelope approximation is valid.

2.2 Pseudo-Spectral Methods

Pseudo-spectral methods are usually the first choice for numerical modelling of optical pulse propagation in optical fibers by solving the nonlinear Schrödinger equation (NLSE) or the generalized nonlinear Schrödinger equation (GNLSE). They can be used to simulate propagation of optical pulses that are sufficiently longer than one optical cycle, which means pulses that are longer than ~ 10 fs can be modelled with this group of methods.

In pseudo-spectral methods, NLSE and GNLSE are solved by handling linear effects in frequency domain and handling intensity-dependent nonlinear effects in time domain. Fast Fourier transform (FFT) is used to go back and forth between time and frequency domains. Two different pseudo-spectral methods will be explained in detail.

2.2.1 Split-Step Fourier Method

Split-step Fourier method is the most popular method that is used for solving NLSE and GNLSE. NLSE and GNLSE can be written in terms of linear and nonlinear operators as

$$\frac{\partial A}{\partial z} = (\hat{D} + \hat{N})A \quad (2.1)$$

where \hat{D} is a differential operator that includes the effect of the chromatic dispersion, loss or gain and \hat{N} is a nonlinear operator that includes the effect of fiber nonlinearities. These operators are given by

$$\hat{D} = -\frac{i\beta_2}{2} \frac{\partial^2}{\partial T^2} \quad (2.2)$$

$$\hat{N} = i\gamma|A|^2 \quad (2.3)$$

for NLSE and given by

$$\hat{D} = -\frac{\alpha}{2} - \left(\sum_{n \geq 2} \beta_n \frac{i^{n-1}}{n!} \frac{\partial^n}{\partial t^n} \right) \quad (2.4)$$

$$\hat{N} = i\gamma \frac{1}{A} \left(1 + \frac{1}{\omega_0} \frac{\partial}{\partial t} \right) \left((1 - f_R)A|A|^2 + f_RA \int_0^\infty h_R(t')|A(z, t - t')|^2 dt' \right) \quad (2.5)$$

for GNLSE. The split-step Fourier method treats dispersive and nonlinear effects separately and they are assumed to act independently over a small propagation distance. In the simplest implementation of split-step Fourier method, the propagation from z to $z + h$ is performed in two separate steps. In the first step, nonlinear operator acts alone and in the second step linear operator acts alone. Mathematically, this can be written as

$$A(z + h, T) \approx \exp(h\hat{D}) \exp(h\hat{N})A(z, T) \quad (2.6)$$

This split-step Fourier method is locally accurate to second order in the step-size h , which means that it is globally accurate to first order in the step-size h .

A more accurate implementation of the split-step Fourier method is achieved by evaluating the propagation from z to $z + h$ in three steps. In the first step, linear operator acts alone for a propagation distance of $h/2$. In the second step, nonlinear operator acts alone for a propagation distance of h and lastly another linear step of $h/2$ is taken. This modified procedure is called the symmetrized split-step Fourier method and can be written mathematically as

$$A(z + h, T) \approx \exp\left(\frac{h}{2}\hat{D}\right) \exp\left(\int_z^{z+h} \hat{N}(z') dz'\right) \exp\left(\frac{h}{2}\hat{D}\right) A(z, T) \quad (2.7)$$

Symmetrized split-step Fourier method is locally accurate to third order in the step-size h , which means that it is globally accurate to second order in the step-size h .

There are also higher-order split-step Fourier method implementations which use some form of extrapolation. The scheme introduced by Blow and Wood [93] is one of the popular schemes. In the Blow-Wood scheme, four forward steps of length h is followed by a backward step of length $2h$ and four more forward steps

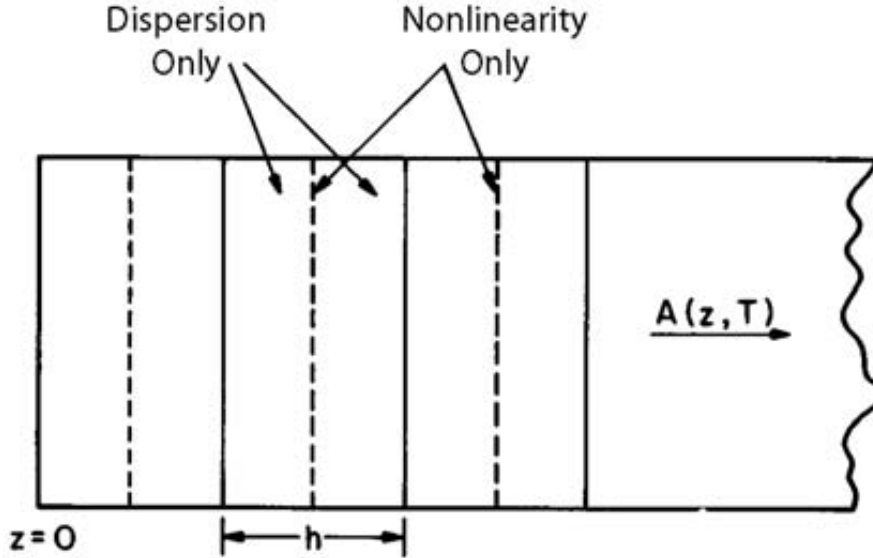


Figure 2.1: Schematic illustration of the symmetrized split-step Fourier method used for numerical simulations [2].

of length h are taken. This scheme is globally accurate to fourth order in the step size h .

Accuracy of all the schemes explained here also depends on the method that is used for integration in the nonlinear step and cannot exceed the accuracy of the integration method.

2.2.2 Fourth-Order Runge-Kutta in the Interaction Picture Method

In quantum mechanics, the interaction picture is an intermediate picture between Schrödinger and Heisenberg pictures that was proposed by Dirac and is also known as the Dirac picture. In the interaction picture, both the quantum states and the operators carry time dependence. The state vectors are transformed only by the free part of the Hamiltonian and the transformed state vectors evolve in time according to the interaction part of the Hamiltonian. The interaction picture allows operators to act on the state vector at different times.

Fourth-order Runge-Kutta in the interaction picture method (RK4IP) is a method that was developed to solve the Gross-Pitaevskii equation, which is a non-linear partial differential equation that describes the dynamics of Bose-Einstein condensates. The time-dependent Gross-Pitaevskii equation can be written as

$$i\hbar \frac{\partial \Psi(\mathbf{r}, t)}{\partial t} = \left(-\frac{\hbar^2}{2m} \nabla^2 + V(\mathbf{r}) + g|\Psi(\mathbf{r}, t)|^2 \right) \Psi(\mathbf{r}, t) \quad (2.8)$$

The Gross-Pitaevskii equation has a similar structure to NLSE and RK4IP method was adapted to solve NLSE and GNLSE [3].

Field envelope A is transformed into the interaction picture representation A_I in terms of the previously defined linear operator \hat{D} and nonlinear operator \hat{N} as

$$A_I = \exp\left(-(z - z')\hat{D}\right) A \quad (2.9)$$

where z' is the separation distance between the interaction and normal pictures. Differentiating A_I gives the evolution of A_I

$$\frac{\partial A_I}{\partial z} = \hat{N}_I A_I \quad (2.10)$$

where

$$\hat{N}_I = \exp\left(-(z - z')\hat{D}\right) \hat{N} \exp\left((z - z')\hat{D}\right) \quad (2.11)$$

A straight-forward implementation of these equations using a fourth-order Runge-Kutta method requires 16 FFTs to be performed per propagation step. However, the number of required FFTs can be reduced to 8 by setting the separation distance $z' = z + h/2$. Even higher-order Runge-Kutta methods can be used but the number of necessary FFTs cannot be reduced for higher-order methods.

One propagation step from z to $z + h$ is performed by evaluating the equations

below:

$$A_I = \exp\left(\frac{h}{2}\hat{D}\right) A(z, T) \quad (2.12)$$

$$k_1 = \exp\left(\frac{h}{2}\hat{D}\right) \left[h\hat{N}(A(z, T))\right] A(z, T) \quad (2.13)$$

$$k_2 = h\hat{N}(A_I + k_1/2)[A_I + k_1/2] \quad (2.14)$$

$$k_3 = h\hat{N}(A_I + k_2/2)[A_I + k_2/2] \quad (2.15)$$

$$k_4 = h\hat{N}\left(\exp\left(\frac{h}{2}\hat{D}\right)(A_I + k_3)\right) \exp\left(\frac{h}{2}\hat{D}\right)[A_I + k_3] \quad (2.16)$$

$$A(z + h, T) = \exp\left(\frac{h}{2}\hat{D}\right) [A_I + k_1/6 + k_2/3 + k_3/3] + k_4/6 \quad (2.17)$$

The RK4IP algorithm is locally accurate to fifth order in the step-size h and it is globally accurate to fourth order in the step-size h . An implementation of this algorithm in MATLAB is given in Appendix A. The given implementation uses the analytical form given in [4] as the Raman response function. It was implemented to simulate supercontinuum generation in photonic crystal fibers.

2.2.3 Performance Comparison of the Pseudo-Spectral Computational Schemes

The accuracy and computational efficiency of the methods that are mentioned before have been compared in reference [3]. As the test case for NLSE, a second-order soliton has been chosen since an analytical solution exists in this case. Simulations was performed using different implementations and the results were compared to the analytical solution. The average relative intensity error ϵ is used for comparisons and it is defined by

$$\epsilon = \frac{\sum_{k=1}^N ||A_k^{comp}|^2 - |A_k^{true}|^2|/N}{\max(|A^{true}|^2)} \quad (2.18)$$

where N is the total number of temporal grid points, A_k^{true} is the analytically calculated solution for k^{th} grid point and A_k^{comp} is the result of computer simulation for k^{th} grid point. Average relative error for some implementation schemes

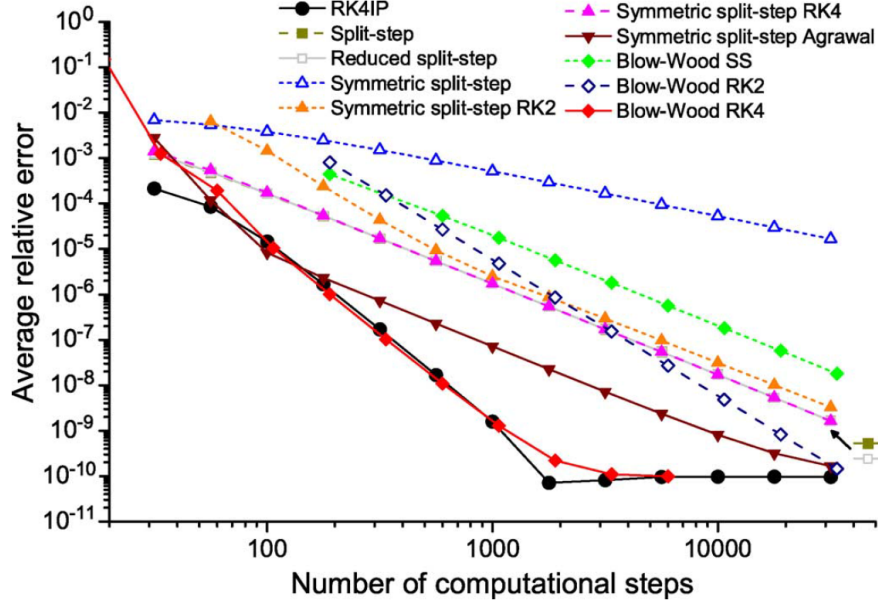


Figure 2.2: Graph of average relative errors for different schemes versus number of computational steps for simulation of a second-order soliton [3].

is given in Fig. 2.2. SS, RK2 and RK4 shows the methods that have been used for integration of nonlinear operator. SS corresponds to trapezoidal integration, RK2 corresponds to second-order Runge-Kutta method and RK4 corresponds to fourth-order Runge-Kutta method. Most accurate methods appear to be the RK4IP and Blow-Wood RK4 methods and they both exhibit an asymptotic slope of -4 until the machine accuracy is reached at $\epsilon \approx 10^{-10}$. For small number of steps, the most accurate method seems to be the RK4IP method.

As the test case for GNLSE, broadband supercontinuum generation in a PCF is simulated. In this case, same definition was used for ϵ and the result of RK4IP algorithm for $N = 316228$ was used as A^{true} . Results are shown in Fig. 2.3. In this test case, RK4IP is distinctly the most accurate algorithm. Numerical accuracy limit is reached at $\epsilon \approx 10^{-8}$.

Since the computational effort to take one propagation step is different for every scheme, the given graphics does not mean much in terms of computational efficiency. In Fig. 2.4, average relative errors versus the computational time which is normalized with the time necessary to calculate one FFT. In this graph, it can

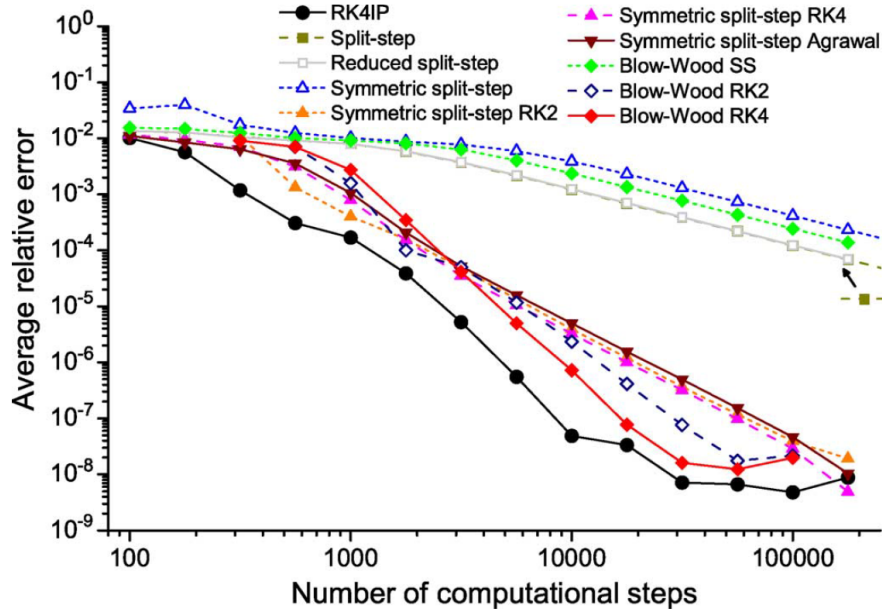


Figure 2.3: Graph of average relative errors for different schemes versus number of computational steps for simulation of broadband supercontinuum generation in PCF [3].

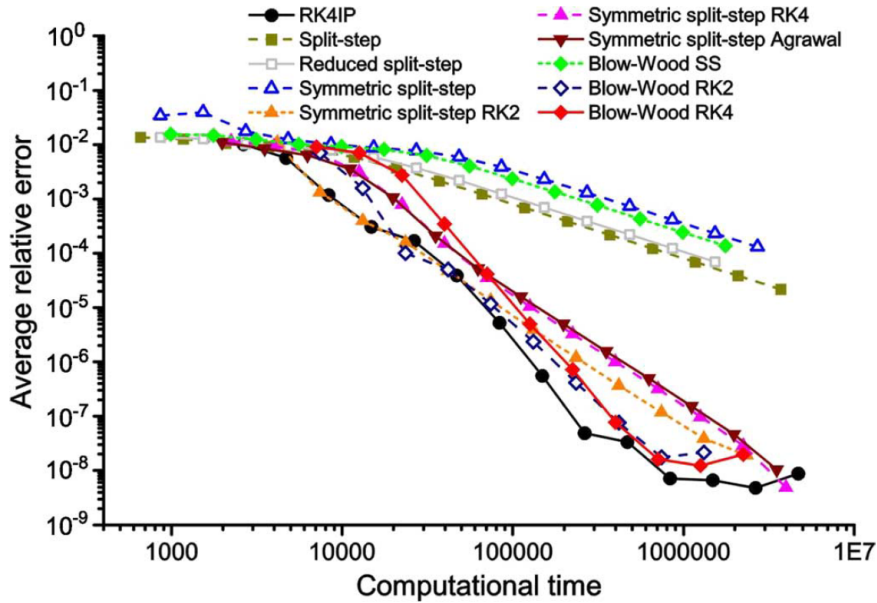


Figure 2.4: Graph of average relative errors for different schemes versus normalized computation time for simulation of broadband supercontinuum generation in PCF [3].

be seen that RK4IP method is computationally the most efficient algorithm for high accuracy simulations and RK4IP, and all schemes except the simple symmetric split-step implementation competitively efficient for low accuracy simulations.

Fixed step sizes were used for all the simulations above. Implementations with adaptive step-size control might perform better since much larger steps can be used for regions where nonlinearity is weak. An implementation of RK4IP algorithm with adaptive step-size control is given in Appendix B and will be explained in detail later in this chapter.

2.3 Ultrashort Pulse Propagator

A pulse propagation simulation software has been developed which solves a simplified version of GNLSE and it has been used to simulate fiber lasers and fiber amplifiers for more than 6 years and freely available for academic use on the web [94]. It is called ‘‘Ultrashort Pulse Propagator’’ and it solves the equation given below

$$\frac{\partial A}{\partial z} + \frac{\alpha}{2}A + \frac{i\beta_2}{2}\frac{\partial^2 A}{\partial T^2} - \frac{\beta_3}{6}\frac{\partial^3 A}{\partial T^3} = i\gamma \left(|A|^2 A + \frac{i}{\omega_0} \frac{\partial}{\partial T} (|A|^2 A) - T_R A \frac{\partial |A|^2}{\partial T} \right) \quad (2.19)$$

where T_R is the Raman response time, which is given by

$$T_R \equiv \int_0^\infty tR(t)dt \approx f_R \int_0^\infty th_R(t)dt = f_R \left. \frac{d(\text{Im}\tilde{h}_R)}{d(\Delta\omega)} \right|_{\Delta\omega=0} \quad (2.20)$$

The experimental value for Raman response time is about 3 fs [95]. The solution is approximated using symmetrized split-step Fourier method with fourth-order Runge-Kutta method used for integration of nonlinear operator. Modelled equation includes the effects of second-order dispersion, third-order dispersion, loss and gain, Kerr nonlinearity, self-steepening and simplified Raman scattering. Gain is implemented as saturable and it has a wavelength dependence with a Lorentzian shape. Gain factor for frequency f is calculated using the equation below

$$G(f) = 1 + \frac{g_0 - 1}{1 + ((f - f_0)/\Delta f)^2} \frac{1}{1 + E_{in}/E_{sat}} \quad (2.21)$$

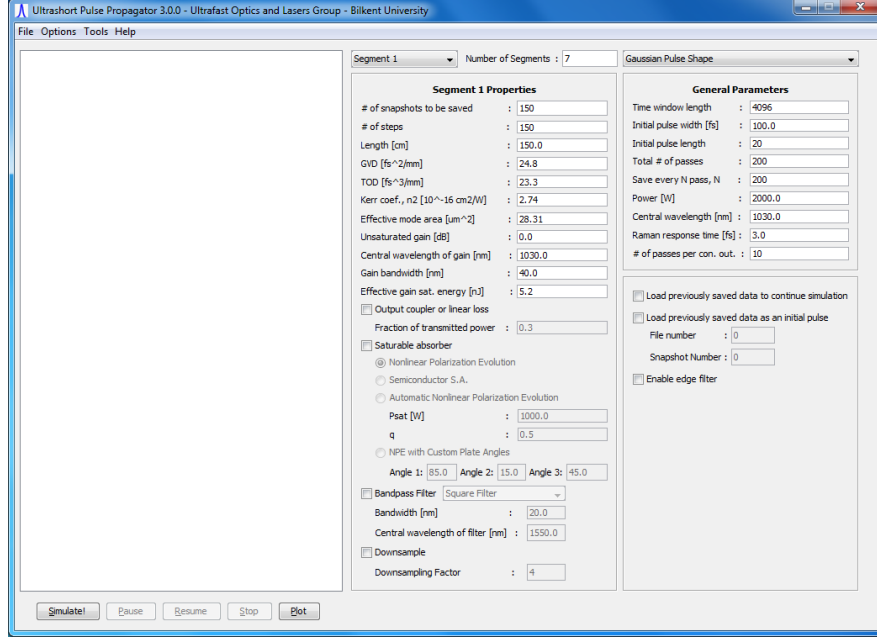


Figure 2.5: Main screen of Ultrashort Pulse Propagator 3.0.0.

where f_0 is the central frequency of the gain, g_0 is the small-signal gain at f_0 , Δf is the half-width at half-maximum (HWHM) of the gain spectrum, E_{in} is the total input energy and E_{sat} is the gain saturation energy.

The effects of saturable absorbers, output couplers and spectral filters are included in the code as multiplications by transmission functions. Output couplers are simply implemented as multiplication of the propagating field by the transmission ratio given by the user. Different saturable absorber models are included. The power-dependent transmission function for semiconductor saturable absorber (SSA) is

$$T_{SSA}(P) = 1 - \frac{q}{1 + P/P_{sat}} \quad (2.22)$$

where P is instantaneous power of the signal, q is the modulation depth and P_{sat} is the saturation power of the saturable absorber. The power-dependent transmission function for nonlinear polarization evolution (NPE) is

$$T_{NPE}(P) = 1 - q \cos^2 \left(\frac{\pi}{2} \frac{P}{P_{sat}} \right) \quad (2.23)$$

again with the same definitions of terms. As an example, the transmission curves for both cases are shown in Fig. 2.6 for $q = 0.7$ and $P_{sat} = 1000$ W. There are

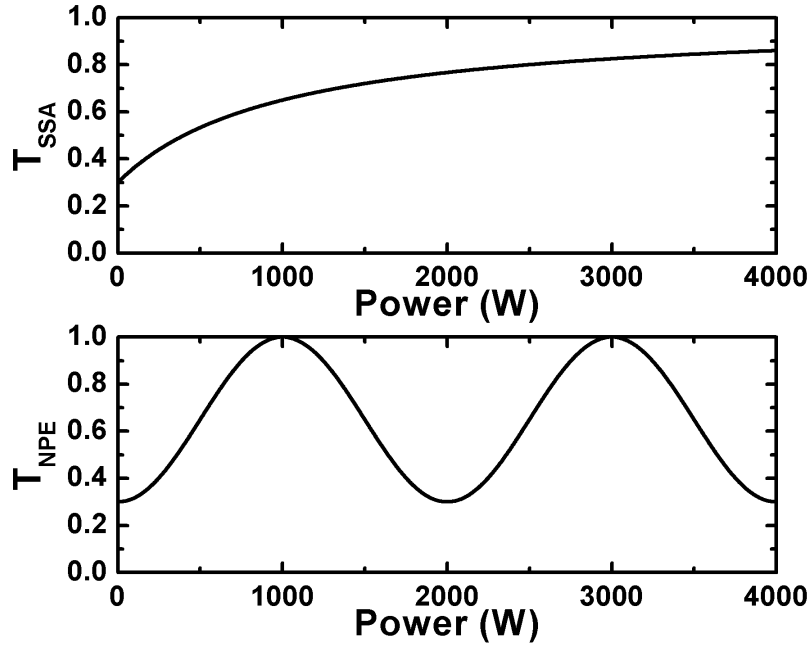


Figure 2.6: Transmission versus incident power graphs for SSA and NPE for the given parameters.

three types of spectral bandpass filters implemented in the program which have square, Gaussian and parabolic shapes. Implementation of spectral filters are simple using FFTs. FFT of the incident field is calculated and multiplied by the spectral transmission function which is calculated according to the parameters that are given by the user. Lastly, inverse FFT of the result is calculated and assigned as the new propagating field.

2.4 Simulation of Supercontinuum Generation Using RK4IP Algorithm

Supercontinuum generation is a highly nonlinear and complicated process where many effects act together and output of the process is extremely sensitive to the input parameters. Highly accurate numerical methods are necessary for simulations due to the mentioned sensitivity of the process. In the previous section, RK4IP was shown to be the most efficient algorithm for simulations that require

high accuracy and a simulation program that uses RK4IP algorithm is developed. Two versions of the algorithm are presented. First version that is given in Appendix A uses constant step-size for propagation. Second version utilizes an adaptive step-size control algorithm and is given in Appendix B. Developed programs solve GNLSE with arbitrary orders of chromatic dispersion and an accurate stimulated Raman scattering model by D. Hollenbeck and C.D. Cantrell [4]. Multiple-vibrational-mode model that is presented fits the experimental Raman

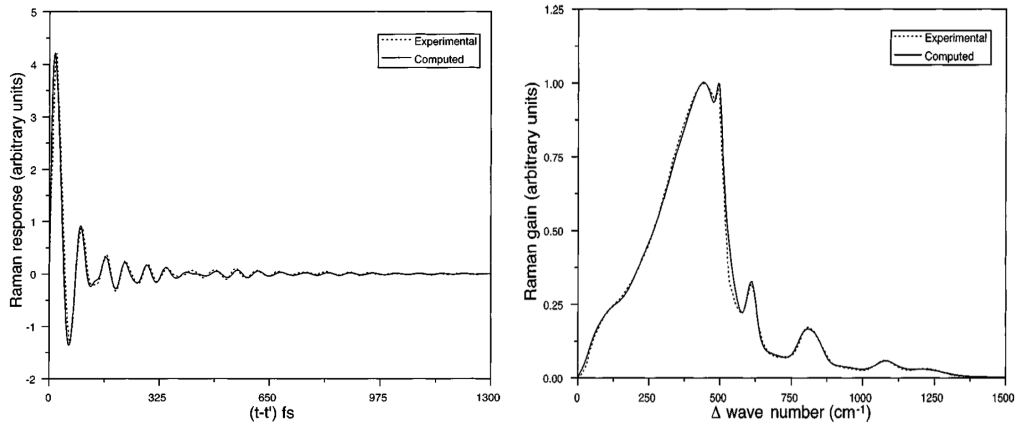


Figure 2.7: Experimental and computed Raman response function and Raman gain [4].

response function by Stolen et.al. [25] using the convolutions of 13 Gaussian and Lorentzian functions. Raman response function $h_R(t)$ is calculated by

$$h_R(t) = \sum_{i=1}^{13} \frac{A'_i}{\omega_{\nu,i}} \exp(-\gamma_i t) \exp(-\Gamma_i^2 t^2/4) \sin(\omega_{\nu,i} t) \theta(t) \quad (2.24)$$

where A'_i is the amplitude of i^{th} vibrational mode, $\omega_{\nu,i}$ is the central frequency of i^{th} vibrational mode, γ_i is the Lorentzian linewidth for mode i , Γ_i is the Gaussian linewidth for mode i and $\theta(t)$ is the unit step function. Numerical values of the parameters are given in Table 2.1.

Calculation of Raman contribution includes the convolution of the response function with the pulse envelope. Convolution is computationally expensive when it is implemented in the naive way. Convolutions can be calculated much faster

Table 2.1: Values of the parameters used in the intermediate-broadening model*

Mode Number i	Component Position (cm^{-1})	Peak Intensity A_i	Gaussian FWHM (cm^{-1})	Lorentzian FWHM (cm^{-1})
1	56.25	1.00	52.10	17.37
2	100.00	11.40	110.42	38.81
3	231.25	36.67	175.00	58.33
4	362.50	67.67	162.50	54.17
5	463.00	74.00	135.33	45.11
6	497.00	4.50	24.50	8.17
7	611.50	6.80	41.50	13.83
8	691.67	4.60	155.00	51.67
9	793.67	4.20	59.50	19.83
10	835.50	4.50	64.30	21.43
11	930.00	2.70	150.00	50.00
12	1080.00	3.10	91.00	30.33
13	1215.00	3.00	160.00	53.33

* $A_i = A'_i/\omega_{\nu,i}$, $\Gamma_i = \pi c \times (\text{Gaussian FWHM})$, $\gamma_i = \pi c \times (\text{Lorentzian FWHM})$ and $\omega_{\nu,i} = 2\pi c \times (\text{component position})$

by using the convolution theorem. According to the convolution theorem, convolution of two functions can be calculated through use of Fourier transforms,

$$f * g = \mathcal{F}^{-1}\{\mathcal{F}\{f\} \cdot \mathcal{F}\{g\}\} \quad (2.25)$$

Since Fourier transforms can be calculated very fast with the usage of FFT algorithms, convolutions can be accelerated by orders of magnitude with an implementation that uses FFT. This is used in the implementation of the given simulation.

Experimental and simulated spectra for supercontinuum generation in 30 cm-long SC-3.7-975 fiber using 35 fs pulses with 24 kW peak power are given in Fig. 2.8. The similarity of the two spectra is striking and shows the quality of the used model. The difference in the spectra is mostly caused by the noise floor of the optical spectrum analyzer that was used for the measurements, which is in the order of 0.01 for 600 nm and decreases as the wavelength increases.

As mentioned before, usage of adaptive step-size control might decrease the necessary computational effort to reach a given computational accuracy. Adaptive step-size control algorithms need some measure to estimate the error and adjust the step size accordingly. There are different approximations to this problem.

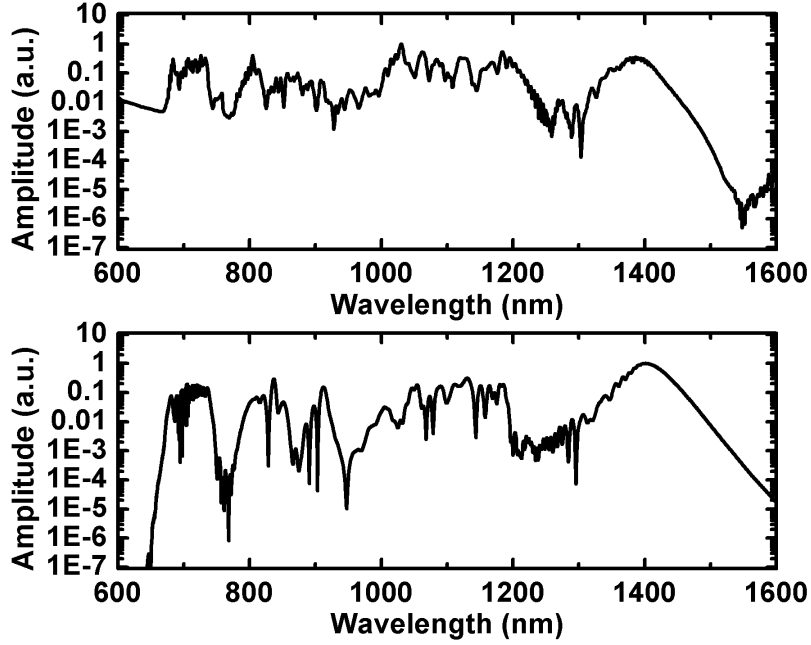


Figure 2.8: Experimental (upper fig.) and simulated (lower fig.) supercontinuum spectra obtained from 30 cm-long SC-3.7-975 photonic crystal fiber.

The local error method tries to estimate the error by taking a coarse step, then propagating the same amount in two steps with half the step size and comparing them to estimate the error. The conservation quantity error (CQE) method for adaptive step-size control, which is proposed by A. M. Heidt [5], is an improvement over the local error method and uses the total photon number as a measure of local error to increase the computational efficiency. A second version of the presented simulation is implemented using this method. Local error and CQE methods are explained below.

As mentioned before, local error method propagates a distance in three steps: firstly whole propagation is done in one step and the solution A_{coarse} is calculated, then it is propagated again in two half steps and the solution A_{fine} is calculated. Local error is approximated by

$$\delta = \frac{|A_{\text{fine}} - A_{\text{coarse}}|}{|A_{\text{fine}}|} \quad (2.26)$$

The step-size is adjusted as such: If $\delta > 2\delta_G$ then last step is discarded and repeated with half the step-size, if $\delta_G < \delta < 2\delta_G$ then h is divided by $2^{(1/\eta)}$, if

$\delta < 0.1\delta_G$ then h is multiplied by $2^{(1/\eta)}$, where δ_G is the goal error and η is the degree of local accuracy of the used method in the step size. $\eta = 3$ for symmetrized split-step Fourier method and $\eta = 5$ for RK4IP method. Both coarse and fine solutions can be used for increasing the accuracy of the computation through extrapolation and a higher-order accurate solution can be found:

$$A_{\eta+1} = \frac{2^{\eta-1}}{2^{\eta-1} - 1} A_{\text{fine}} - \frac{1}{2^{\eta-1} - 1} A_{\text{coarse}} \quad (2.27)$$

GNLSE conserves the photon number in the absence of loss and CQE method exploits this property of GNLSE to decrease the necessary computational effort. Even if linear loss exists in the medium, the true photon number can be calculated easily. Change in the photon number in a step can be used as a measure of local error. In the absence of loss, absolute photon number error can be calculated as,

$$\Delta_{\text{Ph}} = |P_{\text{calc}}(z+h) - P_{\text{true}}(z+h)| \quad (2.28a)$$

$$= \left| \int \left(|\tilde{A}_{\text{calc}}(z+h, \omega)|^2 - |\tilde{A}_{\text{true}}(z+h, \omega)|^2 \right) \times \frac{S(\omega)}{\omega} d\omega \right| \quad (2.28b)$$

$$= \left| \int \left(|\tilde{A}_{\text{calc}}(z+h, \omega)|^2 - |\tilde{A}(z, \omega)|^2 \right) \times \frac{S(\omega)}{\omega} d\omega \right| \quad (2.28c)$$

where $\tilde{A}(z, \omega)$ is the Fourier transform of $A(z, T)$, $S(\omega) = n_{\text{eff}}(\omega)A_{\text{eff}}(\omega)$ and n_{eff} is the frequency-dependent refractive index. Relative photon error, which will be used to adjust the step sizes, is defined as,

$$\delta_{\text{Ph}} = \frac{\Delta_{\text{Ph}}}{P_{\text{true}}} \quad (2.29)$$

The step size is adjusted in the same way as the local error method with the only difference being the usage of δ_{Ph} instead of δ .

Necessary computational times for different implementation schemes are shown in Fig. 2.9. In this figure, local error, CQE and constant step-size methods are compared for RK4IP and symmetrized split-step Fourier methods. RK4IP-CQE method is found to be the most efficient method.

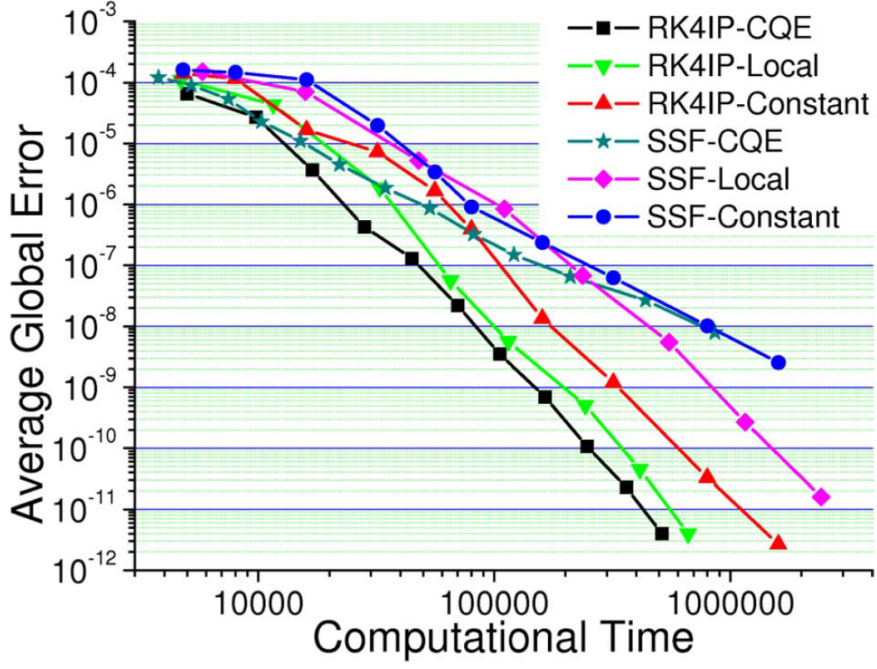


Figure 2.9: Comparison of necessary computational time for supercontinuum generation process in PCF for different implementations of symmetrized split-step Fourier method and RK4IP method [5].

2.5 Improvement of the GNLSE

GNLSE usually gives satisfactorily accurate results but it is not enough to model some aspects of the supercontinuum generation such as the coherence of the output spectra. In order to study the noise properties and coherence of the output spectra, it is necessary to implement the spontaneous Raman scattering and input pulse noise. GNLSE can be modified slightly to include the spontaneous Raman scattering in the following way [96]:

$$\begin{aligned}
& \frac{\partial A}{\partial z} + \frac{\alpha}{2} - \sum_{k \geq 2} \frac{i^{k+1}}{k!} \beta_k \frac{\partial^k A}{\partial T^k} \\
& = i\gamma \left(1 + i\tau_{shock} \frac{\partial}{\partial T} \right) \left(A(z, t) \int_{-\infty}^{\infty} R(T') |A(z, T - T')|^2 dT' + i\Gamma_R(z, T) \right)
\end{aligned} \tag{2.30}$$

The term Γ_R is a multiplicative stochastic variable that is added to model the effect of spontaneous Raman scattering. Γ_R has correlations given by

$$\langle \Gamma_R(\Omega, z) \Gamma_R^*(\Omega', z') \rangle = \frac{2f_R \hbar \omega_0}{\gamma} |\text{Im}[h_R(\Omega)]| [n_{th}(|\Omega|) + \theta(-\Omega)] \delta(z - z') \delta(\Omega - \Omega') \quad (2.31)$$

where $\Omega = \omega - \omega_0$, $n_{th}(\Omega) = [\exp(\hbar\Omega/k_B T) - 1]^{-1}$ and θ is the unit step function. Input pulse shot noise can be implemented as adding one photon per mode with random phase to every spectral discretization bin [96].

Accuracy of the simulations can be increased further with the inclusion of frequency-dependent fiber losses, frequency-dependence of the mode-field area and Kerr coefficient, and polarization effects. It is straight forward to implement frequency-dependent losses since loss is a part of the linear operator and implemented in the frequency domain. To the first order, frequency dependence of mode-field diameter can be included by a simple correction to τ_{shock} [93, 97],

$$\begin{aligned} \tau_{shock} &= \tau_0 + \frac{d}{d\omega} \left[\ln \left(\frac{1}{n_{\text{eff}}(\omega) A_{\text{eff}}(\omega)} \right) \right]_{\omega_0} \\ &= \tau_0 - \left[\frac{1}{n_{\text{eff}}(\omega)} \frac{dn_{\text{eff}}(\omega)}{d\omega} \right]_{\omega_0} - \left[\frac{1}{A_{\text{eff}}(\omega)} \frac{dA_{\text{eff}}(\omega)}{d\omega} \right]_{\omega_0} \end{aligned} \quad (2.32)$$

where $A_{\text{eff}}(\omega)$ is the frequency-dependent mode-field area and $n_{\text{eff}}(\omega)$ is the frequency-dependent effective index.

Chapter 3

Supercontinuum Generation in Photonic Crystal Fibers with Femtosecond Pulses

The possibility of shifting zero-dispersion wavelength (ZDW) to shorter wavelengths than the intrinsic ZDW of silica fibers which is around $1.3 \mu\text{m}$ by choosing appropriate design parameters for cladding of photonic crystal fibers was shown [98]. It was noted that the small mode-field diameters of solid-core PCFs would enhance the Kerr nonlinearity of these fibers compared to standard fibers and this might bring new opportunities [99]. Combination of these effects lead to generation of supercontinuum that spans from 400 nm to 1500 nm with pulses from a Ti:Sa laser at 770 nm with 100 fs duration and 0.8 nJ energy using only 75 cm-long PCF [75]. Efforts to model and analyse the SC generation in PCF have been made and it was found that GNLSE was capable of accurately modelling SC generation in PCF [100].

In this chapter, the important effects behind the supercontinuum generation in photonic crystal fibers will be explained with the help of simulations that solve GNLSE. This chapter is mostly based on [6]. Simulations are performed using the code given in Appendix A. The discussions here applies to PCFs with single

Table 3.1: Dispersion coefficients of SC-3.7-975 fiber for wavelength of 1040 nm.

$$\begin{aligned}\beta_2 &= -7.5946 \text{ fs}^2/\text{mm} \\ \beta_3 &= 78.5925 \text{ fs}^3/\text{mm} \\ \beta_4 &= -101.3403 \text{ fs}^4/\text{mm} \\ \beta_5 &= 110.2014 \text{ fs}^5/\text{mm}\end{aligned}$$

ZDW. However, there are some PCFs with multiple ZDW and the SC generation dynamics for these fibers will not be discussed.

3.1 Supercontinuum Generation Dynamics

Supercontinuum generation in photonic crystal fibers has very rich dynamics that mainly arises from the interplay between chromatic dispersion, Kerr nonlinearity and Raman scattering. Propagation of a 62 fs hyperbolic secant pulse with 2.6 kW peak power and 1040 nm central wavelength in SC-3.7-975 fiber is shown in Fig. 3.2. ZDW of this fiber is 984 nm according to the given data by the manufacturer and dispersion coefficients up to 5th order for 1040 nm wavelength is given in Table 3.1. Dispersion profile is shown in Fig. 3.1.

Input pulse parameters correspond to a third-order soliton. Propagation dynamics for this case will be deconstructed in the rest of this section.

3.1.1 Soliton Fission

For anomalous GVD pumping regime, soliton effects dominate the evolution of pulses in the PCF and soliton fission is the most important effect that causes the spectrum to get broadened. Soliton fission is the break-up of an high-order soliton into several fundamental solitons due to effects that disturb the soliton evolution. In Fig. 3.3, the evolution of the described pulse is shown in the absence of disturbances like higher-order dispersion, self-steepening and Raman scattering. Initially, pulse gets compressed temporally and the spectrum of the

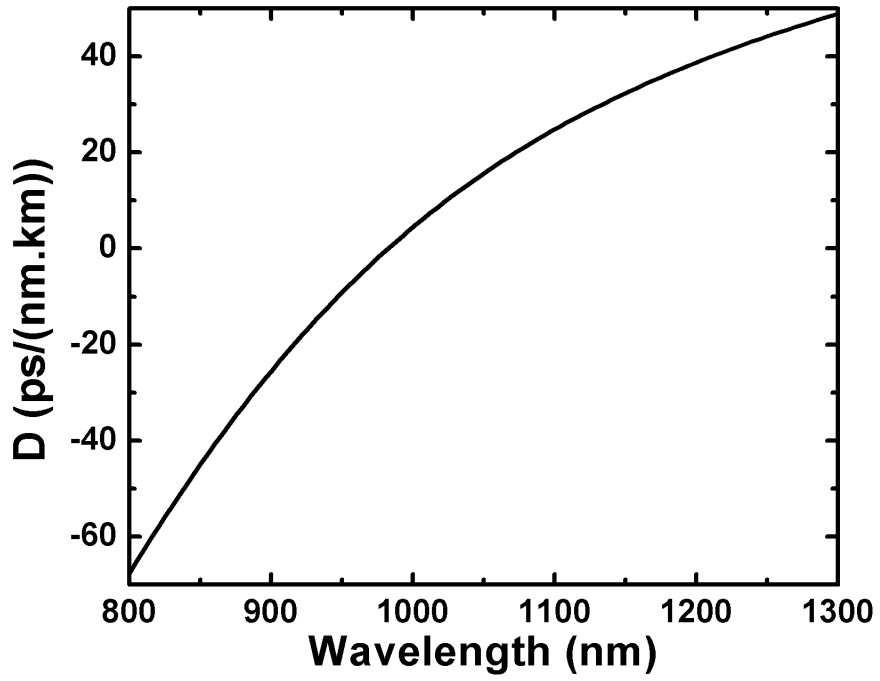


Figure 3.1: Dispersion profile of SC-3.7-975.

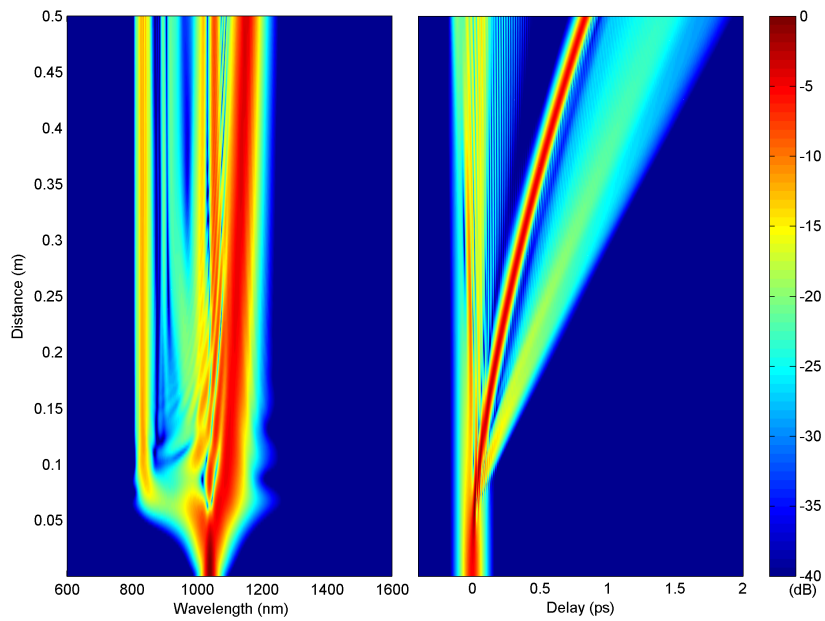


Figure 3.2: Evolution of a third-order soliton in PCF.

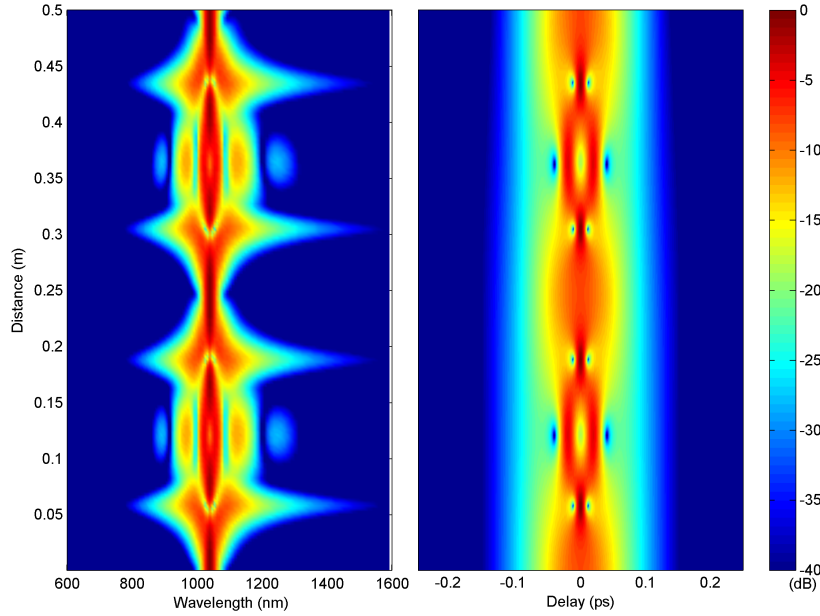


Figure 3.3: Evolution of a third-order soliton in fiber in the absence of higher-order dispersion and Raman scattering.

pulse gets broadened. Pulse recover its original state after one soliton period.

3.1.2 Raman Scattering

Raman scattering is one of the effects that disturb the soliton evolution and induce pulse break up. In Fig. 3.4, propagation of the same initial pulse is shown when the stimulated Raman scattering is taken into account. Pulse cannot recover its initial state and breaks up into several pulses. Three distinct pulses can be seen. First ejected soliton carries most of the energy and it gets further away from other pulses as its wavelength shifts to higher wavelengths through Raman induced self-frequency shift. Spectrum of the pulse continues to broaden as it propagates. Raman scattering is the dominant disturbing effect for long pulses (> 200 fs).

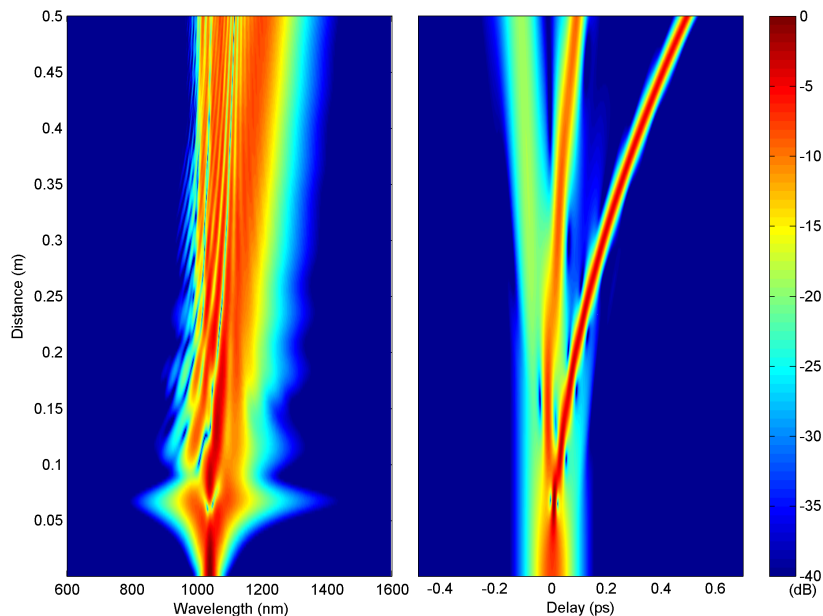


Figure 3.4: Raman scattering induced break up of a third-order soliton in PCF in the absence of higher-order dispersion.

3.1.3 Dispersive Wave Generation

Soliton fission and the Raman scattering cannot explain normal GVD regime spectral structure and the low-intensity temporal background that is observed in SC generation with PCF. It is necessary to consider higher-order dispersion to explain the mentioned properties of SC generation. Higher-order dispersion is the most important effect that disturbs and modifies the soliton evolution for short pulses (< 50 fs). In Fig. 3.5, evolution of the same pulse under the influence of higher-order dispersion and absence of Raman scattering is shown. From the similarity to Fig. 3.2, it can be deduced that higher-order dispersion is the main effect that determines the pulse evolution for this particular case.

Higher-order dispersion modifies the evolution in two ways. It causes the Raman shifted solitons to experience different values of GVD through their evolution and they need to continuously adapt. Higher-order dispersion also cause some energy to be transferred to a resonant region in the normal GVD regime from the solitons [101]. This process is shown to be analogous to the Cherenkov

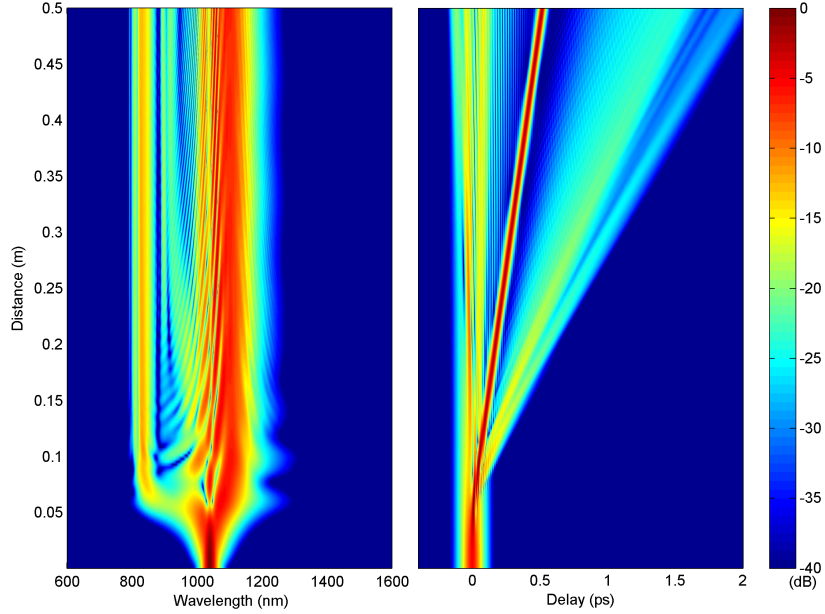


Figure 3.5: Higher-order dispersion induced break up of a third-order soliton in PCF in the absence of Raman scattering.

radiation and the resonance frequency for a soliton can be calculated by solving the equation [102],

$$\beta(\omega_s) - \frac{\omega_s}{\nu_{g,s}} + (1 - f_R)\gamma P_s = \beta(\omega_{\text{DW}}) - \frac{\omega_{\text{DW}}}{\nu_{g,s}} \quad (3.1)$$

where ω_{DW} is the frequency of the generated dispersive wave, P_s is the peak power of the soliton, ω_s is the frequency of the soliton and $\nu_{g,s}$ is the group velocity at ω_s .

3.2 Dependence of Generated Supercontinuum on Input Pulse Parameters

Main effects that contribute to the SC generation have been discussed in the previous section. In this section, dependence of the generated supercontinuum on the input pulse parameters such as central wavelength, pulse duration and initial chirp will be discussed.

3.2.1 Dependence on Pulse Wavelength

The relative positions of the ZDW of PCF and the central wavelength of the input pulse is one of the most critical factors in the SC generation process since it determines the fundamental nature of the propagation in PCF. Numerical simulations are performed to demonstrate how the evolution is modified when the input pulse wavelength is changed. In the simulations, Gaussian pulses with 25 kW peak power and 50 fs FWHM duration with different central wavelengths are propagated through 15 cm-long SC-3.7-975 fiber, which have ZDW of 984 nm according to the provided data. Simulation results for several cases are shown in Fig. 3.6. The central wavelength of the input pulses are varied from 800

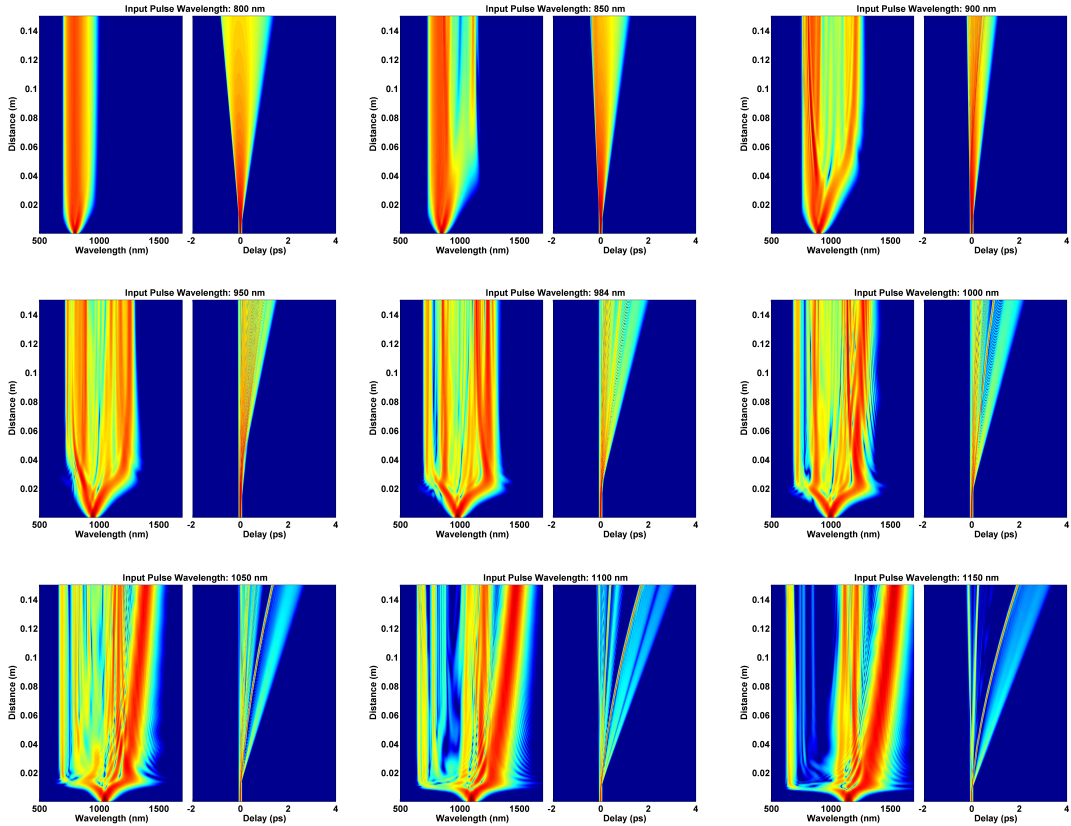


Figure 3.6: Temporal and spectral evolution of pulses with different central wavelengths in PCF with ZDW of 984 nm.

nm to 1150 nm. Variety of the resulting spectra shows the importance of the

dispersion profile of PCF for the SC generation. For input wavelength of 800 nm, Kerr nonlinearity is the dominant effect in the broadening of the spectrum. Since Kerr nonlinearity with normal GVD leads to rapid broadening of the input pulse, spectral broadening is limited. For 850 nm and 900 nm input pulses, Kerr nonlinearity starts the initial broadening. After the initial broadening phase, some of the energy is transferred to the anomalous GVD regime and temporal oscillations on the pulse envelope appear. As the pulse wavelength gets closer to the ZDW, solitonic effects become apparent. As the input pulse wavelength increased further, broader spectra are generated. One may expect that increasing wavelength should decrease the generated spectral bandwidth since increased wavelength means higher anomalous dispersion and smaller soliton number. As it is apparent from the simulations, this is not the whole story. Higher anomalous dispersion also means smaller characteristic dispersion length L_D and more solitons are ejected for the same length of fiber, which leads to higher depletion of the pump wavelength area, more distinct spectral peaks and broader spectra.

3.2.2 Dependence on Pulse Duration

The effect of duration of the chirp-free input pulses will be discussed here with the help of numerical simulations. In the simulations, Gaussian pulses with 25 kW peak power, 1040 nm central wavelength and various durations are propagated through 15 cm-long SC-3.7-975 fiber. Simulation results are shown in Fig. 3.7. As it is seen from the simulation results, all the spectral components of the generated SC is seeded by the initial broadening phase for short pulses, whereas most of the generated spectra is started from noise for long pulses. Longer pulses correspond to pulses with higher soliton orders for constant peak power and this also contributes to the complex temporal and spectral structure observed for long pulses. The effects of the pulse duration will be discussed further during the discussion of the coherence of the generated SC.

Transform-limited input pulses are used for the discussions up to this point. The SC generation with chirped input pulses was studied numerically by Corwin et. al. [103]. In the simulations, it has been found that the broadest spectra

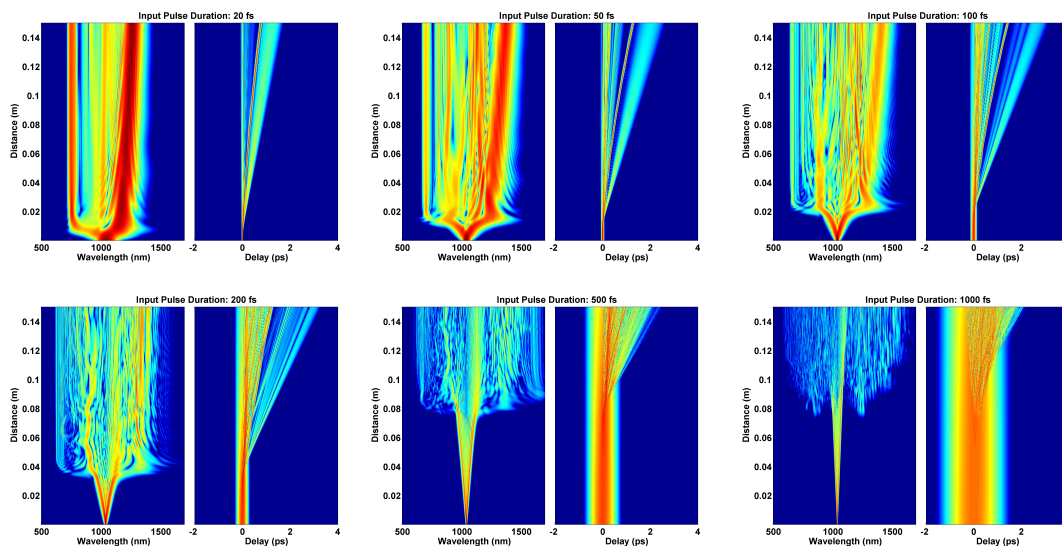


Figure 3.7: Temporal and spectral evolution of pulses with different initial durations in PCF.

is generated by near-transform-limited pulses with slight positive chirp around $+100 \text{ fs}^2$ for constant input pulse energy and bandwidth.

3.2.3 Noise Properties of the Generated Supercontinuum

Noise properties of the generated SC is a big concern for some applications like optical frequency metrology. In this section, dependence of the noise properties of the generated SC on the input pulse parameters will be discussed based on numerical simulations.

Amplitude, phase and timing noise of the generated SC were studied numerically in [103, 104]. In these studies, it has been found that noise contribution from the spontaneous Raman scattering was very small compared to the contribution of the input pulse shot noise. In [103], firstly both effects are taken into account and relative intensity noise (RIN) is calculated for a sample case. When only the spontaneous Raman scattering is neglected, calculated RIN reduced less than 1 dB. When only the input shot noise is neglected, calculated RIN reduced

by 20 dB. It is also found that spectral distribution of RIN has a very complex structure. There are consistently low RIN spectral areas, which correspond to the input pulse wavelength and the Raman soliton on the infrared side of the spectrum. In both studies, the dependence of the noise on the pulse energy and input pulse chirp is investigated. Minimum RIN is found to be achieved for slightly positive input pulse chirp around $\sim 100 \text{ fs}^2$. RIN is found to increase exponentially with both pulse energy and pulse chirp. RIN is also found to increase exponentially with increasing spectral bandwidth. In [104], phase noise, timing jitter, amplitude noise and carrier-envelope-offset phase jitter are found to be highly correlated with RIN and the statements about RIN holds for other types of noise. The way to reach the largest spectral bandwidth with minimal noise is also investigated in this study. When the spectral bandwidth is increased by 10% increasing the fiber length, noise increases by $\sim 12 \text{ dB}$. When the spectral bandwidth is increased by increasing the pulse energy, noise increases by $\sim 8 \text{ dB}$. When the spectral bandwidth is increased by reducing the input pulse chirp towards the optimum value of $+100 \text{ fs}^2$, the noise decreases by $\sim 12 \text{ dB}$. As a conclusion, as long as the pulse duration is kept constant, wide spectrum should be obtained using high energy pulses and short fiber length for minimum noise.

It was shown that the amplitude and phase fluctuations across the supercontinuum spectrum can also be characterized using interferometric measures [105]. In this study, two independently generated supercontinua interfered and separated spectrally. Then, the fringe visibility is used as a measure of SC phase stability. It has been shown that this measure of SC phase stability can be calculated using numerical simulations [106]. The modulus of the complex degree of first-order coherence is defined by

$$|g_{12}^{(1)}(\lambda, t_1 - t_2)| = \left| \frac{\langle E_1^*(\lambda, t_1) E_2(\lambda, t_2) \rangle}{\sqrt{\langle |E_1(\lambda, t_1)|^2 \rangle \langle |E_2(\lambda, t_2)|^2 \rangle}} \right| \quad (3.2)$$

The angular brackets denote ensemble average of independently generated SC pairs. To calculate the fringe visibility at zero path difference, t_1 and t_2 should be equal.

The dependence of the coherence of the resulting SC on the input pulse duration and wavelength is also investigated in [6, 106]. A map that shows the

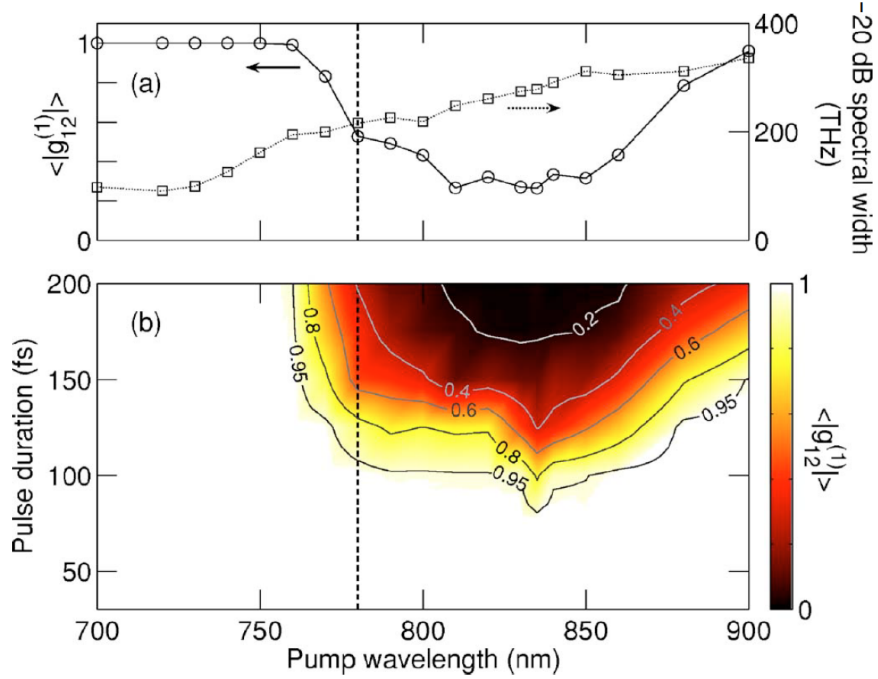


Figure 3.8: Dependence of average SC coherence and -20 dB spectral bandwidth on pump wavelength and pulse duration for constant peak power [6]. Dashed line indicates ZDW.

dependence of average SC coherence and spectral bandwidth on input pulse duration and wavelength for constant peak power was generated (Fig. 3.8). From this map, it can be seen that perfect coherence can be obtained with pulse durations of < 80 fs using any pump wavelength. Another conclusion that can be drawn is that perfect coherence can be obtained with a pump wavelength in the normal GVD regime using any pulse duration, at the expense of narrower spectral bandwidth. A somewhat surprising result is that when the process is pumped in the deep anomalous regime, obtained coherence increases. This effect can be understood by considering the characteristic lengths of modulation instability gain and soliton fission. The characteristic length for modulation instability gain is proportional to the nonlinear length and does not change considerably with wavelength. On the other hand, soliton fission length gets shorter as the dispersion coefficient gets larger and more solitons can be ejected before the modulation instability gain significantly amplifies the input pulse noise.

Chapter 4

Net-Zero Dispersion Short Pulsed Laser

Coherence of a produced supercontinuum is an important concern for applications that requires the carrier-envelope offset frequency (f_{ceo}) to be stabilized. As mentioned in chapter 3, to obtain good coherence, short pulses should be used. Another concern is the width of the f_{ceo} beat signal. Width of the beat signal depends on net laser cavity dispersion and reaches its minimum value for net-zero cavity dispersion [107]. Therefore, an ideal laser for f_{ceo} stabilization should have net-zero cavity dispersion and produce very short pulses. Current laser designs were unable to provide both features together. Similariton lasers can be compressed to very short pulse durations but they have net-normal cavity dispersion. Dispersion-managed lasers with net-zero dispersion cannot be compressed to short pulse durations (<50 fs). The good features of the both lasers should be combined to build “the ideal laser” for f_{ceo} stabilization. To be able to do this, one needs to understand the dynamics of both of these lasers.

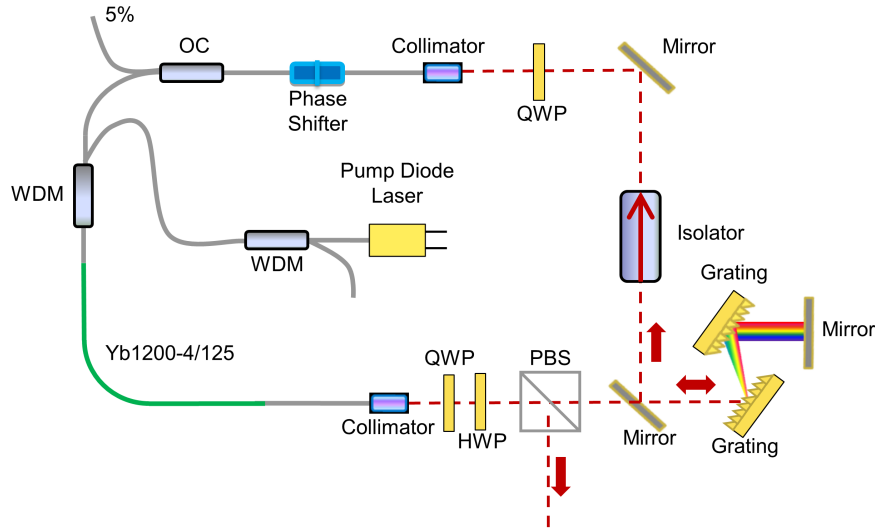


Figure 4.1: Schematics of a dispersion-managed laser.

4.1 Basic Principles of Similariton Lasers

Similariton lasers are dispersion-managed lasers with net-positive cavity dispersion. Diffraction grating separation is adjusted such that anomalous dispersion that is caused by grating pair is smaller than the total normal dispersion that is caused by other elements in the cavity (mainly fibers). Similariton lasers utilize self-similar propagation in optical fibers to reach high-energies and linearly-chirped wide spectra. Self-similar propagation occurs in fibers with normal group velocity dispersion in the presence of Kerr nonlinearity. A generic cavity design for a dispersion-managed laser is shown in Fig. 4.1. A similariton laser can exhibit two fundamentally different pulse evolutions for same cavity dispersion and pulse energy, depending on the saturable absorber parameters. In one case, pulses enter the fiber with minimal duration and minimal spectral width after the diffraction gratings. Pulses get wider in both time and frequency domains as they evolve self-similarly in the passive fiber. Pulses get amplified in the gain segment. Their spectral widths can be narrowed due to limited gain bandwidth. Saturable absorber makes the pulses shorter in time domain and narrower in frequency domain. For this type of evolution, simulated evolution of pulses for one cavity round-trip is shown in Fig. 4.2. In the second case, pulses enter the cavity with

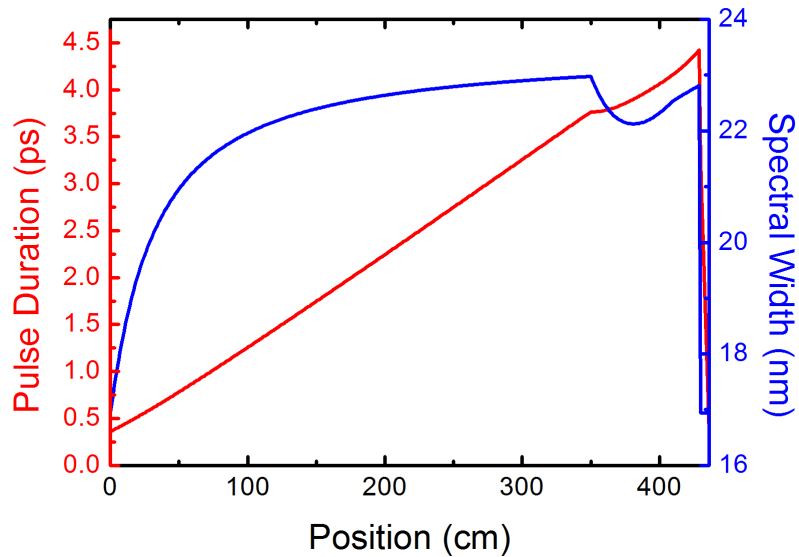


Figure 4.2: Simulated evolution of pulses in a similariton laser for the first type of evolution.

negative-chirp after the diffraction gratings. Spectral compression takes place and makes the pulses shorter in time domain and narrower in frequency domain, until the chirp on the pulse reaches zero. After that point, self-similar propagation takes place, mainly in the gain fiber. Again, saturable absorber makes the pulses shorter in time domain and narrower in frequency domain. Simulated evolution of pulses for this type of evolution is also shown for one cavity round-trip in Fig. 4.3. In both simulations, cavity consists of a segment of 350 cm-long passive fiber, followed by a segment of 60 cm-long gain fiber and another segment of passive fiber which has the length of 20 cm. These fiber segments are followed by a saturable absorber and a pair of diffraction gratings. Net cavity dispersion is $+11600 \text{ fs}^2$. Maximum pulse energy is 4.74 nJ for the first case and 4.22 nJ for the second case. Maximum peak powers are 926 W and 2612 W respectively. In conclusion, net-normal dispersion of the cavity causes pulses to have longer durations in average and allows high-energy operation without pulse breaking. Its drawbacks are also caused by net-normal cavity dispersion. Since total cavity dispersion is not zero, cavity round-trip time for every frequency component is slightly different, which causes the repetition frequency beat signal to be widened, which in turn causes f_{ceo} beat signal to be widened.

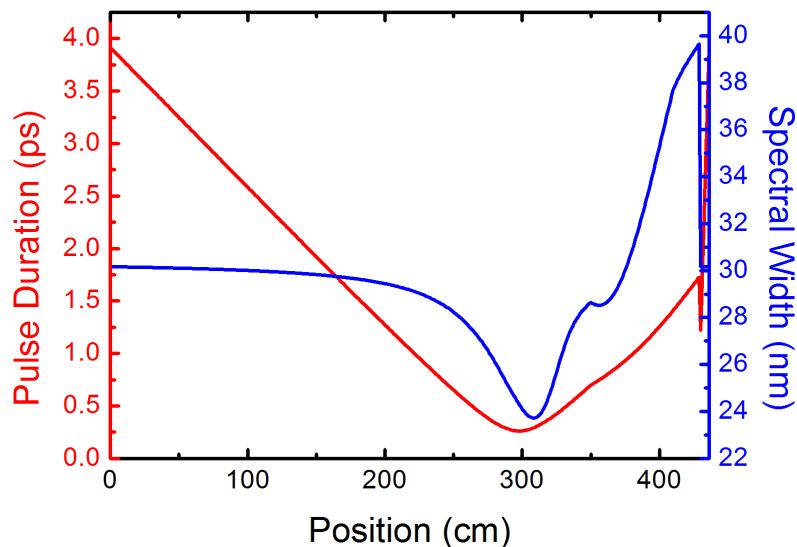


Figure 4.3: Simulated evolution of pulses in a similariton laser for the second type of evolution.

4.2 Basic Principles of Dispersion-Managed Lasers with Net-Zero Cavity Dispersion

Dispersion-managed lasers with net-zero cavity dispersion has a similar structure to the similariton lasers. Only difference is that anomalous dispersion of grating pair exactly cancels the normal dispersion of other elements in the cavity. Simulated evolution of the pulse for one round-trip is shown in Fig. 4.4. In the simulation, cavity design is very similar to the previous case, with the exceptions of 30 cm-long gain segment and diffraction grating pair separation. Maximum pulse energy is 0.56 nJ and maximum peak power is 1895 W. Pulse evolution is similar to the second type of evolution that is explained in the previous section. Main difference is that spectral compression phase continues deep into the gain fiber segment, until the 20th cm of the 30 cm-long gain fiber. Its main drawback is that net-zero cavity dispersion limits maximum reachable pulse energy to small values and pulses usually have narrower spectra than similariton laser pulses. A second simulation for the same laser with 1 nJ pulse energy is also shown in Fig. 4.5. Maximum peak power for this case is 3156 W. Notice that the position of

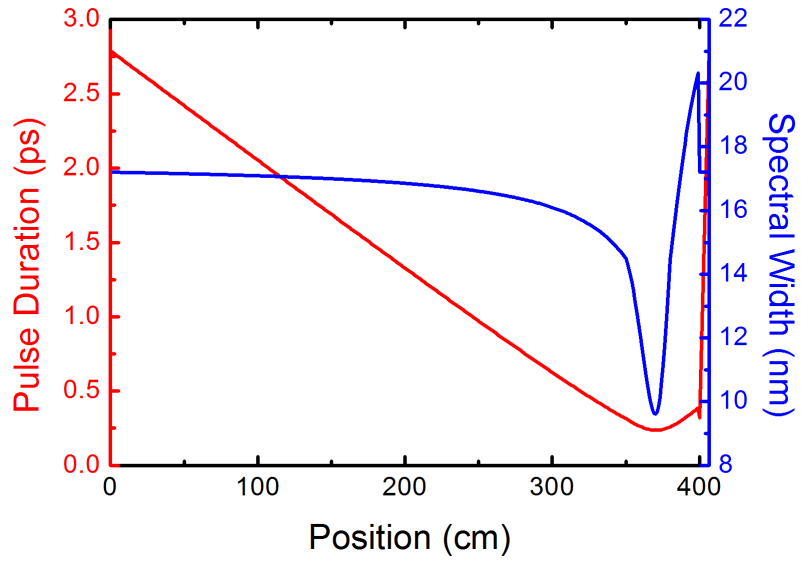


Figure 4.4: Simulated evolution of pulses in a dispersion-managed laser with net-zero cavity dispersion for 0.56 nJ pulse energy.

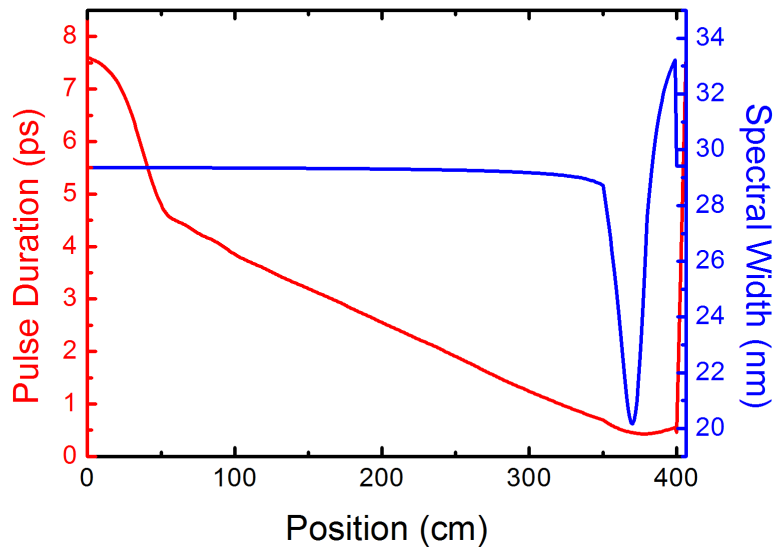


Figure 4.5: Simulated evolution of pulses in a dispersion-managed laser with net-zero cavity dispersion for 1 nJ pulse energy.

minimal spectral width point did not change. The reason for low pulse energy limitation can be understood from these simulations in the following way: as the pulse energy increases, spectral bandwidth of the pulses increases and spectral compression dominantly happens in the gain segment. After some energy value, spectral compression cannot balance the increase in spectral bandwidth.

4.3 Design and Characterization of a Novel Laser

As it was stated before, “the ideal laser” for f_{ceo} stabilization should have net-zero cavity dispersion and its pulses should be compressible to short (<50 fs) durations. To satisfy the short pulse duration requirement, pulses with large spectral bandwidths are required. To obtain large spectral bandwidth, the net-zero dispersion laser should be modified in such a way that spectral compression should end at the beginning of the gain fiber. Since the spectral compression in the passive fiber before the gain fiber would not be enough, another component is necessary to keep the balance. A spectral bandpass filter, which is placed before the passive fiber can do the job. If the input energy to the passive fiber is reduced using a beamsplitter to reduce the effect of spectral compression, balance can be satisfied even with increased pulse energy. Such a laser design is shown in Fig. 4.6. With these thoughts in mind, I simulated a zero-dispersion laser with a 10 nm-wide bandpass filter and a 60/40 beamsplitter. Laser has the same fiber lengths and structure as the simulations in the previous section. Simulated pulse evolution and spectrum are shown in Fig. 4.7-4.8. In the given simulation, pulses enter the fiber with pulse energy of 57 pJ and reach intra-cavity pulse energy of 3.82 nJ and peak power of 6296 W at the end of gain fiber. Pulses reach minimal spectral bandwidth of 6.0 nm at 9th cm of the gain fiber and maximal spectral bandwidth of 61.7 nm at the end of fiber section. Beamsplitter output of the laser can be compressed to 38 fs using a diffraction grating pair with line density of 600 lines/mm and the compressed pulse shape is shown in Fig. 4.9.

Encouraged by the simulation results, a net-zero cavity dispersion laser is

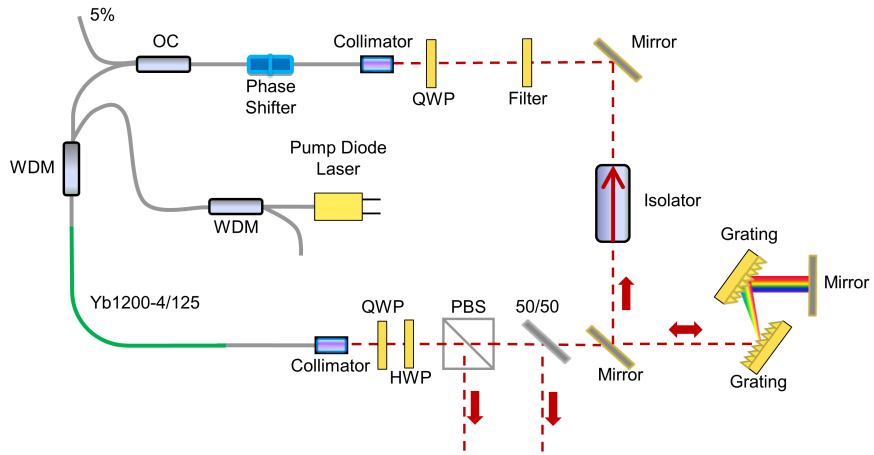


Figure 4.6: Schematics of the new laser.

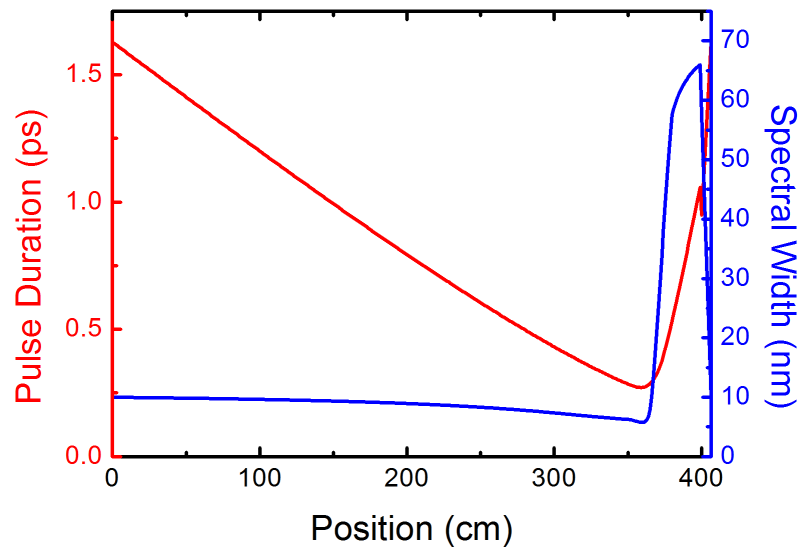


Figure 4.7: Simulated evolution of pulses in the new laser.

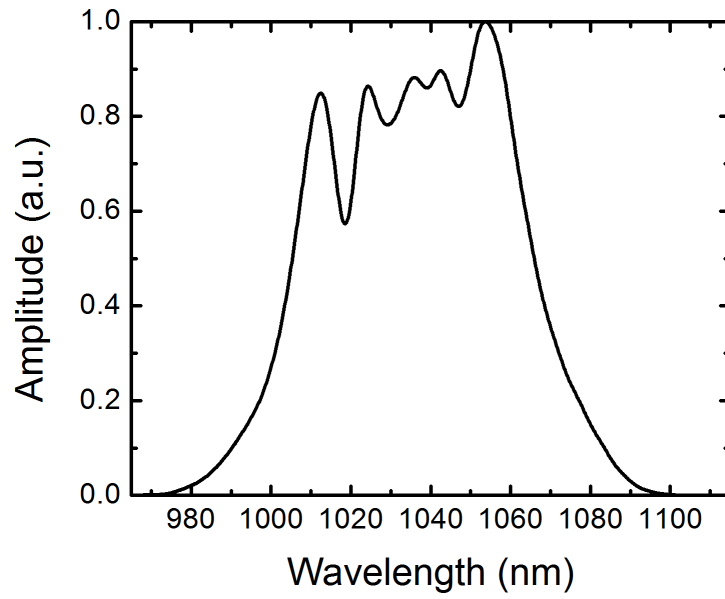


Figure 4.8: Simulated beamsplitter output of the laser for 3.82 nJ pulse energy.

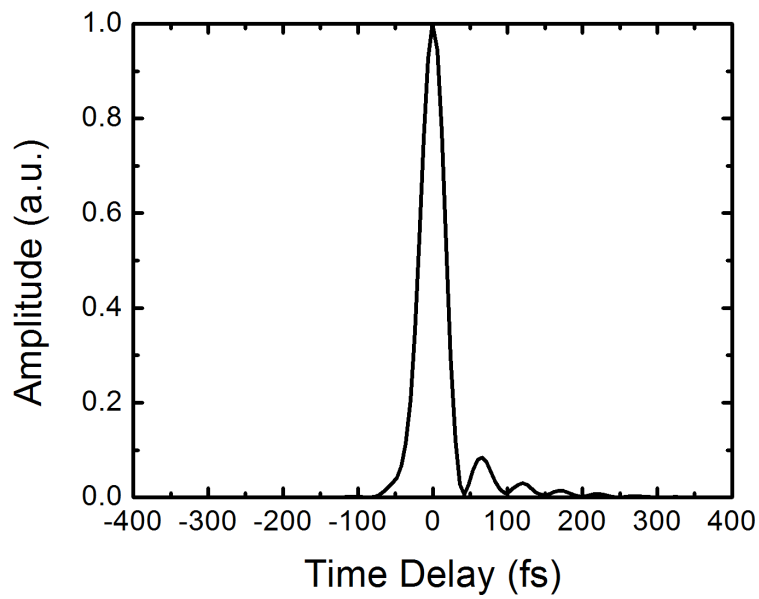


Figure 4.9: Simulated compressed beamsplitter output.

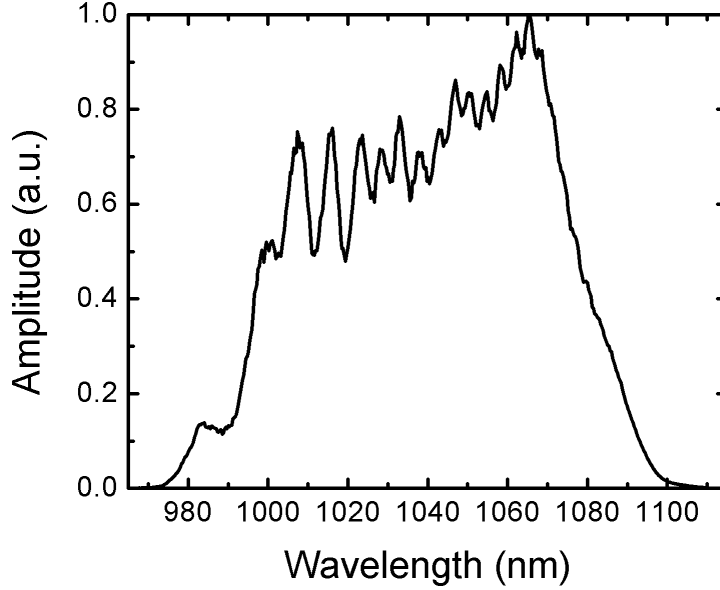


Figure 4.10: 50/50 Beamsplitter output of the laser.

built with the simulated parameters. Grating distance is initially set such that the total cavity dispersion is near-zero. After that, cavity dispersion is fine-tuned to zero by using the *in situ* dispersion measurement technique proposed by Knox [108]. 50/50 beamsplitter is placed after the PBS. Transmittance of the 50/50 beamsplitter is 50% for unpolarized light and $\sim 60\%$ for the polarized light after the PBS. Measured spectra for polarizing beamsplitter (PBS) and 50/50 beamsplitter outputs are shown in Fig. 4.10-4.11. Repetition rate of the laser is 49.5 MHz. PBS output power is 90.4 mW and 50/50 beamsplitter output power is 38.6 mW. This means the total intra-cavity power is 186.9 mW and pulse energy is 3.81 nJ. Output of the 50/50 beamsplitter is compressed using a pair of diffraction gratings with line density of 600 lines/mm and measured using an intensity autocorrelator. Measured autocorrelation and spectrum is given to PICASO algorithm and pulse shape is retrieved [109]. Measured autocorrelation trace, PICASO retrieved autocorrelation trace and PICASO retrieved pulse shape is shown in Fig. 4.12. Retrieved pulse shape from the PICASO algorithm has a FWHM width of 33 fs.

Noise performance of the laser is characterized by relative intensity noise

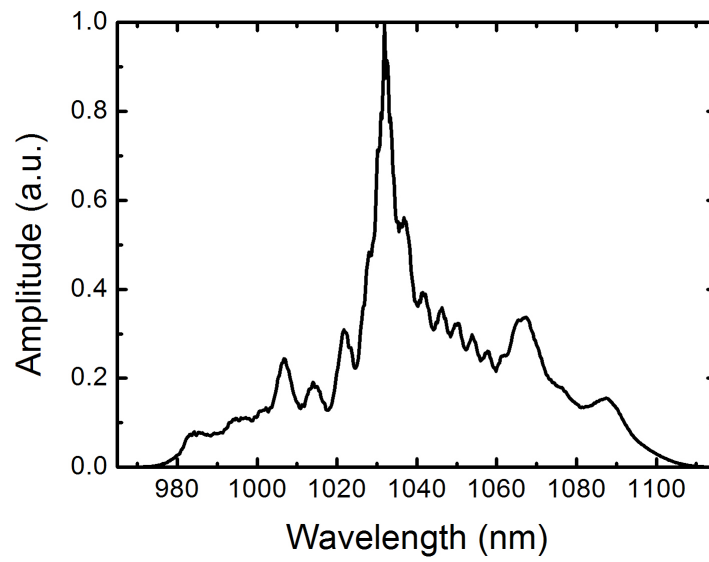


Figure 4.11: Polarizing beamsplitter output of the laser.

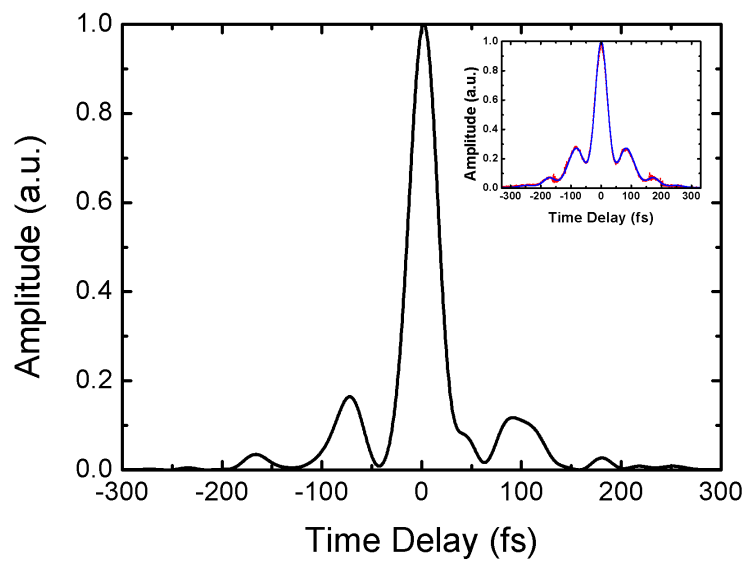


Figure 4.12: Retrieved pulse shape from PICASO algorithm. (Inset) Measured (red) and PICASO retrieved (blue) autocorrelation traces.

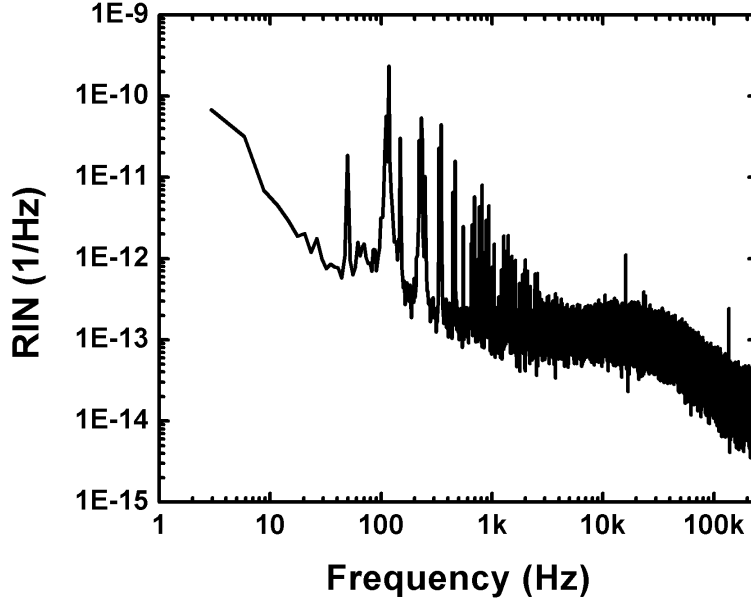


Figure 4.13: Relative intensity noise of the laser.

(RIN) and phase noise (PN) measurements. Noise measurements are performed using the PBS output of the laser. For the measurement of RIN, output of the laser is passed through a variable attenuator and detected by a 100 MHz photodetector. Output of the photodetector is filtered by a low-pass filter with -3 dB cut-off frequency of 1.9 MHz and analyzed by a Rohde&Schwarz UPV Audio Analyzer. The measured RIN for 3 Hz - 250 kHz interval is shown in Fig. 4.13. Integrated RIN for this interval is equal to 0.017%. From the location of the peaks in the RIN graph, it can be concluded that most of the intensity noise is caused by electrical and acoustic noise from the environment.

Measurement of the phase noise is done in a similar way. Output of the free-running laser is passed through a variable attenuator and detected by an EOT-ET3500 photodetector which has a bandwidth >15 GHz. 16th harmonic of the repetition rate is passed through a bandpass filter and then amplified by a Mini-Circuits ZRL-1150LN+ low-noise amplifier. Amplified signal is analyzed using Agilent E5052B signal source analyzer. Measured phase noise heavily depends on the incident optical power and photodiode bias voltage. Since all the RF

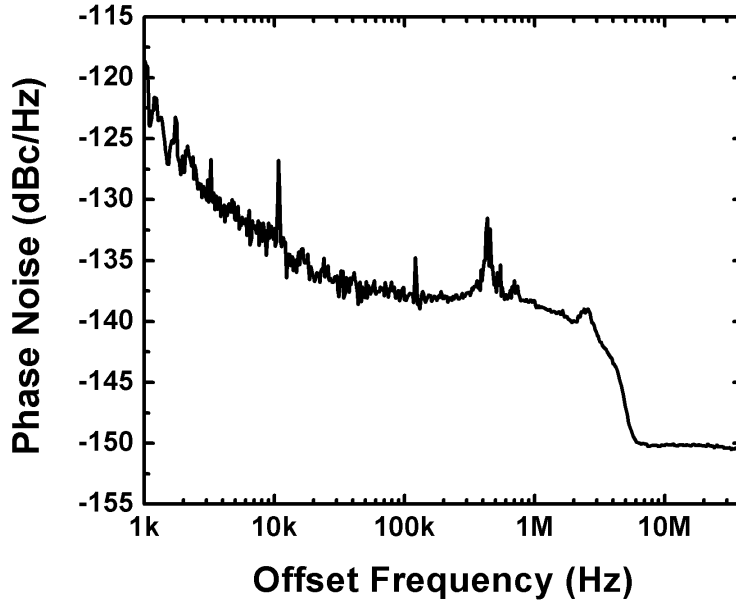


Figure 4.14: Phase noise of the laser.

components also contribute to the noise, measured PN should be considered as an upper-bound to the actual phase noise of the laser. The measured PN is shown in Fig. 4.14. Timing jitter that is calculated using this measurement is 76 fs. For the actual measurement of the PN, optical measurement techniques should be used [110]. Typical timing jitter values measured for near-zero dispersion Yb-doped fiber lasers using optical techniques are <1 fs [111].

Chapter 5

Frequency Comb Stabilization and Absolute Frequency Measurements with The Stabilized Frequency Comb

In this chapter, stabilized femtosecond frequency comb that has been developed will be explained in detail.

5.1 Repetition-Rate Stabilization of the Laser

Laser is slightly modified and 50/50 beamsplitter is placed after the bandpass filter. Schematics of the repetition rate stabilization and measurement setup is shown in Fig. 5.1. 5% Output of the laser is detected by a photodiode. Output of the photodiode is passed through a low-pass filter which lets only the fundamental repetition frequency to pass. The signal is amplified by an amplifier and splitted into two. One arm of the splitted signal is connected to a frequency counter for measurement purposes and the other arm is connected to an electronic mixer. A signal generator, which is referenced to Cs atomic clock 1 is also connected

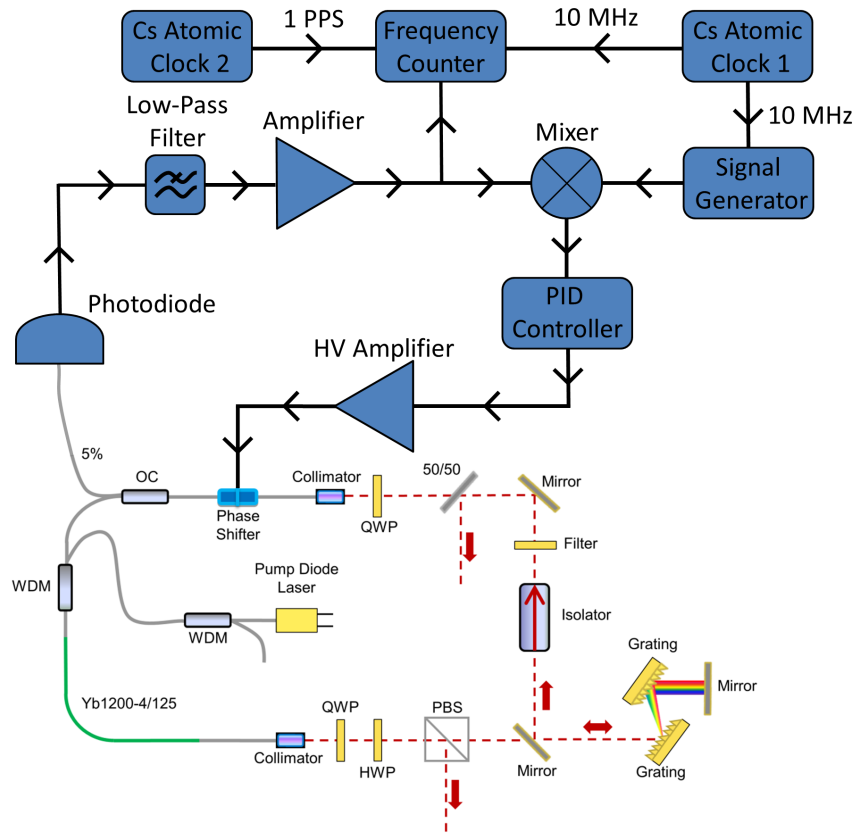


Figure 5.1: Schematics of the repetition-rate locking and characterization setup.

to the mixer. Output frequency of the signal generator is adjusted to a value that is close to the repetition frequency of the laser. At the output of the mixer, difference frequency between the signal generator and the repetition-rate of the laser is obtained and connected to a PID controller. Output of the PID controller is amplified by a high-voltage amplifier and connected to the fiber phase shifter in the laser cavity. Proportional gain, integrator gain offset voltage, lower and upper output voltage limits of the PID controller are adjusted such that output of the high-voltage amplifier never exceeds the limits of the fiber phase shifter and a good repetition-rate locking is achieved.

Performance of the repetition-rate stabilization system is shown by performing time-interval measurements with the frequency counter and calculating the corresponding overlapping Allan deviations [112]. Frequency counter is also referenced to Cs atomic clock 1. 1 pulse-per-second (PPS) output of Cs atomic clock 2 is connected to frequency counter as trigger signal. Signal generator frequency is adjusted to be an integer, therefore for an ideal stabilization system with ideal reference oscillators, phase of the repetition-rate signal will be the same for every triggered measurement. Instabilities of the system is then quantified by the fluctuation of the phase of the repetition-rate signal from measurement to measurement. Overlapping Allan deviation graphs are shown in Fig. 5.2.

5.2 Carrier-Envelope-Offset Frequency Stabilization

Carrier-envelope-offset frequency (f_{ceo}) of the laser is obtained with the setup shown in Fig. 5.3. Output from the 50/50 beamsplitter that is inside the laser is passed through a half-wave plate and coupled into the 250 cm-long HI-1060 fiber by a pigtailed fiber collimator. This fiber is followed by a 980/1030 nm wavelength-division-multiplexer (WDM) to couple the pump laser into the 40-cm long Yb1200-4/125 gain fiber. Total fiber length before the gain fiber is 350 cm as it was in the laser cavity. It is designed in this way for the spectral compression of the pulses to end at the beginning of the gain fiber. Gain fiber is 10 cm

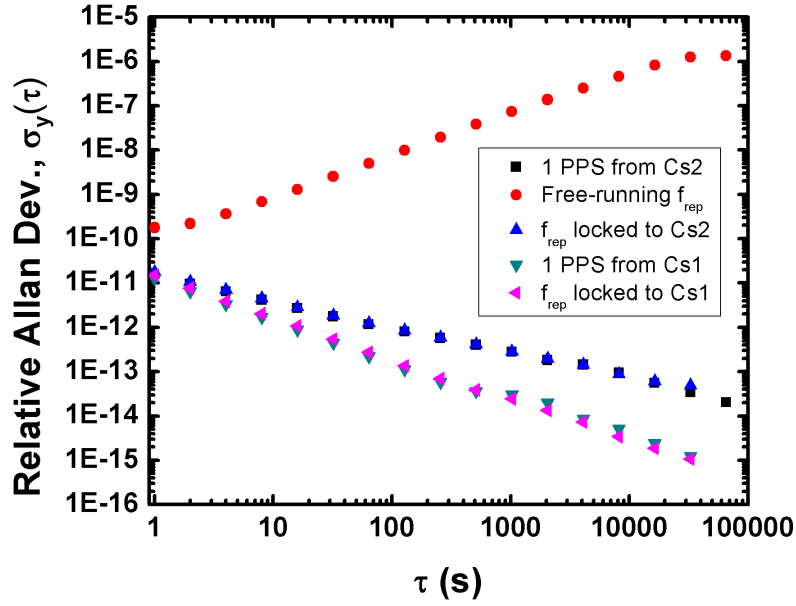


Figure 5.2: Relative Allan deviation vs. averaging time graph for the given cases.

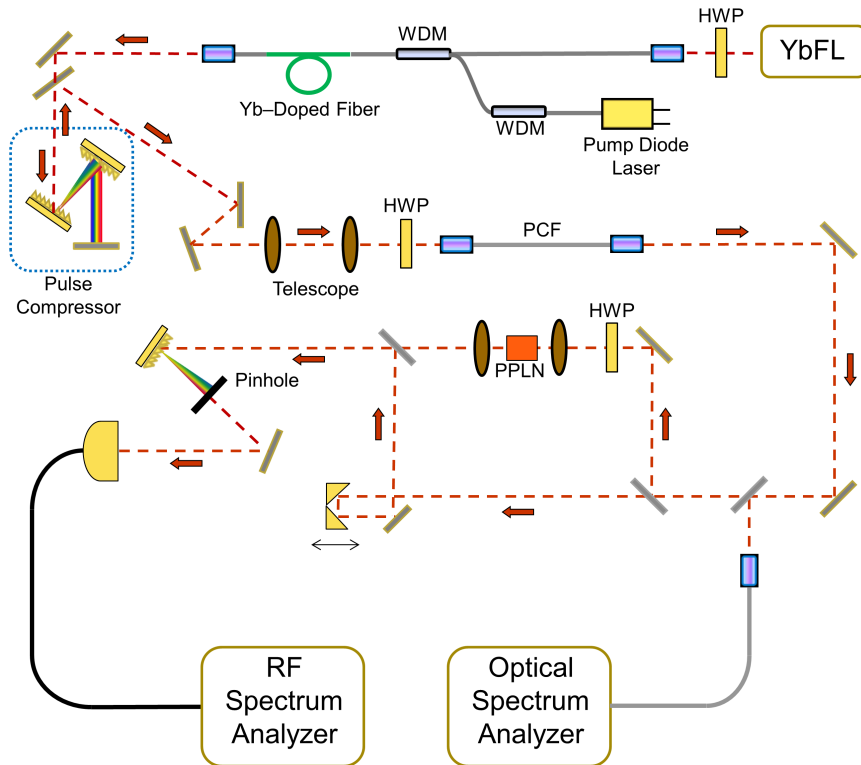


Figure 5.3: Schematics of the supercontinuum generation setup and f-2f interferometer.

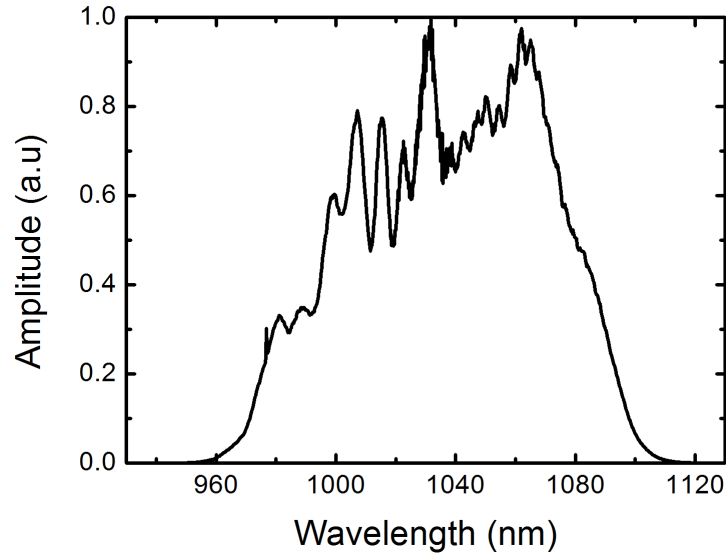


Figure 5.4: Output spectrum of the amplifier.

longer than it was in the laser cavity so the amplifier can be pumped with higher pump powers than the laser itself. Collimator that is placed after the gain fiber has the length of 18 cm. Output power of 335 mW is obtained for 650 mW of pump power. Output spectrum of the amplifier for this case is shown in Fig. 5.4. Output of the amplifier is compressed by a pair of diffraction gratings with the line density of 300 lines/mm. Compressed pulse duration is measured by an intensity autocorrelator. Measured autocorrelation trace and measured amplifier spectrum is processed using PICASO algorithm to retrieve the pulse shape and the retrieved pulse shape has FWHM of 36 fs. Measured autocorrelation trace and the retrieved pulse shape is shown in Fig. 5.5. Pulse compressor work with 63% efficiency. Compressed pulses are coupled into 30 cm-long SC-3.7-975 photonic crystal fiber after passing through a half-wave plate for polarization adjustment. Generated supercontinuum is detected by an optical spectrum analyzer. Obtained supercontinuum spectrum for 62 mW coupled average power is shown (Fig. 5.6). Output of PCF is separated into two beams with a dichroic mirror with cut-off wavelength of 1000 nm. The beam with higher wavelength is focused to a 1 cm-long PPLN crystal which efficiently produces second harmonic of 1400 nm. Generated second harmonic is collimated using a second lens. The beam with the

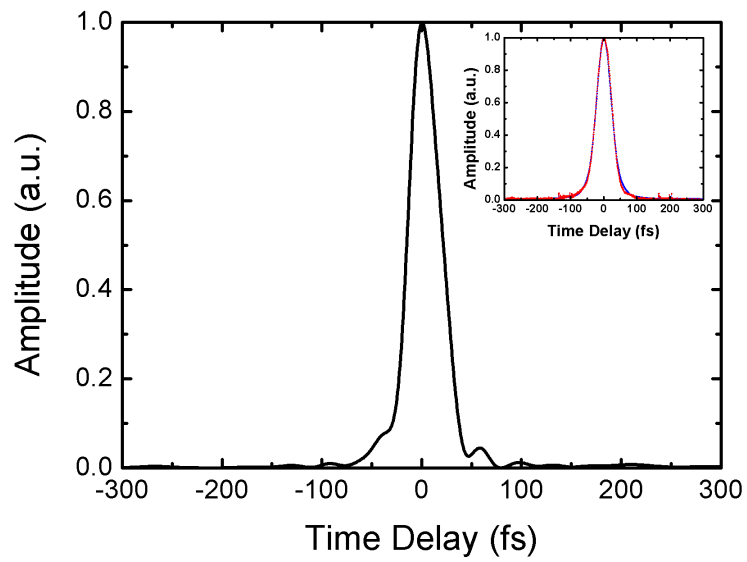


Figure 5.5: Compressed pulse shape that is retrieved from PICASO algorithm. (Inset) Measured (red) and PICASO retrieved (blue) autocorrelation traces.

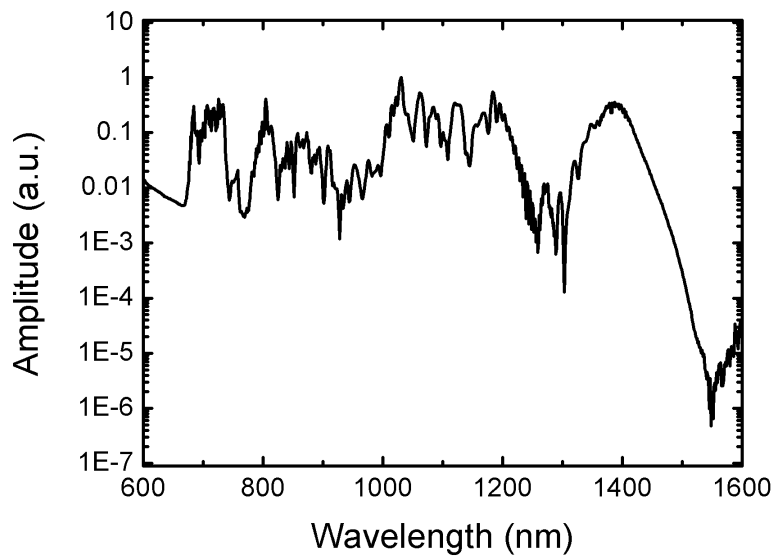


Figure 5.6: Measured supercontinuum spectrum for 62 mW of coupled average power.

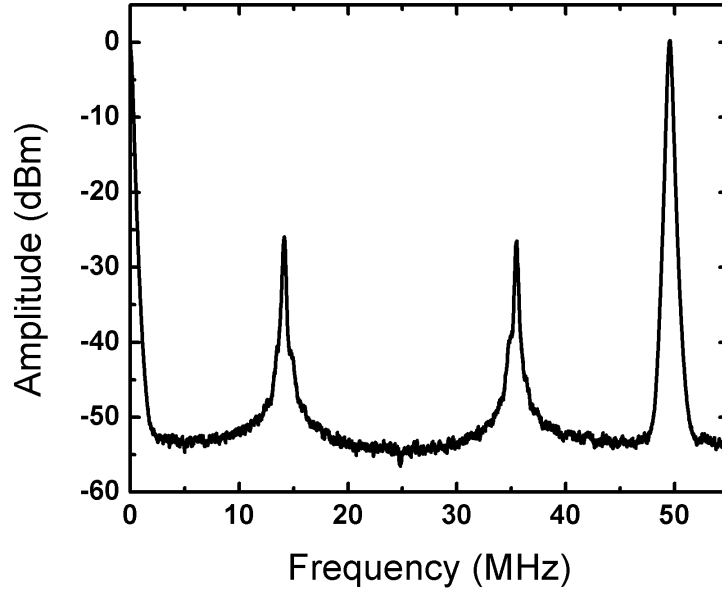


Figure 5.7: Obtained carrier-envelope offset beat signal.

lower wavelength is sent to an adjustable delay line. Two beams are combined again by a 50/50 beamsplitter. Combined beam is sent to a diffraction grating and the spectral region which includes the SHG signal is separated by a pinhole and detected by an amplified photodiode. Obtained carrier-envelope offset beat signal is shown in Fig. 5.7.

Carrier-envelope offset frequency of the laser is stabilized using the setup shown in Fig. 5.8. Obtained signal is passed through a 30 MHz band-pass filter with -3 dB width of 8 MHz. If offset beat does not correspond to this region, it is shifted to 30 MHz by slightly changing the laser pump diode current. Filtered signal is amplified and splitted into two. One line is connected to a frequency counter for measurement purposes and the other line is connected to a phase detector. A 30 MHz sine signal that is coming from a function generator is also connected to the phase detector. The error signal that is obtained from the phase detector is connected to a PID controller and PID controller's output is connected to the analog modulation input of the laser pump diode's current driver.

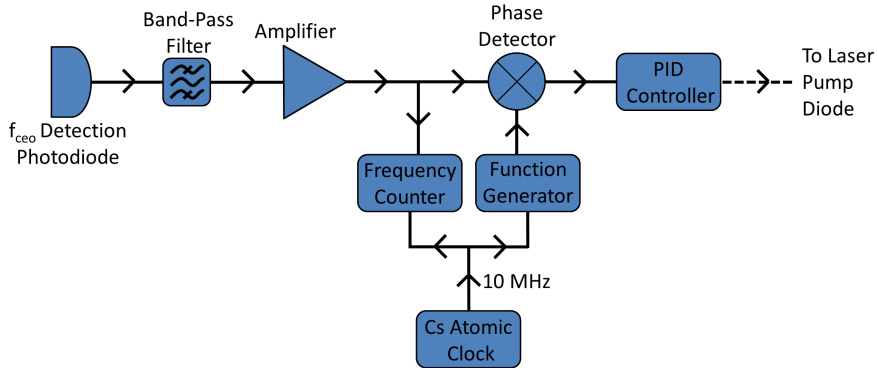


Figure 5.8: Schematics of the carrier-envelope offset frequency locking setup.

Stability of the carrier-envelope offset frequency is characterized by performing frequency measurements with the frequency counter and calculating the corresponding Allan deviations. Overlapping Allan deviations for free-running and stabilized cases are shown in Fig. 5.9.

5.3 Absolute Frequency Measurements with the Stabilized Frequency Comb

Absolute frequency measurements are performed by obtaining the frequency difference between the laser-under-test (LUT) and one of the comb teeth. Schematics of the heterodyne beat setup is shown in Fig. 5.10. After the stabilization of the laser, generated supercontinuum and the beam from LUT are passed through separate half-wave plates and combined by a beamsplitter. Combined beam is spread spectrally by a diffraction grating and the spectral region of interest is selected by a pinhole. Half-wave plate angles and beam power are adjusted for optimum beat signal-to-noise ratio. Obtained RF beat signal is filtered using a band-pass filter, amplified and connected to a frequency counter that is referenced to a Cs atomic clock. Measured beat frequency is recorded for some time and Allan variance statistics is used to characterize the stability of LUT.

Generally, measuring the beat signal frequency is not enough for determining the absolute frequency of LUT. As it is shown in Fig. 5.11, two LUT-comb beat

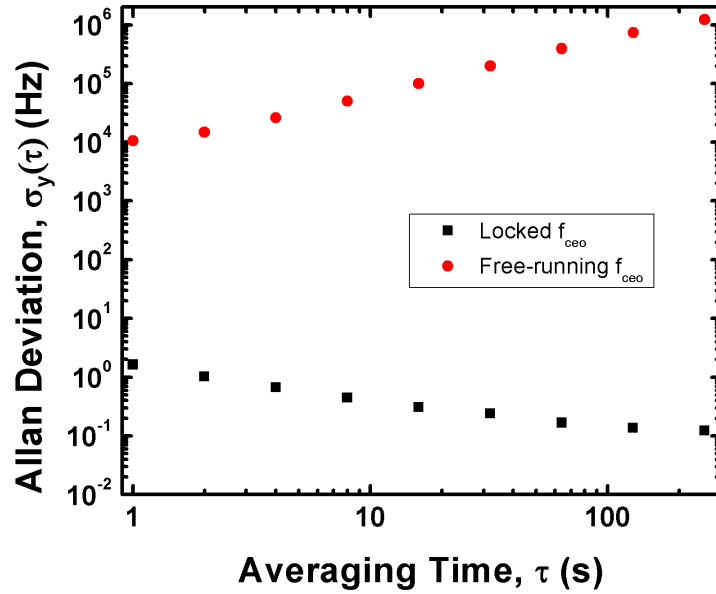


Figure 5.9: Allan deviation vs. averaging time graphs for free-running and stabilized f_{ceo} .

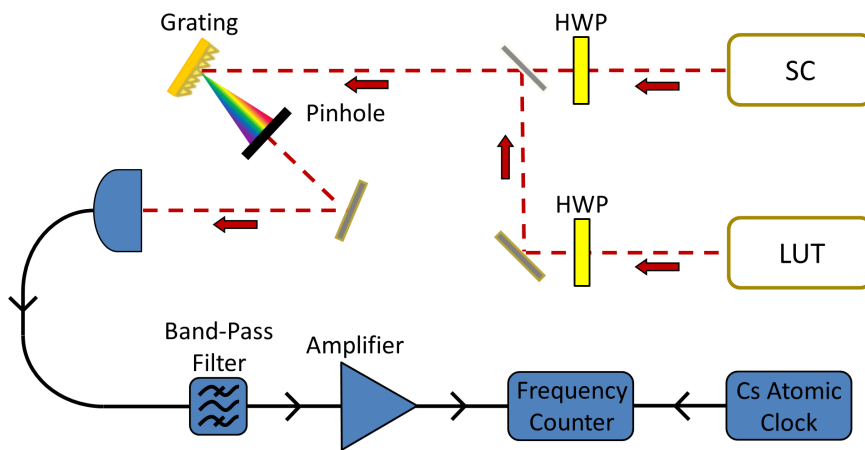


Figure 5.10: Schematics of the absolute frequency measurement setup.

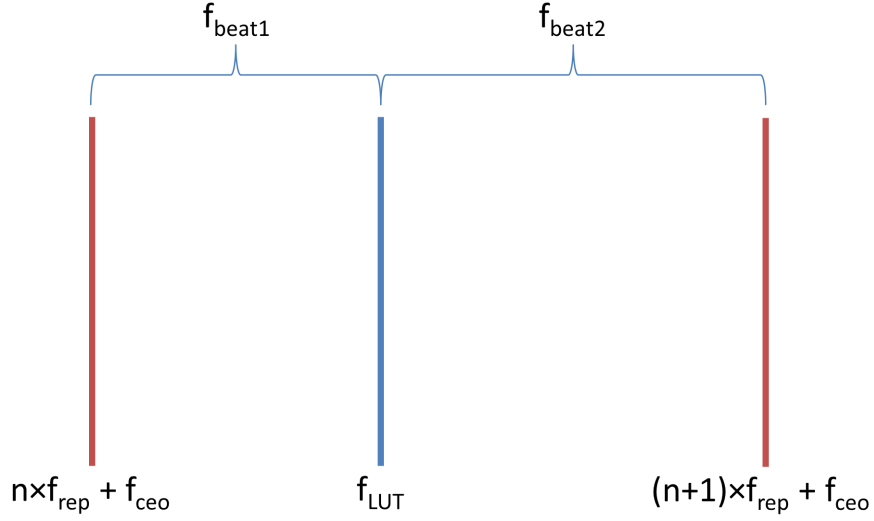


Figure 5.11: Illustration of LUT and comb teeth.

signals are observed that is smaller than the repetition rate of the comb and same is valid for f_{ceo} beat signal. It is necessary to identify the beat signals and the comb teeth number n .

Frequencies of LUT-comb beat signals is given by the following equations:

$$f_{\text{beat1}} = f_{\text{LUT}} - n f_{\text{rep}} - f_{\text{ceo}} \quad (5.1)$$

$$f_{\text{beat2}} = (n + 1) f_{\text{rep}} + f_{\text{ceo}} - f_{\text{LUT}} \quad (5.2)$$

by taking partial derivatives of equations 5.1 and 5.2, the following equations are obtained:

$$\frac{\partial f_{\text{beat1}}}{\partial f_{\text{rep}}} = -n \quad (5.3)$$

$$\frac{\partial f_{\text{beat2}}}{\partial f_{\text{rep}}} = n + 1 \quad (5.4)$$

$$\frac{\partial f_{\text{beat1}}}{\partial f_{\text{ceo}}} = -1 \quad (5.5)$$

$$\frac{\partial f_{\text{beat2}}}{\partial f_{\text{ceo}}} = 1 \quad (5.6)$$

Using these equations, beat signals can be identified and the number “ n ” can be calculated by following the steps below:

1. Lock the repetition frequency of the laser to an arbitrary frequency.

2. Lock one of the carrier-envelope offset frequency beat signals to an arbitrary frequency.
3. Observe LUT beat signals.
4. Filter and read one of the beat signals using a frequency counter. Record the beat signal for some time.
5. Slightly modify the repetition rate of the laser. Repeat the last step for the same beat signal. Number “n” can be calculated from equation 5.3 or equation 5.4, depending on the sign of the derivative.
6. Slightly modify the frequency of the locked carrier-envelope offset frequency beat signal. Observe the change of carrier-envelope offset beat signals and LUT beat signals. Carrier-envelope offset frequency can be identified using equations 5.5 and 5.6.

If the LUT frequency is known approximately (as it is the case for the lasers that are stabilized to a known atomic transition), it is usually enough to measure one of the LUT beat signals, without identifying the beat signals, to determine the absolute frequency of the laser after locking the repetition-rate and any one of the carrier-envelope offset beat signals. When the beat frequencies are not determined, there are four different possibilities for the absolute frequency of the laser and the closest one to the known transition frequency can be assumed to be the absolute frequency of the laser.

Using the method explained in the previous paragraph, absolute frequency measurement of a Nd:YAG laser that is stabilized to the a_{10} line of R(56)32-0 group is performed. Stabilization is achieved by using the 532 nm second-harmonic output of the laser and the measurement is performed by using the 1064 nm output of the laser. Nd:YAG laser parameters, PLL parameters and iodine cell temperature is adjusted to their respective CIPM (International Committee for Weights and Measures) recommended values. Beat signal between the frequency comb teeth and the Nd:YAG laser is obtained using the setup shown in Fig. 5.10. Repetition rate of the Yb-laser is locked to 49556406.90 Hz. One of the carrier-envelope offset beat signals is locked to 30 MHz. One of the obtained beat

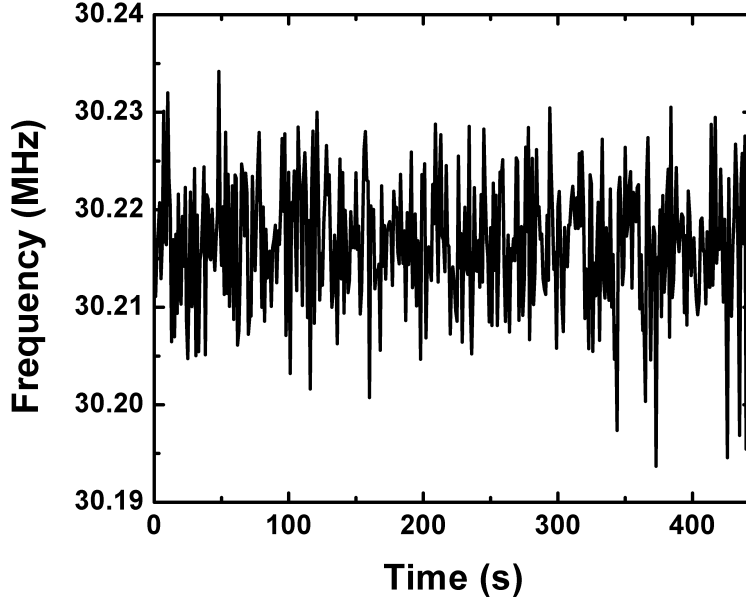


Figure 5.12: Nd:YAG beat frequency measurement data.

signals is passed through a 30 MHz bandpass filter with -3 dB bandwidth of 10 MHz and read by a frequency counter that is stabilized to a Cs atomic clock. Beat frequency is read once a second and recorded. Measurement data is shown in Fig. 5.12. Average of the data is 30216604 Hz. Overlapping Allan deviation graph for the measurement data is shown in Fig. 5.13.

Since the beat signals are not identified, all possible frequencies should be considered. The frequency of R(56)32-0: a_{10} is given as 563260223513 ± 5 kHz by CIPM. Since the frequency of 1064 nm beam should be around half of this value, the frequency of the laser should be around 28163011756500 Hz. There are four possible combinations of beat signals and four possible frequency values as it was mentioned before:

1. Locked carrier-offset frequency beat signal is f_{ceo} and the recorded comb-LUT beat frequency is the beat of LUT with a comb teeth with lower frequency than the LUT. In this case, the possible actual laser frequency that is closest to the recommended value is 28163011757442 Hz, which is 942 Hz above the recommended value.

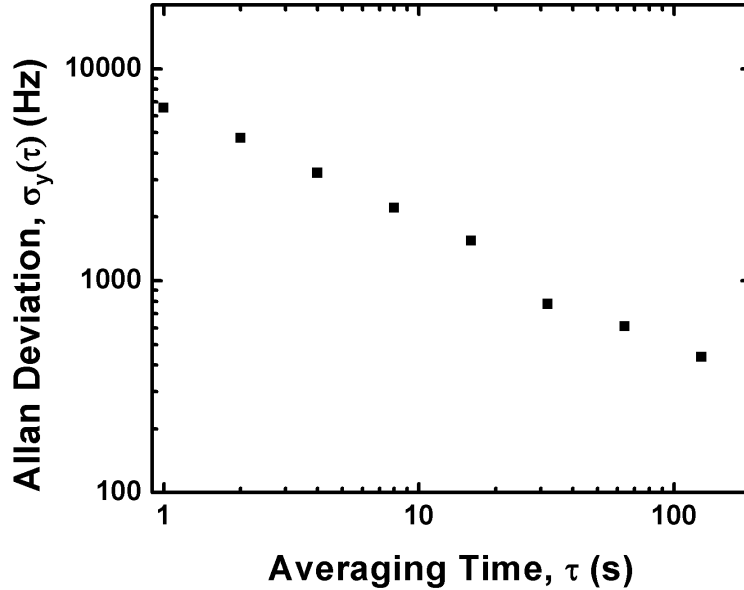


Figure 5.13: Overlapping Allan deviation graph for beat signal between the stabilized Nd:YAG laser and one frequency comb tooth.

2. Locked carrier-offset frequency beat signal is f_{ceo} and the recorded comb-LUT beat frequency is the beat of LUT with a comb teeth with higher frequency than the LUT. In this case, the possible actual laser frequency that is closest to the recommended value is 281630100880641 Hz, which is 10855859 Hz below the recommended value.
3. Locked carrier-offset frequency beat signal is $f_{\text{rep}} - f_{\text{ceo}}$ and the recorded comb-LUT beat frequency is the beat of LUT with a comb teeth with lower frequency than the LUT. In this case, the possible actual laser frequency that is closest to the recommended value is 281630101313849 Hz, which is 10422651 Hz below the recommended value.
4. Locked carrier-offset frequency beat signal is $f_{\text{rep}} - f_{\text{ceo}}$ and the recorded comb-LUT beat frequency is the beat of LUT with a comb teeth with higher frequency than the LUT. In this case, the possible actual laser frequency that is closest to the recommended value is 281630090437048 Hz, which is 21299452 Hz below the recommended value.

It can be safely assumed that the frequency calculated for case 1 is indeed the absolute frequency of the stabilized Nd:YAG laser and the multiplicative constant for repetition rate is 5683020. Measurement uncertainty can be calculated using the Allan deviation graphs for repetition rate, carrier-envelope offset frequency and LUT beat frequency. When a line is fitted to Fig. 5.13, the slope of the line is -0.580324 and the Allan deviation for $\tau = 1$ is 6950.33. Therefore, Allan deviation of Nd:YAG beat frequency for an arbitrary τ can be calculated from the equation $\sigma_y(\tau) = 6950.33 \times \tau^{-0.580324}$. Same calculation can be repeated for repetition rate and carrier-envelope offset frequency. Allan deviation of repetition rate can be written as $\sigma_y(\tau) = 7.227 \times 10^{-4} \times \tau^{-0.564945}$ and Allan deviation of carrier-envelope offset frequency can be written as $\sigma_y(\tau) = 1.43391 \times \tau^{-0.513901}$. Therefore, for the averaging time of 445 s, the Allan deviations for f_{ceo} , $n \times f_{\text{rep}}$ and f_{beat} are 0.06 Hz, 131 Hz and 202 Hz, respectively. As a result, the absolute frequency of the 1064 nm output of Nd:YAG laser that is stabilized to R(56)32-0: a_{10} line of iodine gas is measured as 281630111757442 ± 333 Hz, which is within the frequency interval that is recommended by CIPM.

Chapter 6

Conclusions

In this thesis, a new fiber laser design and a fully stabilized Yb-doped frequency comb that is based on this design is presented. The design and understanding of the system requires the understanding of the laser dynamics and supercontinuum generation process. For this reason, numerical simulations are used and the utilized simulation methods and simulation results are presented.

In chapter 1, introductory information about optical fiber technology, pulse propagation dynamics in fibers, mode-locked fiber lasers and femtosecond frequency combs is given.

In chapter 2, numerical simulations for ultrashort pulse propagation in fibers are presented. Several computational schemes are compared and split-step Fourier and fourth-order Runge-Kutta in the interaction picture methods are discussed in some detail. Local error and conservation quantity error methods for adaptive step-size control are discussed. At the end of the chapter, some improvements over the generalized nonlinear Schrödinger equation are presented.

In chapter 3, dynamics of supercontinuum generation in photonic crystal fibers using femtosecond pulses are explained with the help of numerical simulations. In addition, dependence of the generated supercontinuum parameters on the input pulse parameters are also investigated.

In chapter 4, a novel laser which has net-zero cavity dispersion and produces output pulses that can be compressed to 33 fs is presented. The laser is characterized by spectrum, autocorrelation, relative intensity noise and phase noise measurements.

In chapter 5, the stabilized femtosecond frequency comb that has been built using the laser presented on the previous chapter and absolute frequency measurement of an Nd:YAG/I₂ laser performed with this comb are presented. Repetition-rate and carrier-envelope-offset frequency stabilization setups are explained in detail and their characterizations of long-term stability are presented using overlapping Allan deviations.

In the appendices, two numerical simulation programs, that is written in MATLAB and solves generalized Schrödinger equation are given. The first program uses fixed step-sizes through the propagation while the second program uses conservation quantity error method for adaptive step-size control.

Bibliography

- [1] Mrzeon, “Optical fiber types.svg — Wikimedia Commons.” http://commons.wikimedia.org/wiki/File:Optical_fiber_types.svg, 2007. [Online; accessed 16-January-2013].
- [2] G. P. Agrawal, *Nonlinear Fiber Optics*. San Diego, CA, USA: Elsevier Inc., 2007.
- [3] J. Hult, “A fourth-order Runge-Kutta in the interaction picture method for simulating supercontinuum generation in optical fibers,” *IEEE Journal of Lightwave Technology*, vol. 25, no. 12, pp. 3770–3775, 2007.
- [4] D. Hollenbeck and C. D. Cantrell, “Multiple-vibrational-mode model for fiber-optic Raman gain spectrum and response function,” *Journal of Optical Society of America B*, vol. 19, no. 12, pp. 2886–2892, 2002.
- [5] A. M. Heidt, “Efficient adaptive step size method for the simulation of supercontinuum generation in optical fibers,” *IEEE Journal of Lightwave Technology*, vol. 27, no. 18, pp. 3984–3991, 2009.
- [6] J. M. Dudley, G. Genty, and S. Coen, “Supercontinuum generation in photonic crystal fiber,” *Reviews of Modern Physics*, vol. 78, no. 4, pp. 1135–1184, 2006.
- [7] D. Colladon, “On the reflections of a ray of light inside a parabolic liquid stream,” *Comptes Rendus*, no. 15, pp. 800–802, 1842.
- [8] J. Babinet, “Note on the transmission of light by sinuous canals,” *Comptes Rendus*, no. 15, p. 802, 1842.

- [9] J. L. Baird, "An improved method of and means for producing optical images," British Patent 285,738, 1928.
- [10] C. W. Hansell, "Picture transmission," US Patent 1,751,584, 1930.
- [11] H. Lamm, "Biegsame optische gerte," *Z. Instrumentenk*, no. 50, pp. 579–581, 1930.
- [12] H. Hopkins and N. S. Kapany, "A flexible fiberscope, using static scanning," *Nature*, vol. 22, no. 173, pp. 39–41, 1954.
- [13] L. E. Curtiss, "Glass fiber optical devices," US Patent 3,589,793, 1971.
- [14] J. Nishizawa and K. Suto, "Terahertz wave generation and light amplification using Raman effect," in *Physics of Semiconductor Devices IWPSD-2003* (K. N. Bhat and A. DasGupta, eds.), India: Narosa Publishing House, 2004.
- [15] M. Brner, "Mehrstufiges bertragungssystem fr pulscodemodulation dargestellte nachrichten," DE Patent 1,254,513, 1967.
- [16] M. Brner, "Elecro-optical transmission system utilizing lasers," US Patent 3,845,293, 1974.
- [17] C. K. Kao and G. A. Hockham, "Dielectric-fibre surface waveguides for optical frequencies," *Proc. IEE*, vol. 113, no. 7, pp. 1151–1158, 1966.
- [18] D. B. Keck, P. C. Schultz, and F. Zimar, "Method of forming optical waveguide fibers," US Patent 3,737,292, 1973.
- [19] R. J. Mears, L. Reekie, M. Jauncey, and D. N. Payne, "Low-noise erbium-doped fiber amplifier operating at 1.54 μm ," *Electronics Letters*, vol. 23, no. 19, pp. 1026–1028, 1987.
- [20] E. Desurvire, J. R. Simpson, and P. C. Becker, "High-gain erbium-doped traveling-wave fiber amplifier," *Optics Letters*, vol. 12, no. 11, pp. 888–890, 1987.

- [21] P. Russell, "Photonic crystal fibers," *Science*, vol. 299, no. 5605, pp. 358–362, 2003.
- [22] D. Marcuse, "Loss analysis of single-mode fiber splices," *The Bell System Technical Journal*, vol. 56, no. 5, pp. 703–718, 1977.
- [23] D. Milam, "Review and assessment of measured values of the nonlinear refractive-index coefficient of fused silica," *Applied Optics*, vol. 37, no. 3, pp. 546–550, 1998.
- [24] M. Fox, *Optical Properties of Solids*. New York, US: Oxford University Press Inc., 2001.
- [25] R. H. Stolen, J. P. Gordon, W. J. Tomlinson, and H. A. Haus, "Raman response function of silica-core fibers," *Journal of Optical Society of America B*, vol. 6, no. 6, pp. 1159–1166, 1989.
- [26] I. P. Alcock, A. I. Ferguson, D. C. Hanna, and A. C. Tropper, "Mode-locking of a neodymium-doped monomode fibre laser," *Electronics Letters*, vol. 22, no. 5, pp. 268–269, 1986.
- [27] D. C. Hanna, A. Kazer, M. W. Phillips, D. P. Shepherd, and P. J. Suni, "Active mode-locking of an Yb:Er fibre laser," *Electronics Letters*, vol. 25, no. 2, pp. 95–96, 1989.
- [28] J. D. Kafka, T. Baer, and D. W. Hall, "Mode-locked erbium-doped fiber laser with soliton pulse shaping," *Optics Letters*, vol. 14, no. 22, pp. 1269–1271, 1989.
- [29] I. N. Duling, III, "Subpicosecond all-fibre erbium laser," *Electronics Letters*, vol. 27, no. 6, pp. 544–545, 1991.
- [30] N. Kishi, J. N. Carter, R. Mottahedeh, P. R. Morkel, R. G. Smart, A. J. Seeds, J. S. Roberts, C. C. Button, D. N. Payne, A. C. Tropper, and D. C. Hanna, "Actively mode-locked and passively Q-switched operation of thulium-doped fibre laser using multiquantum well asymmetric Fabry-Perot modulator," *Electronics Letters*, vol. 28, no. 2, pp. 175–177, 1992.

- [31] D. J. Richardson, A. B. Grudinin, and D. N. Payne, "Passive, all-fibre source of 30 fs pulses," *Electronics Letters*, vol. 28, no. 8, pp. 778–779, 1992.
- [32] M. E. Fermann, M. J. Andrejco, Y. Silberberg, and A. M. Weiner, "Generation of pulses shorter than 200 fs from a passively mode-locked Er fiber laser," *Optics Letters*, vol. 18, no. 1, pp. 48–50, 1993.
- [33] M. H. Ober, M. Hofer, and M. E. Fermann, "42-fs pulse generation from a mode-locked fiber laser started with a moving mirror," *Optics Letters*, vol. 18, no. 5, pp. 367–369, 1993.
- [34] T. Sugawa, E. Yoshida, Y. Miyajima, and M. Nakazawa, "1.6 ps pulse generation from a 1.3 μm Pr^{3+} -doped fluoride fibre laser," *Electronics Letters*, vol. 29, no. 10, pp. 902–903, 1993.
- [35] K. Tamura, E. P. Ippen, H. A. Haus, and L. E. Nelson, "77-fs pulse generation from a stretched-pulse mode-locked all-fiber ring laser," *Optics Letters*, vol. 18, no. 13, pp. 1080–1082, 1993.
- [36] K. Tamura, C. R. Doerr, L. E. Nelson, H. A. Haus, and E. P. Ippen, "Technique for obtaining high-energy ultrashort pulses from an additive-pulse mode-locked erbium-doped fiber ring laser," *Optics Letters*, vol. 19, no. 1, pp. 46–48, 1994.
- [37] H. A. Haus, K. Tamura, L. E. Nelson, and E. P. Ippen, "Stretched-pulse additive pulse mode-locking in fiber ring lasers: theory and experiment," *IEEE Journal of Quantum Electronics*, vol. 31, no. 3, pp. 591–598, 1995.
- [38] L. E. Nelson, E. P. Ippen, and H. A. Haus, "Broadly tunable sub-500 fs pulses from an additive-pulse mode-locked thulium-doped fiber ring laser," *Applied Physics Letters*, vol. 67, no. 1, pp. 19–21, 1995.
- [39] C. Hnninger, F. Morier-Genoud, M. Moser, U. Keller, L. R. Brovelli, and C. Harder, "Efficient and tunable diode-pumped femtosecond Yb:glass lasers," *Optics Letters*, vol. 23, no. 2, pp. 126–128, 1998.

- [40] F. Ö. Ilday, J. Buckley, L. Kuznetsova, and F. W. Wise, “Generation of 36-femtosecond pulses from a ytterbium fiber laser,” *Optics Express*, vol. 11, no. 26, pp. 3550–3554, 2003.
- [41] F. Ö. Ilday, J. R. Buckley, W. G. Clark, and F. W. Wise, “Self-similar evolution of parabolic pulses in a laser,” *Physical Review Letters*, vol. 92, no. 21, pp. 3902–3905, 2004.
- [42] A. Chong, J. Buckley, W. Renninger, and F. Wise, “All-normal-dispersion femtosecond fiber laser,” *Optics Express*, vol. 14, no. 21, pp. 10095–10100, 2006.
- [43] M. Baumgartl, C. Lecaplain, A. Hideur, J. Limpert, and A. Tnnermann, “66 W average power from a microjoule-class sub-100 fs fiber oscillator,” *Optics Letters*, vol. 37, no. 10, pp. 1640–1642, 2012.
- [44] E. M. Dianov, A. A. Krylov, V. V. Dvoyrin, V. M. Mashinsky, P. G. Kryukov, O. G. Okhotnikov, and M. Guina, “Mode-locked bi-doped fiber laser,” *Journal of Optical Society of America B*, vol. 24, no. 8, pp. 1807–1808, 2007.
- [45] B. Oktem, C. Igdr, and F. Ö. Ilday, “Soliton-similariton fibre laser,” *Nature Photonics*, vol. 4, no. 5, pp. 307–311, 2010.
- [46] A. Chamorovskiy, A. V. Marakulin, S. Ranta, M. Tavast, J. Rautiainen, T. Leinonen, A. S. Kurkov, and O. G. Okhotnikov, “Femtosecond mode-locked holmium fiber laser pumped by semiconductor disk laser,” *Optics Letters*, vol. 37, no. 9, pp. 1448–1450, 2012.
- [47] S. D. Jackson, “Continuous wave 2.9 μm dysprosium-doped fluoride fiber laser,” *Applied Physics Letters*, vol. 83, no. 7, pp. 1316–1318, 2003.
- [48] Y. H. Tsang, A. E. El-Taher, T. A. King, and S. D. Jackson, “Efficient 2.96 μm dysprosium-doped fluoride fibre laser pumped with a Nd:YAG laser operating at 1.3 μm ,” *Optics Express*, vol. 14, no. 2, pp. 678–685, 2006.
- [49] A. Chong, H. Liu, B. Nie, B. G. Bale, S. Wabnitz, W. H. Renninger, M. Dantus, and F. W. Wise, “Pulse generation without gain-bandwidth

- limitation in a laser with self-similar evolution,” *Optics Express*, vol. 20, no. 13, pp. 14213–14220, 2012.
- [50] A. Sell, G. Krauss, R. Scheu, R. Huber, and A. Leitenstorfer, “8-fs pulses from a compact Er: fiber system: quantitative modeling and experimental implementation,” *Optics Express*, vol. 17, no. 2, pp. 1070–1077, 2009.
- [51] G. Krauss, S. Lohss, T. Hanke, A. Sell, S. Eggert, R. Huber, and A. Leitenstorfer, “Synthesis of a single cycle of light with compact erbium-doped fibre technology,” *Nature Photonics*, vol. 4, no. 1, pp. 33–36, 2010.
- [52] K. Kieu, R. J. Jones, and N. Peyghambarian, “Generation of few-cycle pulses from an amplified carbon nanotube mode-locked fiber laser system,” *IEEE Photonics Technology Letters*, vol. 22, no. 20, pp. 1521–1523, 2010.
- [53] S. Thomas, R. Holzwarth, and P. Hommelhoff, “Generating few-cycle pulses for nanoscale photoemission easily with an erbium-doped fiber laser,” *Optics Express*, vol. 20, no. 13, pp. 13663–13668, 2012.
- [54] S. Kobtsev, S. Kukarin, and Y. Fedotov, “Ultra-low repetition rate mode-locked fiber laser with high-energy pulses,” *Optics Express*, vol. 16, no. 26, pp. 21936–21941, 2008.
- [55] S. M. Kobtsev, S. V. Kukarin, S. V. Smirnov, and Y. S. Fedotov, “High-energy mode-locked all-fiber laser with ultralong resonator,” *Laser Physics*, vol. 20, no. 2, pp. 351–356, 2010.
- [56] T. Eidam, J. Rothhardt, F. Stutzki, F. Jansen, S. Hdrich, H. Carstens, C. Jauregui, J. Limpert, and A. Tnnermann, “Fiber chirped-pulse amplification system emitting 3.8 GW peak power,” *Optics Express*, vol. 19, no. 1, pp. 255–260, 2011.
- [57] B. R. Washburn, S. A. Diddams, N. R. Newbury, J. W. Nicholson, M. F. Yan, and C. G. Jrgensen, “Phase-locked, erbium-fiber-laser-based frequency comb in the near infrared,” *Optics Letters*, vol. 29, no. 3, pp. 250–252, 2004.
- [58] R. R. Gattass and E. Mazur, “Femtosecond laser micromachining in transparent materials,” *Nature Photonics*, vol. 2, no. 4, pp. 219–225, 2008.

- [59] A. Galvanauskas, M. A. Arbore, M. M. Fejer, M. E. Fermann, and D. Harter, “Fiber-laser-based femtosecond parametric generator in bulk periodically poled LiNbO₃,” *Optics Letters*, vol. 22, no. 2, pp. 105–107, 1997.
- [60] G. Matthus, B. Orta, J. Limpert, S. Nolte, R. Hohmuth, M. Voitsch, W. Richter, B. Pradarutti, and A. Tnnermann, “Intracavity terahertz generation inside a high-energy ultrafast soliton fiber laser,” *Applied Physics Letters*, vol. 93, no. 26, p. 261105, 2008.
- [61] E. R. Thoen, *Development of Ultrashort Pulse Fiber Lasers for Optical Communication Utilizing Semiconductor Devices*. PhD thesis, Department of Electrical Engineering and Computer Science, Massachusetts Institute of Technology, 2000.
- [62] A. H. Zewail, “Femtochemistry: Atomic-scale dynamics of the chemical bond,” *Journal of Physical Chemistry A*, vol. 104, no. 24, pp. 5660–5694, 2000.
- [63] J. Kim and F. X. Krtner, “Microwave signal extraction from femtosecond mode-locked lasers with attosecond relative timing drift,” *Optics Letters*, vol. 35, no. 12, pp. 2022–2024, 2010.
- [64] D. U. Kim, H. Song, W. Song, H.-S. Kwon, M. Sung, and D. Y. Kim, “Two-photon microscopy using an Yb³⁺-doped fiber laser with variable pulse widths,” *Optics Express*, vol. 20, no. 11, pp. 12341–12349, 2012.
- [65] Y. Wang, K. Maslov, Y. Zhang, S. Hu, L. Yang, Y. Xia, J. Liu, and L. V. Wang, “Fiber-laser-based photoacoustic microscopy and melanoma cell detection,” *Journal of Biomedical Optics*, vol. 16, no. 1, p. 011014, 2011.
- [66] T. Ditmire, J. Zweiback, V. P. Yanovsky, T. E. Cowan, G. Hays, and K. B. Wharton, “Nuclear fusion from explosions of femtosecond laser-heated deuterium clusters,” *Nature*, vol. 398, no. 6727, pp. 489–492, 1999.
- [67] J. Shah, *Ultrafast Spectroscopy of Semiconductors and Semiconductor Nanostructures*. Germany: Springer, 1999.

- [68] H. Lim, Y. Jiang, Y. Wang, Y.-C. Huang, Z. Chen, and F. W. Wise, “Ultrahigh-resolution optical coherence tomography with a fiber laser source at 1 μm ,” *Optics Letters*, vol. 30, no. 10, pp. 1171–1173, 2005.
- [69] D. V. Palanker, M. S. Blumenkranz, D. Andersen, M. Wiltberger, G. Marcellino, P. Gooding, D. Angeley, G. Schuele, B. Woodley, M. Simoneau, N. J. Friedman, B. Seibel, J. Batlle, R. Feliz, J. Talamo, and W. Culbertson, “Femtosecond laser-assisted cataract surgery with integrated optical coherence tomography,” *Science Translational Medicine*, vol. 2, no. 58, pp. 1–9, 2010.
- [70] S. Juodkazis, A. V. Rode, E. G. Gamaly, S. Matsuo, and H. Misawa, “Recording and reading of three-dimensional optical memory in glasses,” *Applied Physics B*, vol. 77, no. 2–3, pp. 361–368, 2003.
- [71] A. Weiner, *Ultrafast Optics*. United States: John Wiley & Sons, 2009.
- [72] J. L. Hall, “Optical frequency measurement: 40 years of technology revolutions,” *IEEE Journal on Selected Topics in Quantum Electronics*, vol. 6, no. 6, pp. 1136–1144, 2000.
- [73] T. W. Hensch, “Nobel Lecture: Passion for precision,” *Reviews of Modern Physics*, vol. 78, no. 4, pp. 1297–1309, 2006.
- [74] J. N. Eckstein, *High resolution spectroscopy using multiple coherent interactions*. PhD thesis, Department of Physics, Stanford University, 1978.
- [75] J. K. Ranka, R. S. Windeler, and A. J. Stentz, “Visible continuum generation in air-silica microstructure optical fibers with anomalous dispersion at 800 nm,” *Optics Letters*, vol. 25, no. 1, pp. 25–27, 2000.
- [76] S. A. Diddams, D. J. Jones, J. Ye, S. T. Cundiff, J. L. Hall, J. K. Ranka, R. S. Windeler, R. Holzwarth, T. Udem, and T. W. Hensch, “Direct link between microwave and optical frequencies with a 300 THz femtosecond laser comb,” *Physical Review Letters*, vol. 84, no. 22, pp. 5102–5105, 2000.

- [77] F. Keilmann and S. Amarie, “Mid-infrared frequency comb spanning an octave based on an Er fiber laser and difference-frequency generation,” *Journal of Infrared, Millimeter, and Terahertz Waves*, vol. 33, no. 5, pp. 479–484, 2012.
- [78] A. Schliesser, N. Picqu, and T. W. Hensch, “Mid-infrared frequency combs,” *Nature Photonics*, vol. 6, no. 7, pp. 440–449, 2012.
- [79] R. J. Jones, K. D. Moll, M. J. Thorpe, and J. Ye, “Phase-coherent frequency combs in the vacuum ultraviolet via high-harmonic generation inside a femtosecond enhancement cavity,” *Physical Review Letters*, vol. 94, no. 19, p. 193201, 2005.
- [80] C. Gohle, T. Udem, M. Herrmann, J. Rauschenberger, R. Holzwarth, H. A. Schuessler, F. Krausz, and T. W. Hensch, “A frequency comb in the extreme ultraviolet,” *Nature*, vol. 436, no. 7048, pp. 234–237, 2005.
- [81] A. Cingz, D. C. Yost, T. K. Allison, A. Ruehl, M. E. Fermann, I. Hartl, and J. Ye, “Direct frequency comb spectroscopy in the extreme ultraviolet,” *Nature*, vol. 482, no. 7383, pp. 68–71, 2012.
- [82] M. Hentschel, R. Kienberger, C. Spielmann, G. A. Reider, N. Milosevic, T. Brabec, P. Corkum, U. Heinzmann, M. Drescher, and F. Krausz, “Attosecond metrology,” *Nature*, vol. 414, no. 6863, pp. 509–513, 2001.
- [83] A. A. Madej, P. Dub, Z. Zhou, J. E. Bernard, and M. Gertsvolf, “ $^{88}\text{Sr}^+$ 445-THz single-ion reference at the 10^{-17} level via control and cancellation of systematic uncertainties and its measurement against the SI second,” *Physical Review Letters*, vol. 109, no. 20, p. 203002, 2012.
- [84] T. L. Nicholson, M. J. Martin, J. R. Williams, B. J. Bloom, M. Bishof, M. D. Swallows, S. L. Campbell, and J. Ye, “Comparison of two independent Sr optical clocks with 1×10^{-17} stability at 10^3 s,” *Physical Review Letters*, vol. 109, no. 23, p. 230801, 2012.
- [85] T. Steinmetz, T. Wilken, C. Araujo-Hauck, R. Holzwarth, T. W. Hensch, L. Pasquini, A. Manescau, S. D’Odorico, M. T. Murphy, T. Kentischer,

- W. Schmidt, and T. Udem, “Laser frequency combs for astronomical observations,” *Science*, vol. 321, no. 5894, pp. 1335–1337, 2008.
- [86] S. A. Diddams, L. Hollberg, and V. Mbele, “Molecular fingerprinting with the resolved modes of a femtosecond laser frequency comb,” *Nature*, vol. 445, no. 7128, pp. 627–630, 2007.
- [87] K. Predehl, G. Grosche, S. M. F. Raupach, S. Droste, O. Terra, J. Alnis, T. Legero, T. W. Hensch, T. Udem, R. Holzwarth, and H. Schnatz, “A 920-kilometer optical fiber link for frequency metrology at the 19th decimal place,” *Science*, vol. 336, no. 6080, pp. 441–444, 2012.
- [88] I. Coddington, W. C. Swann, L. Nenadovic, and N. R. Newbury, “Rapid and precise absolute distance measurements at long range,” *Nature Photonics*, vol. 3, no. 6, pp. 351–356, 2009.
- [89] M. Grishin, ed., *Advances in Solid-State Lasers: Development and Applications*. Croatia: InTech, 2010.
- [90] J. S. Oh and S.-W. Kim, “Femtosecond laser pulses for surface-profile metrology,” *Optics Letters*, vol. 30, no. 19, pp. 2650–2652, 2005.
- [91] S.-W. Kimt, “Combs rule,” *Nature Photonics*, vol. 3, no. 6, pp. 313–314, 2009.
- [92] T. Rosenband, D. B. Hume, P. O. Schmidt, C. W. Chou, A. Brusch, L. Lorini, W. H. Oskay, R. E. Drullinger, T. M. Fortier, J. E. Stalnaker, S. A. Diddams, W. C. Swann, N. R. Newbury, W. M. Itano, D. J. Wineland, and J. C. Bergquist, “Frequency ratio of Al^+ and Hg^+ single-ion optical clocks; Metrology at the 17th decimal place,” *Science*, vol. 319, no. 5871, pp. 1808–1812, 2008.
- [93] K. J. Blow and D. Wood, “Theoretical description of transient stimulated Raman scattering in optical fibers,” *IEEE Journal of Quantum Electronics*, vol. 25, no. 12, pp. 2665–2673, 1989.
- [94] Ultrafast Optics and Lasers Group, “Simulation Software — UFOLAB.” http://ultrafast.bilkent.edu.tr/UFOLAB/Public_Tools.html, 2006.

- [95] A. K. Atieh, P. Myslinski, J. Chrostowski, and P. Galko, “Measuring the Raman time constant (T_R) for soliton pulses in standard single-mode fiber,” *IEEE Journal of Lightwave Technology*, vol. 17, no. 2, pp. 216–221, 1999.
- [96] P. D. Drummond and J. F. Corney, “Quantum noise in optical fibers. I. Stochastic equations,” *Journal of Optical Society of America B*, vol. 18, no. 2, pp. 139–152, 2001.
- [97] N. Karasawa, S. Nakamura, N. Nakagawa, M. Shibata, R. Morita, H. Shigekawa, and M. Yamashita, “Comparison between theory and experiment of nonlinear propagation for a-few-cycle and ultrabroadband optical pulses in a fused-silica fiber,” *IEEE Journal of Quantum Electronics*, vol. 37, no. 3, pp. 398–404, 2001.
- [98] D. Mogilevtsev, T. A. Birks, and P. S. J. Russell, “Group-velocity dispersion in photonic crystal fibers,” *Optics Letters*, vol. 23, no. 21, pp. 1662–1664, 1998.
- [99] N. G. R. Broderick, T. M. Monroe, P. J. Bennett, and D. J. Richardson, “Nonlinearity in holey optical fibers: measurement and future opportunities,” *Optics Letters*, vol. 24, no. 20, pp. 1395–1397, 1999.
- [100] B. R. Washburn, S. Ralph, P. A. Lacourt, J. M. Dudley, W. T. Rhodes, R. S. Windeler, and S. Coen, “Tunable near-infrared femtosecond soliton generation in photonic crystal fibers,” *Electronics Letters*, vol. 37, no. 25, pp. 1510–1512, 2001.
- [101] P. K. A. Wai, C. R. Menyuk, Y. C. Lee, and H. H. Chen, “Nonlinear pulse propagation in the neighborhood of the zero-dispersion wavelength of monomode optical fibers,” *Optics Letters*, vol. 11, no. 7, pp. 464–466, 1986.
- [102] N. Akhmediev and M. Karlsson, “Cherenkov radiation emitted by solitons in optical fibers,” *Physical Review A*, vol. 51, no. 3, pp. 2602–2607, 1995.
- [103] K. L. Corwin, N. R. Newbury, J. M. Dudley, S. Coen, S. A. Diddams, K. Weber, and R. S. Windeler, “Fundamental noise limitations to supercontinuum generation in microstructure fiber,” *Physical Review Letters*, vol. 90, no. 11, p. 113904, 2003.

- [104] B. R. Washburn and N. R. Newbury, “Phase, timing, and amplitude noise on supercontinua generated in microstructure fiber,” *Optics Express*, vol. 12, no. 10, pp. 2166–2175, 2004.
- [105] M. Bellini and T. W. Hensch, “Phase-locked white-light continuum pulses: toward a universal optical frequency-comb synthesizer,” *Optics Letters*, vol. 25, no. 14, pp. 1049–1051, 2000.
- [106] J. M. Dudley and S. Coen, “Coherence properties of supercontinuum spectra generated in photonic crystal and tapered optical fibers,” *Optics Letters*, vol. 27, no. 13, pp. 1180–1182, 2002.
- [107] L. Nugent-Glandorf, T. A. Johnson, Y. Kobayashi, and S. A. Diddams, “Impact of dispersion on amplitude and frequency noise in a Yb-fiber laser comb,” *Optics Letters*, vol. 36, no. 9, pp. 1578–1580, 2011.
- [108] W. H. Knox, “*In situ* measurement of complete intracavity dispersion in an operating Ti:sapphire femtosecond laser,” *Optics Letters*, vol. 17, no. 7, pp. 514–516, 1992.
- [109] J. W. Nicholson, J. Jasapara, W. Rudolph, F. G. Omenetto, and A. J. Taylor, “Full-field characterization of femtosecond pulses by spectrum and cross-correlation measurements,” *Optics Letters*, vol. 24, no. 23, pp. 1774–1776, 1999.
- [110] J. Kim, J. Chen, J. Cox, and F. X. Krtner, “Attosecond-resolution timing jitter characterization of free-running mode-locked lasers,” *Optics Letters*, vol. 32, no. 24, pp. 3519–3521, 2007.
- [111] Y. Song, C. Kim, K. Jung, H. Kim, and J. Kim, “Timing jitter optimization of mode-locked Yb-fiber lasers toward the attosecond regime,” *Optics Express*, vol. 19, no. 15, pp. 14518–14525, 2011.
- [112] W. J. Riley, *Handbook of Frequency Stability Analysis*. Washington, DC, USA: U.S. Government Printing Office, 2008.

Appendix A

Simulation of Pulse Propagation in Fiber Using RK4IP Algorithm

This MATLAB function calculates the output spectrum and shape of a pulse after passing through some fiber by solving GNLSE using fourth-order Runge-Kutta method in the interaction picture.

```
1 function []=RK4IP ()
2
3 tic
4
5 global w timesteps fr hr dz tres gamma h passrat
6
7 c=299792458;           %Speed of light (m/s)
8 twidth=10e-12;       %Total time window width (s)
9 tres=1e-15;          %Time resolution (s)
10 nz=5000;             %Number of z-steps
11 nsaves = 200;        %Number of saved snapshots
12 pulshape=1;          %0 for sech^2, 1 for Gaussian pulse ...
    shape
13
14 fr=0.18;
15
16 fiberlength=0.15;    %Fiber length (m)
```

```

17 aeff=7.55e-12;           %Effective mode area of the fiber (m...
    ^2)
18 n2=2.74e-20;           %Kerr coefficient (m^2/W)
19 betas=[-8.9655e-27,80.3570e-42,-103.2412e-57,110.2014e-72]; %...
    Betas (s^x/m)
20
21 pulsewidth=50e-15;     %Initial pulse duration (s)
22 peakpower=25000;       %Peak power of the initial pulse (W)
23 lambda=1050e-9;        %Central wavelength (m)
24
25 timesteps=round(twidth/tres+1);
26 t=-twidth/2:tres:twidth/2;
27
28 empty=zeros(1,timesteps);
29
30 comp_pos=[56.25,100.00,231.25,362.50,463.00,497.00,611.50,691.67...
    ,793.67,835.50,930.00,1080.00,1215.00].*100; %1/m
31 peak_int=[1.00,11.40,36.67,67.67,74.00,4.50,6.80,4.60,4.20,4.50,2...
    .70,3.10,3.00]; %Unitless
32 gau_FWHM=[52.10,110.42,175.00,162.50,135.33,24.50,41.50,155.00,59...
    .50,64.30,150.00,91.00,160.00].*100; %1/m
33 lor_FWHM=[17.37,38.81,58.33,54.17,45.11,8.17,13.83,51.67,19.83,21...
    .43,50.00,30.33,53.33].*100; %1/m
34
35 hr=empty;
36
37 for a=ceil(timesteps/2):timesteps
38     for b=1:13
39         hr(a)=hr(a)+peak_int(b)*exp(-pi*c*t(a)*lor_FWHM(b))*exp...
            (-(pi*c*gau_FWHM(b))^2*(t(a)^2)/4)*sin(2*pi*c*...
            comp_pos(b)*t(a));
40     end
41 end
42
43 hr_integral=trapz(t,hr);
44
45 hr=hr./hr_integral;
46 hr=fft(hr);
47 if (pulseshape==1)
48     E=sqrt(peakpower).*exp(-0.5*(t./pulsewidth*1.665).^2);

```

```

49 else
50     E=sqrt (peakpower)*sech (t/pulsewidth);
51 end
52 w=2*pi*c/lambda;
53
54 fs=1/(timesteps*tres);
55 freq=c/lambda+fs*linspace(-timesteps/2,timesteps/2,timesteps);
56
57 lambdaarr = c./freq;
58 gamma=n2*w/(c*aeff);
59
60 omegas=2*pi*freq;
61 B=0;
62 for i = 1:length(betas) % Taylor expansion of ...
63     B = B - li*betas(i)/factorial(i+1).*(omegas-w).^ (i+1);
64 end
65
66 passrat=0;
67 dz=fiberlength/nz;
68 h = waitbar(0, '0% done...');
69
70 k=1;
71 spectarr=zeros (nsaves,timesteps);
72 Iarr=zeros (nsaves,timesteps);
73 zarr = linspace(0, fiberlength, nsaves);
74 for i=1:nz
75     E=Prop (E, w, gamma, fr, hr, dz, tres, empty, timesteps, B);
76     passrat=i/nz;
77     if (passrat*fiberlength>=zarr(k))
78         Iarr (k, :)=abs (E).^2;
79         spectarr (k, :)=abs (fftshift (fft (E))).^2;
80         zarr(k)=i*dz;
81         k=k+1;
82     end
83 end
84
85 Spect=abs (fftshift (fft (E))).^2;
86 Spect=Spect/max (Spect);
87

```

```

88 figure;
89 plot(t,abs(E).^2);
90 grid on;
91
92 title('Temporal Intensity');
93 axis tight;
94 print -r300 -dpng 'intensity.png'
95 saveas(gcf,'intensity','fig');
96
97 figure;
98 semilogy(lambdaarr,Spect);
99 title('Output Spectrum')
100 grid on;
101 axis tight;
102 xlim([600 1750].*1e-9);
103 ylim([1e-10 1]);
104 print -r300 -dpng 'spectrum.png'
105 saveas(gcf,'spectrum','fig');
106
107 fid=fopen('RK4IP_inten.txt','w');
108 for i=1:timesteps
109     fprintf(fid,'%d %d \r\n',t(1,i),abs(E(1,i)).^2);
110 end
111 fclose(fid);
112
113 fid=fopen('RK4IP_spect.txt','w');
114 for i=1:timesteps
115     fprintf(fid,'%d %d \r\n',lambdaarr(1,i),Spect(1,i));
116 end
117 fclose(fid);
118
119 figure;
120 LIW = 10*log10(spectarr);           % log scale spectral ...
    intensity
121 mLIW = max(max(LIW));             % max value, for ...
    scaling plot
122 LIW=LIW-mLIW;
123 WL = lambdaarr; iis = (WL>500e-9&WL<1700e-9); % wavelength ...
    grid
124 s1=subplot(1,2,1);

```



```

125 pcolor(WL(iis)*1e9,zarr,lIW(:,iis)); % plot as ...
    pseudocolor map
126 caxis([-40.0, 0]); xlim([500,1700]); shading interp;
127 xlabel('Wavelength (nm)'); ylabel('Distance (m)');
128
129 lIT = 10*log10(Iarr); % log scale temporal ...
    intensity
130 mlIT = max(max(lIT)); % max value, for ...
    scaling plot
131 lIT=lIT-mlIT;
132 s2=subplot(1,2,2);
133 pcolor(t*1e12,zarr,lIT); % plot as ...
    pseudocolor map
134 caxis([-40.0,0]); xlim([-2,4]);
135 shading interp;
136 xlabel('Delay (ps)'); %ylabel('Distance (m)');
137 hb = colorbar('location','eastoutside');
138 hand=xlabel(hb,'(dB)');
139 set(hand,'position',[2 -42 0]);
140 set(s1,'Units','normalized','position',[0.1 0.1 0.37 0.85]);
141 set(s2,'Units','normalized','position',[0.50 0.1 0.37 0.85]);
142 set(s2,'ytick',[]);
143 set(hb,'Units','normalized','position',[0.9 0.1 0.03 0.85]);
144 set(findall(gcf,'type','text'),'FontSize',15,'fontWeight','bold')
145 set(findall(gcf,'type','axes'),'FontSize',15,'fontWeight','bold')...
    ;
146 print -r300 -dpng 'evolution.png'
147 saveas(gcf,'evolution','fig');
148 close(h)
149
150 toc
151
152 end
153
154 function [Eout] = Prop(Ein,w,gamma,fr,hr,dz,tres,empty,timesteps,...
    B)
155
156 global h passrat
157
158 Ai=DSPProp(Ein,B,dz/2);

```

```

159 k1=DSPProp (NLProp (Ein,w,gamma,fr,hr,dz,tres,empty,timesteps),B,dz...
    /2);
160 k2=NLProp (Ai+k1/2,w,gamma,fr,hr,dz,tres,empty,timesteps);
161 k3=NLProp (Ai+k2/2,w,gamma,fr,hr,dz,tres,empty,timesteps);
162 k4=NLProp (DSPProp (Ai+k3,B,dz/2),w,gamma,fr,hr,dz,tres,empty,...
    timesteps);
163 Eout=DSPProp (Ai+k1/6+k2/3+k3/3,B,dz/2)+k4/6;
164
165 waitbar (passrat,h, strcat (num2str (round (passrat*100)), '% done...') ...
    );
166 end
167
168 function [Eout] = NLProp (Ein,w,gamma,fr,hr,dz,tres,empty,...
    timesteps)
169
170 I=ifftshift (ifft (hr.*fft (abs (Ein).^2))).*Ein*tres*fr+(1-fr).*Ein....
    *abs (Ein).^2;
171 Eout=-dz*gamma*(I*li+1/w*dif (I,tres,empty,timesteps));
172 end
173
174 function [Eout] = DSPProp (Ein,B,dz)
175
176 Ein=fftshift (fft (Ein));
177 Eout=ifft (ifftshift (Ein.*exp (B*dz)));
178
179 end
180
181 function [out] = dif (in,tres,empty,len)
182
183 out=empty;
184
185 out (1)=(in (4)-9*in (3)+45*in (2)-45*in (len)+9*in (len-1)-in (len-2)) ...
    / (60*tres);
186 out (2)=(in (5)-9*in (4)+45*in (3)-45*in (1)+9*in (len)-in (len-1)) / (60*...
    tres);
187 out (3)=(in (6)-9*in (5)+45*in (4)-45*in (2)+9*in (1)-in (len)) / (60*tres...
    );
188 out (4:len-3)=(in (7:len)-9*in (6:len-1)+45*in (5:len-2)-45*in (3:len...
    -4)+9*in (2:len-5)-in (1:len-6)) / (60*tres);

```

```
189 out(len-2)=(in(1)-9*in(len)+45*in(len-1)-45*in(len-3)+9*in(len-4)...
    -in(len-5))/(60*tres);
190 out(len-1)=(in(2)-9*in(1)+45*in(len)-45*in(len-2)+9*in(len-3)-in(...
    len-4))/(60*tres);
191 out(len)=(in(3)-9*in(2)+45*in(1)-45*in(len-1)+9*in(len-2)-in(len...
    -3))/(60*tres);
192
193 end
```

Appendix B

Simulation of Pulse Propagation in Fiber Using RK4IP Algorithm with Adaptive Step-Size

This MATLAB function calculates the output spectrum and shape of a pulse after passing through some fiber by solving GNLSE using fourth-order Runge-Kutta method in the interaction picture with adaptive step-size.

```
1 function []=RK4IP_adaptive()  
2  
3 tic  
4  
5 global w timesteps fr hr dz tres gamma h fiberlength totalsteps ...  
   minstep maxstep totalaccepted passed tol  
6  
7 c=299792458;           %Speed of light (m/s)  
8 twidth=10e-12;        %Total time window width (s)  
9 tres=1e-15;           %Time resolution (s)  
10 dz=0.1;               %Initial z-step size (m)  
11 tol=1e-8;             %Relative error tolerance  
12 pulshape=1;           %0 for sech^2, 1 for Gaussian pulse ...  
   shape
```

```

13
14 fr=0.18;
15
16 fiberlength=0.3;           %Fiber length (m)
17 aeff=7.55e-12;           %Effective mode area of the fiber (m...
    ^2)
18 n2=2.74e-20;             %Kerr coefficient (m^2/W)
19 betas=[-7.5946e-27,78.5925e-42,-101.3403e-57,110.2014e-72]; %...
    Betas (s^x/m)
20
21 pulsewidth=35e-15;       %Initial pulse duration (s)
22 peakpower=24000;        %Peak power of the initial pulse (W)
23 lambda=1040e-9;         %Central wavelength (m)
24
25 timesteps=round(twidth/tres+1);
26 t=-twidth/2:tres:twidth/2;
27
28 empty=zeros(1,timesteps);
29
30 comp_pos=[56.25,100.00,231.25,362.50,463.00,497.00,611.50,691.67...
    ,793.67,835.50,930.00,1080.00,1215.00].*100; %1/m
31 peak_int=[1.00,11.40,36.67,67.67,74.00,4.50,6.80,4.60,4.20,4.50,2...
    .70,3.10,3.00]; %Unitless
32 gau_FWHM=[52.10,110.42,175.00,162.50,135.33,24.50,41.50,155.00,59...
    .50,64.30,150.00,91.00,160.00].*100; %1/m
33 lor_FWHM=[17.37,38.81,58.33,54.17,45.11,8.17,13.83,51.67,19.83,21...
    .43,50.00,30.33,53.33].*100; %1/m
34
35 hr=empty;
36
37 for a=ceil(timesteps/2):timesteps
38     for b=1:13
39         hr(a)=hr(a)+peak_int(b)*exp(-pi*c*t(a)*lor_FWHM(b))*exp...
            (-(pi*c*gau_FWHM(b))^2)*(t(a)^2)/4)*sin(2*pi*c*...
            comp_pos(b)*t(a));
40     end
41 end
42
43 hr_integral=trapz(t,hr);
44

```

```

45 hr=hr./hr_integral;
46 hr=fft(hr);
47
48 if (pulseshape==1)
49     E=sqrt(peakpower).*exp(-0.5*(t./pulsewidth*1.665).^2);
50 else
51     E=sqrt(peakpower)*sech(t/pulsewidth);
52 end
53 w=2*pi*c/lambda;
54
55 fs=1/(timesteps*tres);
56 freq=c/lambda+fs*linspace(-timesteps/2,timesteps/2,timesteps);
57
58 lambdaarr = c./freq;
59 gamma=n2*w/(c*aeff);
60
61 omegas=2*pi*freq;
62 B=0;
63 for i = 1:length(betas) % Taylor expansion of ...
64     B = B - li*betas(i)/factorial(i+1).*(omegas-w).^(i+1);
65 end
66
67 photonin=CountPhoton(E,freq);
68 fprintf('Number of Input Photons: %e \n',photonin);
69
70 if (gamma==0)
71     dz=fiberlength;
72 end
73 passed=0;
74
75 h = waitbar(0,'0% done...');
76 totalsteps=0;
77 maxstep=0;
78 minstep=fiberlength;
79 totalaccepted=0;
80 E=Prop(E,w,gamma,fr,hr,tres,empty,timesteps,B,photonin,freq);
81
82 disp(strcat('Total number of steps: ',num2str(totalsteps)));

```

```

83 disp(strcat('Total number of accepted steps: ',num2str(...
    totalaccepted)));
84 disp(strcat('Minimum stepsize: ',num2str(minstep)));
85 disp(strcat('Maximum stepsize: ',num2str(maxstep)));
86
87 photonout=CountPhoton(E,freq);
88 fprintf('Number of Output Photons: %e \n',photonout);
89
90 Spect=abs(fftshift(fft(E))).^2;
91 Spect=Spect/max(Spect);
92
93 figure;
94 plot(t,abs(E).^2);
95 grid on;
96 title(strcat('Output Energy: ',num2str(trapz(t,abs(E).^2))));
97 axis tight;
98
99 figure;
100 plot(lambdaarr,Spect);
101 title('Output Spectrum');
102 grid on;
103 axis tight;
104 xlim([600 1750].*1e-9);
105
106 figure;
107 semilogy(lambdaarr,Spect);
108 title('Output Spectrum')
109 grid on;
110 axis tight;
111 xlim([600 1750].*1e-9);
112 ylim([1e-10 1]);
113
114 fid=fopen('RK4IP_adaptive_spect.txt','w');
115 for i=1:timesteps
116     fprintf(fid,'%d %d \r\n',lambdaarr(1,i),Spect(1,i));
117 end
118 fclose(fid);
119
120 close(h)
121

```

```

122 toc
123
124 end
125
126 function [Eout] = Prop(Ein,w,gamma,fr,hr,tres,empty,timesteps,B,...
    photonin,freq)
127
128 global h passed fiberlength totalsteps minstep maxstep ...
    totalaccepted dz tol
129
130 while (passed<fiberlength)
131
132     if (dz>(fiberlength-passed))
133         dz=(fiberlength-passed);
134     end
135     totalsteps=totalsteps+1;
136
137     Ai=DSPProp(Ein,B,dz/2);
138     k1=DSPProp(NLProp(Ein,w,gamma,fr,hr,dz,tres,empty,timesteps),B,...
        ,dz/2);
139     k2=NLProp(Ai+k1/2,w,gamma,fr,hr,dz,tres,empty,timesteps);
140     k3=NLProp(Ai+k2/2,w,gamma,fr,hr,dz,tres,empty,timesteps);
141     k4=NLProp(DSPProp(Ai+k3,B,dz/2),w,gamma,fr,hr,dz,tres,empty,...
        timesteps);
142     Eout=DSPProp(Ai+k1/6+k2/3+k3/3,B,dz/2)+k4/6;
143
144     photonout=CountPhoton(Eout,freq);
145
146     Δ=abs(photonout-photonin)/photonin;
147
148     if (Δ<2*tol)
149         Ein=Eout;
150         photonin=photonout;
151         passed=passed+dz;
152         minstep=min(minstep,dz);
153         maxstep=max(maxstep,dz);
154         totalaccepted=totalaccepted+1;
155         waitbar(passed/fiberlength,h, strcat(num2str(round(passed/...
            fiberlength*100)), '% done...'));
156         if (Δ>tol)

```



```

157         dz=dz/2^(0.2);
158     elseif ( $\Delta$ <tol)
159         dz=dz*2^(0.2);
160     end
161 else
162     dz=dz/2;
163 end
164
165 end
166
167 end
168
169 function [Eout] = NLProp(Ein,w,gamma,fr,hr,dz,tres,empty,...
    timesteps)
170
171 Eabs=abs(Ein).^2;
172
173 I=ifftshift(ifft(hr.*fft(Eabs))).*Ein*tres*fr+(1-fr).*Ein.*Eabs;
174 Eout=-dz*gamma*(I*li+1/w*dif(I,tres,empty,timesteps));
175
176 end
177
178 function [Eout] = DSProp(Ein,B,dz)
179
180 Ein=fftshift(fft(Ein));
181 Eout=ifft(ifftshift(Ein.*exp(B*dz)));
182
183 end
184
185 function [photonn] = CountPhoton(Ein,freq)
186
187 Spect=abs(fftshift(fft(Ein))).^2;
188 photonn=sum(Spect./(6.626e-34*freq));
189
190 end
191
192 function [out] = dif(in,tres,empty,len)
193
194 out=empty;
195

```

```

196 out(1)=(in(4)-9*in(3)+45*in(2)-45*in(len)+9*in(len-1)-in(len-2))...
    /(60*tres);
197 out(2)=(in(5)-9*in(4)+45*in(3)-45*in(1)+9*in(len)-in(len-1))/(60*...
    tres);
198 out(3)=(in(6)-9*in(5)+45*in(4)-45*in(2)+9*in(1)-in(len))/(60*tres...
    );
199 out(4:len-3)=(in(7:len)-9*in(6:len-1)+45*in(5:len-2)-45*in(3:len...
    -4)+9*in(2:len-5)-in(1:len-6))/(60*tres);
200 out(len-2)=(in(1)-9*in(len)+45*in(len-1)-45*in(len-3)+9*in(len-4)...
    -in(len-5))/(60*tres);
201 out(len-1)=(in(2)-9*in(1)+45*in(len)-45*in(len-2)+9*in(len-3)-in(...
    len-4))/(60*tres);
202 out(len)=(in(3)-9*in(2)+45*in(1)-45*in(len-1)+9*in(len-2)-in(len...
    -3))/(60*tres);
203
204 end

```